UNIVERSITY OF CATANIA

Department of Electrical, Electronic and Computer Engineering
Ph.D. in "Systems, Energy, Computer and Telecommunications Engineering"

METHODS FOR THE MODELING AND CONTROL OF ARTIFICIAL AND NATURAL COMPLEX NETWORKS

Candidate:
Alessandra Corso

Supervisors:
Prof. Mattia Frasca
Prof. Lucia Valentina Gambuzza

Cycle XXXVIII

Acknowledgements

The work presented in this thesis has been possible thanks to the support and collaboration of many people and institutions.

I would like to thank my supervisors, Prof. Mattia Frasca and Prof. Lucia Valentina Gambuzza, for their guidance during these years. They provided me with the opportunity to broaden my expertise in complex systems and to apply these methods in different contexts, encouraging a multidisciplinary perspective.

I am also grateful to the Professors and researchers with whom I collaborated on several publications: Prof. Pietro De Lellis from University of Naples Federico *II*, Prof. Vito Latora, from Queen Mary University of London, Dr. Federico Malizia, from Northeastern University London, Prof. Ludovico Minati, from University of Electronic Science and Technology of China, and Prof. Giovanni Russo, from University of Catania.

I acknowledge Prof. Mario Chavez and Prof. Fabrizio De Vico Fallani, and the whole NERV Lab team at the Fondation ICM, Paris Brain Institute, for hosting me during my Erasmus+ short–term stay. I would like to especially thank Dr. Alice Longhena, Dr. Camilla Mannino, and Dr. Tristan Venot for their kindness and warm welcome during that period.

My sincere thanks go to my colleagues in the Control of Complex Networks Lab, in particular Dr. Chiara Condorelli, Dr. Cinzia Tomaselli, Dr. Amar Venkatachalam, and Dr. Wenying Yuan, as well as the all the other Ph.D. students of the group, for their daily support.

Finally, I am deeply thankful to my friends and my family for their constant care and encouragement throughout this work.

Contents

Chapter 1

Introduction

1.1 Background and state of the art

The study of complex networks, whether artificial or natural, addresses a fundamental problem in the modeling and control of systems comprised of interacting units. These systems are widespread in both engineered and biological domains, ranging from power grids and neural circuits to ecosystems and social structures. Their fundamental characteristic is the emergence of global behavior from local interactions among dynamical, often nonlinear, units that evolve over heterogeneous topologies. A rigorous understanding of such systems requires the development of mathematical frameworks capable of capturing not only pairwise interactions but also higher-order structures, adaptation mechanisms, spatial embedding, and control mechanisms. Despite significant advances, several theoretical and methodological challenges remain open, particularly in reconstructing network structure from data, generating surrogate models preserving topological and spatial properties, and ensuring synchronization under limited control resources.

One key challenge in this context is the reconstruction of network connectivity from observed dynamics [98], particularly in systems where interactions are not limited to isolated pairs of units. In many complex systems, the evolution of each component cannot be fully understood without accounting for the collective effect of interactions [107] involving multiple units simultaneously, commonly referred to as higher-order interactions [57, 5, 48, 46, 76]. They capture combined effects among multiple nodes that are not recover-able through pairwise approximations, as this would entail a significant loss of structural and dynamical information. Such structures are encountered, for instance, in engineered dynamical systems, neural populations, and ecological networks, where emergent behavior results from coordinated activity across pairs or larger subsets of the network nodes.

Reconstructing these structures from time-series data is an instance of the inverse problem, namely understanding which structure generates a given, observed dynamics. Classical approaches often assume that the observed dynamics reflect an underlying graph where each node is influenced by a limited number of neighbors through pairwise couplings. However, when the actual dependencies involve more than two nodes simultaneously, pairwise models fail to capture the full structure of the system. Traditional reconstruction methods were primarily based on statistical inference tools [99], such as pairwise correlations [83], mutual information, or Granger causality [62, 109], often developed for discrete-state models or small networks. While these approaches provided useful insights, they lacked the scalability and robustness required for high-dimensional, continuous dynamical systems. More recent methods address this limitation by incorporating model equations describing the system's dynamics and formulating the reconstruction task as a constrained optimization problem, typically using sparse regression techniques [105]. These strategies have improved the accuracy of inferred interaction patterns from time-series data, yet significant challenges remain. In particular, they are sensitive to noise, subject to overfitting spurious correlations, and often fail to accurately distinguish true interactions from emergent statistical artefacts.

Another issue of the reconstruction problem arises when the network itself evolves over time, for example during critical events such as faults or cascading failures [42, 90, 111]. This is particularly evident in power grids, where the physical topology can change suddenly due to external disturbances, leading to dynamically shifting patterns of connectivity. In these cases, reconstructing the effective interaction structure requires methods that are not only accurate but also capable of tracking time-varying configurations under uncertainty. The difficulty is compounded by the fact that the data available may reflect only a limited time window or an incomplete set of measurements. In such contexts, model-based techniques that make use of known dynamical laws, enforce sparsity constraints, and operate with limited prior knowledge have shown particular promise. These methods aim to recover the minimal set of interactions that explain the observed dynamics.

In parallel with reconstruction efforts, the development of generative models for complex networks plays a complementary and essential role [17]. These models aim to produce synthetic networks that reproduce structural and spatial properties observed in real systems, providing a platform for hypothesis testing, robustness evaluation, and comparative analysis. Formulating the problem becomes non-trivial in systems that are spatially embedded, such as power grids, transportation networks, or anatomical brain structures, where the physical location of nodes imposes constraints on possible connections. In these contexts, the cost of wiring, the spatial proximity of nodes, and the geometry of the embedding space influence the construction and optimization of network topology.

Traditional generative approaches are based on probabilistic or geometric attachment rules designed to reproduce specific structural features of real networks. Classical examples include the Erdös Rény model [40], which generate networks with connections placed uniformly at random, the Watts-Strogatz model [106], which produce networks combining regular local structure with random long-range connections, and the Barabási-Albert model [11], which generates networks where a few nodes become highly connected compared to the majority. However, these models are abstract and not based on specific spatial networks, but rather aim to reproduce general structural features observed in real systems. More advanced generative models attempt to incorporate spatial constraints together with topological features, offering greater flexibility in reproducing empirical network structures. In the literature, several approaches have been proposed in this direction, including geometric graphs, where connections are based on spatial proximity; spatial generalizations of Erdös Rény graphs, which randomize connections under distance-dependent probabilities; spatial small-world models, which combine local geometric neighborhoods with limited long-range links; spatial growth models, where networks expand by progressively adding nodes and edges according to distance rules; and networks optimized according to spatial cost functions, where the configuration minimises wiring costs subject to functional requirements [12]. These models account for the embedding of nodes in space and for the fact that connection probabilities or wiring strategies depend not only on abstract statistical rules but also on geometric distances and cost-related considerations. However, defining models that simultaneously respect spatial geometry and structural heterogeneity remains an open challenge.

In addition to reconstructing or generating network structures, an equally important challenge is the design of strategies that can actively control their dynamics. Many systems require some form of coordination, for instance aligning the rhythms of oscillators, maintaining stable frequencies in power grids, or ensuring coherent activity in neural populations. Control can be attempted in several ways. Some approaches act globally, adjusting interaction strengths across the entire network at once, while others operate locally, letting each unit react only to the behavior of its direct neighbors. A further step consists in allowing the very structure of the network to change: connections can be strengthened, weakened, created, or removed depending on how well the system is performing. This idea has been explored in different contexts, from models of coupled oscillators to networks that rewire themselves in order to avoid overloads. These examples highlight that effective control often relies not only on tuning the dynamics of individual nodes but also on adapting the interaction pattern itself, so that structure and dynamics evolve together toward coordinated behavior [13, 53].

In many artificial and natural systems, the network structure is not fixed but adapts in response to the evolving dynamics of its nodes. This mutual dependence between structure and dynamics [19] is a key characteristic of adaptive or time-varying networks [50, 39]. In these systems, interactions change over time depending on local activity, internal rules, or overall goals. This phenomenon is observed in different domains: neuronal synapses that adapt to correlated activity, infrastructure networks that adjust to demand variations, and engineered systems that reconfigure connections based on performance.

Within this adaptive framework, a central problem is the design of decentralized strategies that can guide the system toward coordinated states, such as synchronization [115], using only local information and limited control resources. One effective class of approaches is based on adaptive mechanisms, where connections are created or removed according to the synchronization error observed between nodes, possibly under additional boundaries such as limited resources. These mechanisms allow the network to reorganize its links in response to the current state of the dynamics, enhancing configurations that promote coordinated behavior. This mechanism allows the network to self-organize into structures that enable synchronization, by creating or removing links in response to the observed differences between node dynamics. Compared to static control methods, edge snapping offers greater flexibility and robustness, particularly in systems with heterogeneous components or limited data availability.

Synchronization is a widely observed phenomenon in networked systems, playing a central role in coordinated behaviors such as coherent oscillations in neural circuits and frequency regulation in power grids. It arises when units with internal dynamics adjust their states through interactions with others, eventually exhibiting coherent evolution. Depending on the system, synchronization may involve complete alignment of states, phase locking, or more general forms of coordinated temporal structure. Its emergence depends on both the intrinsic dynamics of individual units and the pattern of interactions within the network, making it a paradigmatic example of collective behavior shaped by structure and dynamics [34].

When moving from adaptive control strategies to systems characterised by strongly nonlinear or chaotic dynamics, the problem of synchronization becomes even more challenging. The challenge is heightened by the fact that chaotic dynamics, heterogeneous architectures, and sensitivity to perturbations interact in ways that hinder stable collective behavior. In such systems, the synchronization manifold, defined as the set of states in which all nodes follow the same trajectory, is often unstable or highly sensitive to small perturbations. This makes the design of the coupling strategy especially important. The Master Stability Function (MSF) provides an effective analytical framework to determine whether synchronization can be achieved, based on the Laplacian spectrum of the network and the dynamics of individual nodes. It also reveals that increasing the coupling strength does not always improve synchrony; beyond a certain threshold, it may actually slow convergence or cause instability.

Simulated systems based on coupled chaotic oscillators have been used to validate these theoretical predictions, showing that excessive coupling can induce desynchronization or multi-stable behavior. These results highlight the need for control approaches that do not merely enforce synchronization by increasing connectivity, but instead account for the interplay between network topology, coupling strength, and intrinsic node dynamics. Achieving reliable synchronization in such settings requires a balance between structural design and dynamic response, supported by rigorous analytical and empirical evaluation [73].

Taken together, these challenges motivate the research developed in this thesis and aimed at advancing the theory and application of modeling and controlling complex networks. The central objectives include: reconstructing interaction structures, including higher-order and time-varying configurations, from empirical data (see Chapter 3); generating surrogate networks that preserve the spatial and topological properties of real systems (see Chapter 4); designing decentralized control mechanisms that promote synchronization through structural adaptation via limited resources (see Chapter 5); and analyzing the effects of coupling strength on synchronization times and stability, with implications for control design (see Chapter 6).

This thesis addresses these objectives through the development of dedicated methods and analytical tools, with applications to both artificial and biological networks. By integrating reconstruction, modeling, and control within a common framework, it aims to clarify key mechanisms underlying the dynamics of complex networks and to support their analysis and control. The approaches proposed are relevant to several domains, including power systems, neuroscience, and systems biology, and contribute to a broader methodological understanding of structured collective behavior.

1.2 Research contributions

This work proposes a set of methods for the modeling and control of complex networks, developed in response to specific theoretical and practical challenges identified in artificial and natural systems. The approach integrates techniques for structure reconstruction, generative modeling, and decentralized control, with particular attention to spatial constraints, higher-order dependencies, and adaptive dynamics. Each method targets distinct aspect of the problem, and all are developed within a unified framework based on structural analysis, optimization techniques, and the study of nonlinear dynamics.

The first line of investigation concerns the reconstruction of interaction structures from observed dynamics in systems where collective behavior emerges through interactions that cannot be reduced to pairwise terms. A method is introduced to infer both pairwise and higher-order dependencies by solving a sparse inverse problem constrained by the known equations of system dynamics. The method relies on a regularised optimization scheme to extract the underlying higher-order structure from time-series data, allowing true multi-node interactions to be separated from spurious effects. The method is validated on simulated dynamical systems and microbial interaction models, showing robustness to noise and scalability to high-dimensional settings [71].

A different line of work focuses on systems exposed to structural perturbations, where the set of active connections is not fixed but changes abruptly during critical events. An important case is power grids under failure cascades, where disturbances perturb the actual topology in real time. To address this scenario, a reconstruction strategy is introduced that combines knowledge of the governing dynamics with sparsity assumptions, allowing the time-varying connectivity to be inferred from limited observations. This method uses short-term data and remains applicable under missing information, providing insight into dynamically changing interactions during cascading failures. Tests on simulated high-voltage grid data demonstrate its ability to recover key structural features under realistic uncertainty [30].

To complement data-driven reconstruction, the thesis introduces a generative model capable of producing surrogate spatial networks that reflect both geometric constraints and empirical topological features. The model defines a spatial attachment rule controlled by a distance-dependent function with adjustable parameters. Its outputs are evaluated in terms of properties such as mean degree, average shortest path length, and global clustering coefficient. This enables the generation of networks that reproduce spatial constraints of observed systems, while structural features are evaluated for consistency with real networks. The framework offers a tool for hypothesis testing and structural analysis in systems where spatial positioning plays a central role, such as power grids and brain networks.

A second group of methods focuses on control, particularly on the emergence of synchronization under structural bounds. A decentralized mechanism allows each node to form or remove connections depending on local state differences, while enforcing a saturation constraint that limits the maximum number of active links. This mechanism, known as edge snapping, enables the network to self-organise into a synchronised configuration without global supervision. A multilayer implementation is presented, allowing different types of links to be managed independently, and the method is shown to stabilise synchronization in heterogeneous networks of chaotic oscillators while respecting global constraints on connectivity and cost [29].

The analysis is extended to investigate the effect of coupling intensity on the stability and convergence of synchronization. Using networks of chaotic circuits as a reference system, the study explores how variations in interaction strength influence the dynamical response of the system. The Master Stability Function is employed to characterise synchronization stability as a function of network topology and coupling gain. It is shown that excessive coupling can lead to delays or instability, even when structural conditions are favourable. These results highlight the need for coordinated tuning of both structural and dynamical parameters in control design.

1.3 Thesis structure

This section provides an overview of how the thesis is organised and how the different chapters connect to one another.

Since the present chapter, Chapter 1, is devoted to the introduction, it outlines the general motivations, objectives, and methodological perspective adopted throughout the work. It also places the study within the broader context of modeling and controlling complex networks, clarifying why both artificial and natural systems are considered.

Following this introductory chapter, Chapter 2 develops the necessary background. It reviews the essential elements of graph theory and higher-order structures, introduces the main measures used to characterise network topology, and recalls basic tools of dynamical systems theory that will later be used to analyze synchronization and control. Taken together, these first two chapters prepare the ground for the core contributions by establishing notation, clarifying assumptions, and providing the theoretical and conceptual framework within which the subsequent investigations are carried out.

The core of the thesis is then developed in four research chapters, each of which is divided into subsections that address complementary aspects of the general problem of modeling and controlling artificial and natural complex networks. The structure is designed to guide the reader step by step, from methods that reconstruct networks from data, to models that generate them according to given rules, to adaptive control strategies, and finally to theoretical tools for stability analysis.

Chapter 3 is dedicated to the reconstruction of network structure from data. It begins with a general discussion on the role of identifying hidden connectivity patterns in complex systems, which is essential both for understanding collective behavior and for designing effective interventions. The central idea is that measurements of the temporal evolution of the system can be transformed into tractable mathematical problems, where the unknowns correspond to the entries of matrices or tensors that encode pairwise and higher-order interactions. This makes it possible to reconstruct not only simple graphs, but also more complex structures such as hypergraphs and simplicial complexes. The first applications concern artificial networks. One focus is on ensembles of nonlinear oscillators, such as Rössler systems, where the framework is tested to recover both pairwise couplings and group interactions. This shows how higher-order effects can be identified by incorporating the form of the interaction functions. A second application is to models of power grids, where the dynamics of nodes are described by swing equations. In this case, the method is used to infer which transmission lines are active or have failed, based only on measurements of node variables such as voltage phases and angular frequencies. These two examples show how reconstruction can be applied to systems of very different nature, yet within the same mathematical formulation. The approach is then extended to natural networks, with a particular focus on microbial ecosystems. In this setting, reconstruction is used to disentangle the role of higher-order interactions in shaping community dynamics, moving beyond the simpler description in terms of pairwise competition or cooperation. The chapter concludes by discussing the challenges that arise when scaling the method to larger networks or when working with data affected by noise or incompleteness, and outlines the need for solutions tailored to the system under study.

Chapter 4 turns to the development of generative models for spatially embedded networks. After an introductory discussion on the distinction between data-driven inference and rule-based generation, the chapter presents a model that combines empirical degree distributions with spatial constraints to reproduce key features of real networks. The first subsections outline the basic procedure: nodes are placed in space, degrees are drawn from observed distributions, and connections are established with probabilities that decrease with distance. Subsequent sections explore the effect of introducing spatial constraints of increasing strictness on the model's ability to replicate important network properties. Case studies are then introduced. For power grids, the analysis shows how a two-dimensional embedding and distance-based rules can reproduce the main features observed in the real networks. For brain networks, which are three-dimensional and highly modular, much stronger distance penalties are needed to reproduce the observed organization. The chapter closes by comparing this transparent, rule-based approach with recent data-intensive generative models, highlighting the advantages of interpretability, parameter control, and applicability when only limited data are available.

Chapter 5 introduces an adaptive multilayer control protocol that extends the classical edge snapping algorithm. The chapter begins with a review of synchronization control methods and then presents the adaptive mechanism, which allows links in a control layer to be activated or removed depending on the observed degree of synchrony and on explicit constraints limiting the number of links per node. The first subsections test the method on networks of nonlinear oscillators, showing how synchrony can be achieved with fewer resources than in classical edge snapping. A second set of subsections extends the analysis to a model of the Italian high-voltage power grid, where failures can spread across the network when transmission lines are overloaded. Here, the adaptive control layer is shown to restore synchrony and prevent cascading failures even under limited resources. The chapter concludes with a discussion of possible extensions, including heterogeneous resource allocation, restrictions on adaptive links, and control applied only to subsets of nodes.

Chapter 6 provides a theoretical analysis of synchronization based on the Master Stability Function (MSF). The MSF is a general mathematical framework that decouples the local dynamics of each unit from the network topology, reducing the stability problem to the study of eigenvalues of the coupling matrix. The chapter then illustrates its application to networks of chaotic electronic circuits, showing how the structure of the network influences the stability of the synchronous state, and how different topologies can be compared in terms of their ability to support synchronization.

The final Chapter 7 brings together the insights gained across the different approaches. It connects the challenges of reconstruction, the role of spatial constraints in generative modeling, the benefits of adaptive control strategies, and the predictive power of the MSF framework. By linking these perspectives, the thesis highlights the recurring mechanisms that shape the behavior of complex networks and suggests possible directions for future research at the interface between modeling and control.

Chapter 2

Mathematical models of complex networks

The characterization and modeling of artificial and natural complex networks require a formal description of both their structure and the processes that unfold upon them. Building on the concepts introduced earlier, the focus now shifts to the mathematical framework that enables these aspects to be addressed in a unified manner, combining structural descriptors with the representation of dynamical behaviors.

2.1 Notation

In this section we introduce the notation used in the thesis, adopting a consistent set of symbols to describe the mathematical objects, variables, and parameters that will be employed throughout the work. These conventions provide a common framework for the formulations and analyzes developed in the following chapters.

2.1.1 Sets, indices, and variables

- $\mathbb{N}$, $\mathbb{R}$: sets of natural and real numbers, respectively.
- i, j, k: integer indices labelling nodes or units in a network, with $i, j, k \in \{1, \ldots, N\}$ unless otherwise stated.
- $t \in \mathbb{Z}$: discrete time step in discrete-time formulations.

- Bold lowercase letters (e.g., $\mathbf{x}_i$) denote column vectors; uppercase letters (e.g., X) denote matrices, unless otherwise specified.
- Scalars and parameters are written in italic (e.g., x_i, a, b, c), while upright roman is reserved for mathematical constants (e.g., e, i, π), units, and operators (e.g. sin, cos, log).

2.1.2 Matrices and operators

- $A = [a_{ij}]$: adjacency matrix of a network, with $a_{ij} \neq 0$ indicating a link from node j to node i.
- k_i: degree of node i.
- $L = [L_{ij}]$: Laplacian matrix.
- $F(\cdot)$: intrinsic dynamics of an uncoupled node.
- $H(\cdot, \cdot)$: coupling function between two connected nodes.
- A^{T}: transpose of a matrix A.
- $\|\cdot\|$: Euclidean norm of a vector.

2.1.3 Graph- and dynamics-related conventions

- $\mathbf{x}_i(t)$: state vector of node i at time t, with dimension m depending on the specific model.
- $\theta_i(t)$: phase or voltage phase angle of node i at time t.
- $\omega_i(t)$: angular velocity of node i at time t; in power systems, $\omega_i(t) = \dot{\theta}_i(t)$ relative to a synchronous reference frame.
- σ: coupling strength between connected nodes.
- $a^{(1)}_{ij}$, $a^{(2)}_{ijk}$: pairwise and three-body interaction coefficients, respectively, in higher-order dynamical models.

2.2 Graphs

Graphs provide the basic mathematical framework for representing the interaction structure of a networked system. In this context, nodes represent the individual units of the system, while edges encode the existence and nature of interactions between them. The graph formalism accommodates a variety of configurations, including undirected or directed connections, uniform or weighted link strengths, and static or time-varying structures.

Several matrix representations, such as the adjacency matrix, degree matrix, and Laplacian matrix, capture different structural aspects and play a central role in the analysis of network dynamics. These representations will be extensively used in the following chapters to formulate the reconstruction, modeling, and control problems addressed in this thesis.

Definition 2.2.1 (Graph) *A graph is a mathematical object described by the pair* $\mathcal{G} = (\mathcal{V}, \mathcal{E})$*, where* $\mathcal{V}(\mathcal{G}) = \{1, 2, \ldots, N\}$ *is the set of nodes (or vertices), and* $\mathcal{E}(\mathcal{G}) \subseteq \mathcal{V} \times \mathcal{V}$ *is the set of links (or edges).*

Definition 2.2.2 (Subgraph) *A subgraph of* $\mathcal{G} = (\mathcal{V}, \mathcal{E})$ *is a graph* $\mathcal{G}' = (\mathcal{V}', \mathcal{E}')$ *such that* $\mathcal{V}' \subseteq \mathcal{V}$ *and* $\mathcal{E}' \subseteq \mathcal{E} \cap (\mathcal{V}' \times \mathcal{V}')$*.*

Definition 2.2.3 (Directed and undirected graphs) *A directed graph is a graph in which each edge has an orientation, represented as an ordered pair* (i, j) *indicating a link from node* i *to node* j*. An undirected graph is a graph in which each edge has no orientation, meaning that* $(i, j) \in \mathcal{E}$ *also implies* $(j, i) \in \mathcal{E}$*.*

Definition 2.2.4 (Weighted and unweighted graphs)
A weighted graph is a graph $\mathcal{G} = (\mathcal{V}, \mathcal{E}, w)$ *where each edge* $(i, j) \in \mathcal{E}$ *is assigned a weight* $w_{ij} \in \mathbb{R}$*. The weight can represent quantities such as cost, distance, or capacity, and may take positive or negative values depending on the application. An unweighted graph is a graph in which each edge* $(i, j) \in \mathcal{E}$ *has the same weight, typically* $w_{ij} = 1$*.*

Definition 2.2.5 (Path) *A path in a graph is a sequence of nodes* $(v_1, v_2, \ldots, v_p)$ *such that* $(v_i, v_{i+1}) \in \mathcal{E}$ *for all* $1 \leq i < p$*. The length of the path is* $p - 1$*.*

Definition 2.2.6 (Connected components) *In a graph, two nodes* v_{c_1} *and* v_{c_2} *are said to be connected if there exists a path from* v_{c_1} *to* v_{c_2}*. A connected component is a maximal set of nodes such that every pair of nodes is connected.*

Definition 2.2.7 (Adjacency matrix) *Let* $\mathcal{G} = (\mathcal{V}, \mathcal{E})$ *be a graph with* N *nodes, the adjacency matrix associated to* $\mathcal{G}$ *is a square matrix* $A = [a_{ij}]$ *of* *dimension $N \times N$, where*

$$a_{ij} = \begin{cases} w_{ij} \in \mathbb{R}, & \textit{if there exists a link from node } i \textit{ to node } j, \\ 0, & \textit{otherwise.} \end{cases}$$

In the unweighted case, $w_{ij} = 1$ for all $(i, j) \in \mathcal{E}$, so that $a_{ij} \in \{0, 1\}$; in the weighted case, a_{ij} can take real values.

If the graph is undirected, then $a_{ij} = a_{ji}$ for all i, j, and the matrix A is symmetric. If the graph is directed, a_{ij} and a_{ji} are independent, and A can be asymmetric.

Definition 2.2.8 (Degree matrix) *The degree of a node i in an undirected graph is defined as*

$$k_i = \sum_{j=1}^{N} a_{ij}.$$

For directed graphs, the in-degree and out-degree of node i are defined as

$$k_i^{in} = \sum_{j=1}^{N} A_{ji}, \qquad k_i^{out} = \sum_{j=1}^{N} a_{ij}.$$

The degree matrix K of dimension $N \times N$ is the diagonal matrix whose entries are the node degrees:

$$K_{ii} = k_i, \qquad K_{ij} = 0 \textit{ for } i \neq j.$$

Definition 2.2.9 (Laplacian matrix) *Given a graph $\mathcal{G}$ with adjacency matrix A and degree matrix K, the Laplacian matrix is defined as*

$$L = K - A.$$

For undirected graphs, K is the diagonal matrix of node degrees, L is symmetric and positive semi-definite, and all its eigenvalues are non-negative. An eigenvalue λ of L is a scalar for which there exists a nonzero vector v (the corresponding eigenvector) satisfying $Lv = \lambda v$. The smallest eigenvalue of L is always zero, and the multiplicity of zero equals the number of connected components of the graph.

For directed graphs, the degree matrix K can be defined either using the out-degrees or the in-degrees of the nodes, leading to different versions of the Laplacian. These matrices are generally not symmetric, and their spectral properties require separate analysis.

Definition 2.2.10 (Algebraic connectivity) *The algebraic connectivity of an undirected graph is the second-smallest eigenvalue* λ_2 *of its Laplacian matrix* L*. A graph is connected if and only if* $\lambda_2 > 0$*.*

2.3 Topological measures

The structure of a network can be quantitatively described through a variety of topological measures [10], each capturing a specific aspect of the organization of connections among nodes. Some of these measures characterise the network at the *local* level, focusing on the properties of individual nodes or small groups of nodes, while others describe *global* properties involving the entire network. These indicators are widely used to compare different networks, to study the relationship between topology and dynamics, and to evaluate the performance of generative models in reproducing observed structures. In what follows, the main definitions and notations relevant to the mathematical description of network structures and dynamics are presented.

2.3.1 Degree and degree distribution

The *degree* of a node i, denoted by k_i, as introduced in Definition 2.2.8, counts the number of links incident to the node in an undirected network, or distinguishes between incoming and outgoing links in a directed network. A structural indicator of connectivity is given by the *average degree*

$$\langle k \rangle = \frac{1}{N} \sum_{i=1}^{N} k_i, \tag{2.1}$$

which represents the mean number of connections per node.

The *degree distribution* $P(k)$ is the fraction of nodes having degree k, i.e.

$$P(k) = \frac{n_k}{N} \quad \text{with} \sum_{k=0}^{k_{\max}} P(k) = 1, \tag{2.2}$$

where n_k is the number of nodes with degree k.

A related, aggregated representation is the *cumulative degree distribution*,

$$F(k) = \sum_{k'=0}^{k} P(k') = \Pr(K \leq k), \tag{2.3}$$

where K denotes the random variable representing the node degree, and its complement, the *complementary cumulative degree distribution*,

$$\bar{F}(k) = \sum_{k'=k}^{k_{\max}} P(k') = \Pr(K \geq k) = 1 - F(k-1). \tag{2.4}$$

They highlight different features, for instance the behavior of large-degree nodes, and mitigate the effects of sampling noise. In the discrete, noise-free setting they determine $P(k)$ via finite differences, but in empirical analyzes they are not strictly interchangeable due to aggregation and estimation effects. Many engineered infrastructures tend to have narrow degree distributions, whereas biological or self-organised systems often display broad, heavy-tailed forms.

2.3.2 Shortest path length and average shortest path length

The *shortest path length* D_{ij} between two nodes i and j is the minimal number of edges that must be traversed to connect them, or the minimal sum of weights in the weighted case. The *average shortest path length* D is then defined as

$$D = \frac{1}{N(N-1)} \sum_{i \neq j} D_{ij}, \tag{2.5}$$

quantifying the mean geodesic distance between pairs of nodes in the network.

This measure is related to the efficiency of information transfer or transport processes: low values indicate that any two nodes are, on average, connected by few intermediates; otherwise, high values suggest that information or resources must traverse longer routes, which can increase communication delays and reduce the overall efficiency of the system.

2.3.3 Clustering coefficient

The *clustering coefficient* quantifies the tendency of a node's neighbors to also be connected to each other. The *local* clustering coefficient of node i is defined as

$$C_i = \frac{2e_i}{k_i(k_i-1)}, \tag{2.6}$$

where e_i is the number of edges between the neighbors of node i and k_i its degree. This measure captures the density of connections among the neighbors of a specific node. The *global* clustering coefficient is a network-level metric defined as

$$C = \frac{3 \times \text{number of closed triangles}}{\text{number of connected triplets of nodes}}. \tag{2.7}$$

High clustering values indicate the presence of tightly connected groups, a feature common in both social and biological systems and relevant in the analysis of synchronization and robustness; otherwise, low values suggest a more tree-like or loosely connected structure with fewer closed loops.

2.3.4 Modularity

Modularity Q quantifies the extent to which a network can be decomposed into modules, or communities, characterised by dense internal connections and sparser links between different modules [79]. Given a partition of the network into distinct communities, the modularity is defined as

$$Q = \frac{1}{2W} \sum_{i,j} \left(a_{ij} - \frac{k_i k_j}{2W} \right) \delta(c_i, c_j), \tag{2.8}$$

where W is the total number of edges (or the sum of all edge weights if the graph is weighted); a_{ij} is equal to 1 when the link between nodes i and j exists (or $w_{ij} \in \mathbb{R}$ in the weighted case), and 0 otherwise; k_i and k_j are the respective degrees; c_i and c_j denote the communities of nodes i and j; finally $\delta(c_i, c_j)$ is the Kronecker delta, equal to 1 if the two nodes belong to the same community and 0 otherwise.

High modularity values indicate a pronounced community structure, with more intra-community edges than expected at random, whereas low values suggest a more homogeneous or random connectivity pattern without a clear modular organization.

2.3.5 Rent exponent

In spatially embedded networks, the interplay between geometric constraints and connection costs strongly influences topological organization. A key descriptor of this relationship is the *Rent exponent* ρ [27], a scaling exponent relating the number of nodes contained in a subregion of the network to the number of connections crossing its boundary. The Rent exponent is defined thorugh the following expression:

$$E_{\text{boundary}} \propto N_{\text{subset}}^{\rho},$$

where E_{boundary} is the number of edges crossing the boundary of the subregion, and N_{subset} is the number of nodes contained within it.

Lower exponents indicate a stronger localisation of connections, whereas higher values correspond to more distributed connectivity.

Closely related to Rent's scaling are measures such as *wiring cost*, defined as the total Euclidean distance of all connections in the network, and *spatial efficiency* [63], which compares shortest-path distances to Euclidean separations between node pairs. While wiring cost captures the resource expenditure required to physically implement the network, spatial efficiency reflects how effectively spatial proximity is translated into short topological paths. Together, these measures provide complementary insights into how networks balance the minimisation of physical resources with the need for efficient communication.

2.4 Hypergraphs and simplicial complexes

Network is modelled as a set of vertices connected by edges, each edge describing a *pairwise link* between two units. This framework is appropriate for systems where interactions occur strictly in pairs, as in engineered infrastructures such as power grids or communication networks. However, in many natural and biological systems, collective behavior cannot be fully explained by pairwise interactions alone. Examples include coordinated activity in neural populations, or structural dependencies among multiple brain regions revealed by tractography data. In such cases, more general mathematical structures are needed to represent interactions that involve groups of three or more units.

To capture these *higher-order* relations, it is useful to adopt the formalism of hypergraphs and simplicial complexes. This approach extends the standard graph model by including not only edges, but also higher-dimensional elements that explicitly represent multi-node interactions.

Definition 2.4.1 (Hypergraph) *A hypergraph is a pair* $\mathcal{H} = (\mathcal{V}, \mathcal{E})$*, where* $\mathcal{V}$ *is a set of nodes and* $\mathcal{E}$ *is a set of hyperedges. Each hyperedge* $e \in \mathcal{E}$ *is* *a subset of two or more nodes, and may involve any number of vertices simultaneously. Depending on the application, hyperedges can be weighted or unweighted, directed or undirected.*

Definition 2.4.2 (Simplicial complex) *A simplicial complex $\mathcal{K}$ over a set of vertices $\mathcal{V}$ is a collection of simplices such that if a simplex σ belongs to $\mathcal{K}$, then all its faces also belong to $\mathcal{K}$. A d-simplex is an unordered set of $d + 1$ vertices, for example: a 0-simplex is a vertex, a 1-simplex an edge, a 2-simplex a filled triangle, and so on. By construction, simplicial complexes impose the condition that all lower-dimensional subsets of a simplex are also included in the complex. This makes them a specific subclass of hypergraphs.*

Hypergraphs allow maximum flexibility by admitting arbitrary groupings of nodes, while simplicial complexes add the constraint of closure under faces, which is often convenient for mathematical and topological analysis. Both representations can describe higher-order interactions and can be weighted or unweighted, directed or undirected, depending on the system considered.

The choice between hypergraphs and simplicial complexes depends on the context: hypergraphs are natural for modeling general group relations without further structural assumptions, while simplicial complexes are particularly useful when hierarchical inclusion of interactions is required. In this thesis, both frameworks will be employed in the analysis of higher-order reconstruction methods (see Chapter 3), where pairwise and multi-node dependencies are inferred directly from empirical time-series data.

2.5 Networks and hypernetworks of dynamical systems

Many complex systems consist of units whose states evolve over time according to intrinsic dynamical laws, while being influenced by their interactions with other units. A convenient mathematical representation associates each node i with a state vector $\mathbf{x}_i \in \mathbb{R}^m$, where m is the dimension of the local state, namely the number of variables needed to describe its dynamics. The evolution of these states is governed by a set of equations, and the pattern of interactions, encoded by the network or hypernetwork topology, determines how information, energy, or other quantities flow between nodes, shaping the collective behavior of the system. Depending on the nature of the units and the *coupling* mechanism, namely the way in which the state of one node influences others, the dynamics may evolve in continuous or discrete time, be linear or nonlinear, and follow deterministic or stochastic rules.

A general form [19] for a continuous-time networked dynamical system is

$$\dot{\mathbf{x}}_i = F(\mathbf{x}_i) + \sigma \sum_{j=1}^{N} a_{ij} H(\mathbf{x}_j, \mathbf{x}_i), \tag{2.9}$$

where:

- $F : \mathbb{R}^m \to \mathbb{R}^m$ describes the intrinsic (uncoupled) dynamics of each node;
- $\sigma \in \mathbb{R}$ is the coupling strength;
- a_{ij} are the elements of the adjacency matrix, representing the network structure;
- $H : \mathbb{R}^m \times \mathbb{R}^m \to \mathbb{R}^m$ specifies the coupling function between two connected nodes.

In discrete time, where $t \in \mathbb{Z}$ denotes the discrete time step, the equivalent formulation is

$$\mathbf{x}_i(t+1) = F(\mathbf{x}_i(t)) + \sigma \sum_{j=1}^{N} a_{ij} H(\mathbf{x}_j(t), \mathbf{x}_i(t)). \tag{2.10}$$

Instead, in the case of hypernetworks, the general equations are

$$\dot{\mathbf{x}}_i = F(\mathbf{x}_i) + \sigma^{(1)} \sum_{j=1}^{N} a_{ij}^{(1)} H^{(1)}(\mathbf{x}_j, \mathbf{x}_i) + \sigma^{(2)} \sum_{j,k=1}^{N} a_{ijk}^{(2)} H^{(2)}(\mathbf{x}_j, \mathbf{x}_k, \mathbf{x}_i) + \dots, \tag{2.11}$$

where $a_{ij}^{(1)}$ are the entries of the adjacency matrix describing pairwise couplings, $a_{ijk}^{(2)}$ are the entries of a three-way adjacency tensor encoding group interactions among triples of nodes, $\sigma^{(1)}, \sigma^{(2)}$ are coupling strengths at different orders, and $H^{(1)}, H^{(2)}$ denote the corresponding coupling functions. This formulation naturally extends to higher orders, providing a flexible framework to model systems where collective effects cannot be decomposed into independent pairwise contributions.

Once introduced the general paradigm for both networked and hypernetworked systems, we discuss a few examples that will be used in the following.

2.5.1 Networked systems of Rössler units

The *Rössler system* [97] is a paradigmatic model of continuous-time chaotic dynamics, widely used to investigate nonlinear phenomena such as synchronization in networked systems. For node i, the isolated dynamics are given by

$$\begin{aligned}\dot{\mathbf{x}}_i(t) &= -y_i(t) - z_i(t),\\ \dot{\mathbf{y}}_i(t) &= x_i(t) + a\, y_i(t),\\ \dot{\mathbf{z}}_i(t) &= b + z_i(t)\left(x_i(t) - c\right),\end{aligned} \tag{2.12}$$

where a, b, and c are real-valued parameters that determine the qualitative behavior of the oscillator, including the onset of chaos. The system exhibits a chaotic attractor characterised by a single unstable focus and a spiralling trajectory in phase space.

When embedded in a network, the dynamics of node i take the form

$$\begin{aligned}\dot{x}_i(t) &= -y_i(t) - z_i(t) + \sigma \sum_{j=1}^{N} a_{ij}\left(x_j(t) - x_i(t)\right),\\ \dot{y}_i(t) &= x_i(t) + a\, y_i(t),\\ \dot{z}_i(t) &= b + z_i(t)\left(x_i(t) - c\right),\end{aligned} \tag{2.13}$$

where σ denotes the *coupling strength* and a_{ij} are the entries of the adjacency matrix that encode the network structure. This configuration, based on diffusive coupling through the x-component, is commonly adopted to study how intrinsic chaotic dynamics combine with inter-node interactions to generate collective behaviors such as synchronization.

More generally, when higher-order interactions are present, the system can be represented as a *hypernetwork*, where multi-node dependencies are encoded by adjacency tensors. In this case, the dynamics of node i can be written as

$$\dot{\mathbf{x}}_i = F(\mathbf{x}_i) + \sigma_1 \sum_{j=1}^{N} A^{(1)}_{ij}\, g^{(1)}(\mathbf{x}_i, \mathbf{x}_j) + \sigma_2 \sum_{j,k=1}^{N} A^{(2)}_{ijk}\, g^{(2)}(\mathbf{x}_i, \mathbf{x}_j, \mathbf{x}_k), \tag{2.14}$$

where $F(\mathbf{x}_i)$ denotes the intrinsic Rössler dynamics, $A^{(1)}$ and $A^{(2)}$ are respectively the adjacency matrix and adjacency tensor encoding pairwise and three-body interactions, and $g^{(1)}$, $g^{(2)}$ are the corresponding coupling functions. This formulation allows the simultaneous consideration of standard pairwise links and genuine multi-node interactions within the same dynamical framework.

Specifically, Eq. (2.14) instantiates the general hypernetwork model in Eq. (2.11) for Rössler oscillators with first and second order couplings only, with the notational correspondence $F = f_{\text{Rössler}},\ H^{(r)} = g^{(r)},\ a^{(r)} = A^{(r)}$ for $r \in \{1, 2\}$. The gains σ_1 and σ_2 correspond to $\sigma^{(1)}$ and $\sigma^{(2)}$, respectively; this alignment is purely notational and leaves all derivations unchanged.

In this thesis, the Rössler system is used in Chapter 3.6 as a chaotic benchmark for testing reconstruction methods capable of recovering both pairwise and higher-order interactions in continuous-time systems, and in Chapter 5 as a nonlinear testbed within the so-called edge snapping framework, an adaptive strategy for link activation aimed at achieving synchronization under resource constraints.

2.5.2 Networked systems of Kuramoto oscillators and swing equations

The *Kuramoto model* [43, 1] captures the essential features of phase synchronization in a population of coupled oscillators through a minimal yet analytically tractable framework. Each unit is described by a single scalar phase $\theta_i \in [0, 2\pi)$ evolving as

$$\dot{\theta}_i(t) = \omega_i + \frac{\sigma}{N} \sum_{j=1}^{N} a_{ij} \sin\big(\theta_j(t) - \theta_i(t)\big), \tag{2.15}$$

where ω_i is the natural frequency of oscillator i; σ is the coupling strength; and a_{ij} are the entries of the adjacency matrix encoding the network structure. The model describes the competition between the intrinsic tendency of each oscillator to evolve at its own frequency and the tendency to synchronise induced by the coupling.

In the context of power system dynamics, the electromechanical behavior of synchronous machines is described by the *swing equations* [80], which model the time evolution of the voltage phase angle $\theta_i(t)$ and the angular velocity $\omega_i(t)$ of generator i with respect to a synchronous reference frame. The equations, in accordance with the definition introduced in 2.1, take the form

$$\begin{aligned} \dot{\theta}_i(t) &= \omega_i(t), \\ I_i\dot{\omega}_i(t) + \gamma_i\omega_i(t) &= P_{m_i} - P_{e_i}, \end{aligned} \tag{2.16}$$

where I_i is the moment of inertia, γ_i is the damping coefficient, P_{m_i} is the mechanical input power, and P_{e_i} is the electrical output power. The latter depends on the voltage phase differences between connected machines and on the network topology, and in power grid models is typically expressed as

$$P_{e_i} = \sum_{j=1}^{N} \kappa_{ij} \sin\big(\theta_i(t) - \theta_j(t)\big), \tag{2.17}$$

with κ_{ij} determined by the line admittance and voltage magnitudes. This formulation is mathematically equivalent to a second-order Kuramoto model, where the acceleration term accounts for the inertia of the rotors and the damping term models energy dissipation.

In this thesis, Kuramoto dynamics and the swing equations are used in Section 3.8 to investigate coupled oscillator behavior in settings ranging from theoretical phase models to power system dynamics, while Chapter 5 focuses on swing equations to examine cascading failures, namely the sequential tripping of multiple components, in electrical grids.

2.5.3 Hypernetworked systems of Lotka–Volterra populations

The *Lotka–Volterra model* [25] describes the population dynamics of interacting species through coupled nonlinear differential equations, and has been extensively applied in theoretical ecology and related fields. In its generalised form, incorporating both pairwise and three-body interactions, the dynamics of species i can be expressed as

$$\dot{x}_i(t) = r_i x_i(t)\left(1 - \frac{x_i(t)}{K_i}\right) + \sum_{j=1}^{N} a_{ij}^{(1)} x_i(t)x_j(t) + \sum_{j=1}^{N}\sum_{k=j+1}^{N} a_{ijk}^{(2)} x_i(t)x_j(t)x_k(t), \tag{2.18}$$

where $x_i(t)$ is the abundance of species i at time t; r_i is its intrinsic growth rate; K_i is the carrying capacity; $a_{ij}^{(1)}$ are the pairwise interaction coefficients; and $a_{ijk}^{(2)}$ are the coefficients for three-species interactions. This extension from pairwise to higher-order terms allows the model to capture collective effects that cannot be reduced to independent two-species contributions, such as facilitation or inhibition emerging only in the presence of a third species.

In this thesis, the Lotka–Volterra model is employed in Section 3.7 to represent microbial ecosystems whose interaction structure includes both pairwise and higher-order terms. This formulation provides the dynamical framework for testing reconstruction methods capable of inferring not only direct pairwise interactions but also group effects encoded in higher-order connectivity patterns.

2.5.4 Networked systems of Minati–Frasca oscillators

The *Minati–Frasca oscillator* [74, 73, 75] is a compact chaotic electronic circuit designed to operate at low voltages while exhibiting rich nonlinear behavior. The circuit, shown in Fig. 2.1, is composed of an NPN bipolar junction transistor, acting as the active nonlinear element, two inductors L_1 and L_2, a main capacitor C_1 together with an auxiliary smaller capacitor C_2, which provides additional high-frequency coupling and contributes to shaping the circuit's nonlinear dynamics, and a resistor R that both limits the current flow and dissipates energy. A constant voltage source V_s, applied through the resistor R, supplies the circuit. The four passive elements are all connected to a common node. The second terminal of C_1 is grounded, while the other terminals of L_1 and L_2 are connected to the base and collector of the transistor, whose emitter is also grounded.

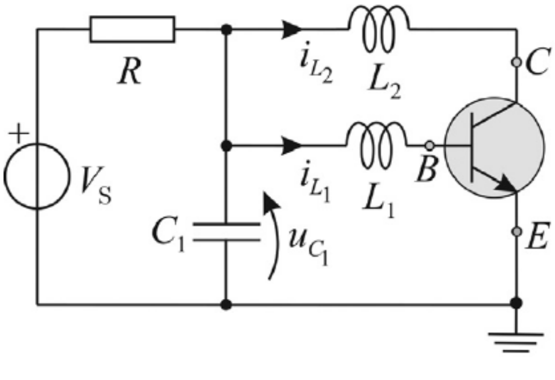

Figure 2.1: Electrical scheme of the transistor-based chaotic oscillator.

This oscillator was originally introduced in [73] and has since been the subject of various studies highlighting its capability to generate chaotic behavior and its underlying mechanisms. A representative parameter set is the following:

$$\begin{aligned} L_1 &= 15 \times 10^{-6}\,\mathrm{H}, & L_2 &= 220 \times 10^{-6}\,\mathrm{H}, \\ C_1 &= 220 \times 10^{-12}\,\mathrm{F}, & C_2 &= 5 \times 10^{-12}\,\mathrm{F}, \\ R &= 1000\,\Omega, & V_s &= 2\,\mathrm{V}. \end{aligned} \tag{2.19}$$

A rigorous physical description of the circuit would require a detailed modeling of the transistor behavior across its operating regions. Such an approach, however, would reduce interpretability and analytical tractability. In analogy with other compact representations of chaotic electronic oscillators, such as the Colpitts oscillator [61], a simplified but effective model was proposed in [75]. Under suitable approximations derived from inspection of the experimental dynamics, the model is written as

$$\begin{aligned} \frac{dv_1}{dt} &= \frac{V_s - v_1}{RC_1} - \frac{i_{L1} + i_{L2}}{C_1}, \\ \frac{dv_2}{dt} &= \frac{i_{L2} - \beta\,\Gamma(i_{L1})\tanh\big(v_2/(2V_t)\big)}{C_2}, \\ \frac{di_{L1}}{dt} &= \frac{v_1 - V_t}{L_1}, \\ \frac{di_{L2}}{dt} &= \frac{v_1 - v_2}{L_2}, \end{aligned} \tag{2.20}$$

with $\Gamma(x) = x$ if $x > 0$, and $\Gamma(x) = 0$ otherwise.

For the analytical developments, it is convenient to work with a rescaled dimensionless formulation. Introducing the following change of variables:

$$\begin{aligned} x_1 &= k_V v_1, \\ x_2 &= k_V v_2, \\ x_3 &= k_I i_{L1}, \\ x_4 &= k_I i_{L2}, \\ t' &= \tau t. \end{aligned} \tag{2.21}$$

with $k_V = 1\,\mathrm{V}^{-1}$, $k_I = 1000\,\mathrm{A}^{-1}$, and $\tau = 10^6\,\mathrm{s}^{-1}$, the compact model reads

$$\begin{aligned}
\dot{x}_1 &= \frac{a - x_1}{bg} - \frac{x_3 + x_4}{b}, \\
\dot{x}_2 &= \frac{x_4 - \beta\,\Gamma(x_3)\tanh(x_2/(2d))}{c}, \\
\dot{x}_3 &= \frac{x_1 - d}{e}, \\
\dot{x}_4 &= \frac{x_1 - x_2}{f},
\end{aligned} \tag{2.22}$$

where $\dot{x} = dx/dt'$, and

$$\begin{aligned}
a &= k_V V_s = 2, \\
b &= \tau k_I C_1 = 0.220, \\
c &= \tau k_I C_2 = 0.005, \\
d &= k_V V_t = 0.6, \\
e &= \frac{L_1 \tau k_V}{k_I} = 0.015, \\
f &= \frac{L_2 \tau k_V}{k_I} = 0.220, \\
g &= \frac{R k_V}{k_I} = 1.
\end{aligned} \tag{2.23}$$

Model (2.22), with the parameters given in (2.23), reproduces chaotic oscillations consistent with the experimental behavior. Representative numerical simulations are illustrated in Fig. 2.2, showing both time series of the state variables and projections of the attractor. These results confirm that a compact modeling approach allows to capture the essential chaotic dynamics while preserving analytical interpretability.

To investigate the collective behavior of multiple oscillators, the circuits can be coupled through resistors inserted between the central nodes, as illustrated in Fig. 2.3. This implements diffusive coupling, namely a bidirectional and symmetric interaction mechanism commonly observed in systems that display synchronization.

Let the two circuits in Fig. 2.3 be indicated as i and j, with state variables $v_1^{(i)}, v_2^{(i)}, i_{L1}^{(i)}, i_{L2}^{(i)}$ and $v_1^{(j)}, v_2^{(j)}, i_{L1}^{(j)}, i_{L2}^{(j)}$, respectively. Using the scaling

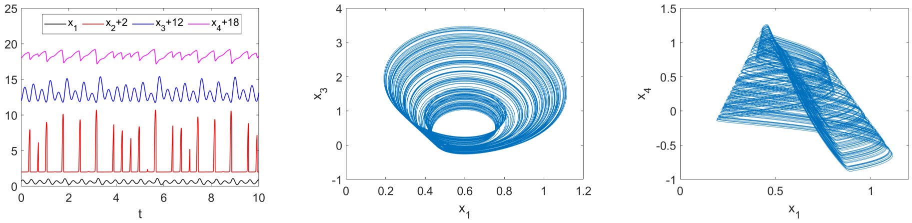

Figure 2.2: Numerical integration of Eqs. (2.22) showing chaotic behavior of the transistor-based chaotic circuit. (a) Time evolution of the state variables $x_i(t)$ with $i = 1, \ldots, 4$. (b) Projection of the attractor onto the plane (x_1, x_3). (c) Projection of the attractor onto the plane (x_1, x_4).

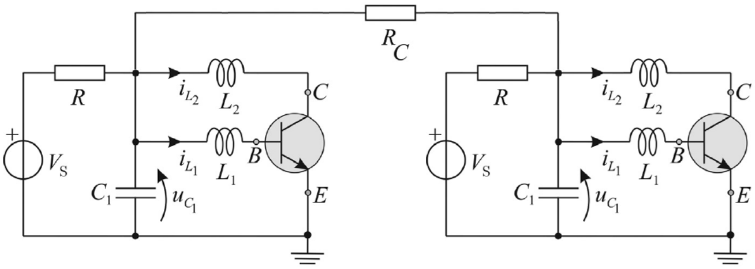

Figure 2.3: Electrical scheme of two coupled transistor-based chaotic oscillators.

in Eq. (2.21), the dimensionless coupled model is

$$\begin{aligned}
\dot{x}_1^{(i)} &= \frac{a - x_1^{(i)}}{bg} - \frac{x_3^{(i)} + x_4^{(i)}}{b} + \sigma \frac{x_1^{(j)} - x_1^{(i)}}{b}, \\
\dot{x}_2^{(i)} &= \frac{x_4^{(i)} - \beta\, \Gamma(x_3^{(i)}) \tanh(x_2^{(i)}/(2d))}{c}, \\
\dot{x}_3^{(i)} &= \frac{x_1^{(i)} - d}{e}, \\
\dot{x}_4^{(i)} &= \frac{x_1^{(i)} - x_2^{(i)}}{f}, \\
\dot{x}_1^{(j)} &= \frac{a - x_1^{(j)}}{bg} - \frac{x_3^{(j)} + x_4^{(j)}}{b} + \sigma \frac{x_1^{(i)} - x_1^{(j)}}{b}, \\
\dot{x}_2^{(j)} &= \frac{x_4^{(j)} - \beta\, \Gamma(x_3^{(j)}) \tanh(x_2^{(j)}/(2d))}{c}, \\
\dot{x}_3^{(j)} &= \frac{x_1^{(j)} - d}{e}, \\
\dot{x}_4^{(j)} &= \frac{x_1^{(j)} - x_2^{(j)}}{f},
\end{aligned} \tag{2.24}$$

where $\sigma = \dfrac{k_I}{R_C k_V}$ and R_C is the coupling resistor.

Eqs. (2.24) naturally extend to $N > 2$ coupled circuits. Let $A = \{a_{ij}\}$ denote the adjacency matrix of a simple, undirected graph representing the couplings among the N circuits, with $a_{ij} = 1$ if i and j are connected, and $a_{ij} = 0$ otherwise, and $a_{ii} = 0$ for all i. The network model reads

$$\begin{aligned}
\dot{x}_1^{(i)} &= \frac{a - x_1^{(i)}}{bg} - \frac{x_3^{(i)} + x_4^{(i)}}{b} + \sigma \sum_{j=1}^{N} a_{ij} \frac{x_1^{(j)} - x_1^{(i)}}{b}, \\
\dot{x}_2^{(i)} &= \frac{x_4^{(i)} - \beta\,\Gamma(x_3^{(i)}) \tanh\big(x_2^{(i)}/(2d)\big)}{c}, \\
\dot{x}_3^{(i)} &= \frac{x_1^{(i)} - d}{e}, \\
\dot{x}_4^{(i)} &= \frac{x_1^{(i)} - x_2^{(i)}}{f},
\end{aligned} \tag{2.25}$$

with identical coupling resistors, such that σ is independent of the pair (i, j).

This networked configuration allows to investigate how the intrinsic chaotic dynamics of individual oscillators combine with the structural properties of the graph to produce collective behaviors such as synchronization.

In this thesis, the Minati–Frasca oscillator is used in Chapter 6 to investigate the interplay between coupling strength and network topology in determining synchronization stability [20]. The Master Stability Function (MSF) – a tool for the analysis of synchronization – is computed for the circuit dynamics and employed to predict synchronization stability regimes without the need for full-network simulations, enabling a direct comparison between analytical predictions and experiments.

Part I

Network modeling

Chapter 3

Reconstruction

3.1 Introduction

The problem of reconstructing the interaction structure of a complex system from observations of its dynamics is central to network science and to the modeling of both artificial and natural systems. In its most general formulation, reconstruction addresses the so-called inverse problem [98], which consists in inferring the underlying coupling pattern responsible for the observed behavior from time series of the states of the system's units. This task is fundamental in domains ranging from engineering to neuroscience and systems biology, where understanding the precise connectivity between components enables accurate modeling, prediction of emergent phenomena, and the design of effective control strategies.

In traditional approaches, attention has mostly been restricted to pairwise interactions, where the system is modelled as a graph and the topology is encoded in a single adjacency matrix. However, many real systems cannot be faithfully described in such a framework, as they exhibit higher-order interactions, namely simultaneous couplings among three or more units [57, 5, 48, 46]. These collective mechanisms are not reducible to the superposition of pairwise effects, and neglecting them can lead to severe mischaracterizations of both structural and dynamical properties. Furthermore, in many applications the topology is not static but evolves over time, either adaptively or due to failures and external perturbations, as in power grids subject to cascading failures [42, 90, 111]. In such cases, the reconstruction problem extends beyond identifying a static network to capturing the time-varying active set of connections.

Since empirical measurements are often noisy, incomplete, or sparsely sampled, reconstruction algorithms must be robust to uncertainty, efficient in extracting information from limited data, and capable of exploiting any available prior knowledge, such as the form of the dynamical equations or partial information about the underlying structure.

3.2 State of the art

Existing approaches to network reconstruction can be categorised according to the type of connectivity they target [98]. Functional connectivity captures statistical dependencies between the states of the units, as shaped by their dynamical interactions [99]. It can be inferred through measures such as pairwise correlations, mutual information, Granger causality [62, 109], transfer entropy [91, 104], or Bayesian inference [58], and may vary with the dynamical regime of the system. Structural connectivity, in contrast, describes the physical or effective couplings themselves. Methods for its inference include the analysis of the system's response to external perturbations [98], adaptive synchronization with a model copy whose links evolve toward those of the original system [113, 108], and the formulation of optimization problems based on time-series measurements when the functional form of the node dynamics is known [93, 94].

While a variety of statistical and model-based techniques have been developed for pairwise networks, the case of higher-order interactions remains less explored [85]. Recent works have distinguished between higher-order mechanisms, namely explicit terms in the microscopic interaction structure, and higher-order behaviors, that is, correlations emerging in the dynamics even without genuine multi-node couplings. The latter can arise, for example, in purely pairwise systems with specific topologies, and disentangling these effects is a non-trivial task. Information-theoretic methods, generalizations of causality measures [82], and simplicial filtration procedures [88] have been proposed to capture patterns beyond pairwise dependencies, while statistical significance tests for hyperlinks and Bayesian reconstructions from link activity data represent complementary strategies [112, 67].

In parallel, the problem of reconstructing time-varying connectivity has been studied in contexts such as adaptive networks and infrastructure systems under perturbations [50]. In particular, in power grids, the interplay between the dynamical redistribution of flows and the protection mechanisms of the lines can lead to sequences of failures that reshape the operative topology [42, 90, 111]. Identifying the set of active lines at each moment is crucial for real-time monitoring and control.

3.3 Reconstruction in higher–order structures

A general framework for reconstructing both pairwise and higher-order interactions in continuous-state systems builds upon the formulation introduced in Eq. (2.11), where the dynamics of each unit are expressed as the sum of an intrinsic contribution and interaction terms of increasing order. In this representation, F specifies the uncoupled dynamics of node i, the functions $g^{(d)}$ capture the effect of $(d+1)$-body couplings, and the coefficients $a^{(d)}_{ij_1\dots j_d}$ are the entries of the adjacency tensors $\mathbf{A}^{(d)}$ encoding the structural connectivity at each order. The goal is to recover all non-zero entries of $\mathbf{A}^{(d)}$ from sampled trajectories $\mathbf{x}_i(t_m)$, $m = 0, \dots, M$.

If the derivatives $\dot{\mathbf{x}}_i(t_m)$ are available, Eq. (2.11) can be written at each time t_m as

$$\mathbf{y}_i^m = \mathbf{z}_i^m - F(\mathbf{x}_i^m) = \sum_{d=1}^{D} \sum_{j_1,\dots,j_d=1}^{N} a^{(d)}_{ij_1\dots j_d}\, g^{(d)}(\mathbf{x}_i^m, \mathbf{x}_{j_1}^m, \dots, \mathbf{x}_{j_d}^m), \tag{3.1}$$

with $\mathbf{x}_i^m := \mathbf{x}_i(t_m)$ and $\mathbf{z}_i^m := \dot{\mathbf{x}}_i(t_m)$. When derivatives are not available from direct measurements, they are estimated from the sampled trajectories using standard finite-difference schemes with first-, second-, or fourth-order accuracy, chosen to balance computational simplicity, numerical precision, and robustness to noise.

Stacking all time points into the vector $\mathbf{y}_i$ and all unknown interaction coefficients for node i into $\mathbf{a}_i$, the problem becomes the linear system

$$\mathbf{y}_i = \mathbf{\Phi}_i \mathbf{a}_i, \tag{3.2}$$

where the regression matrix $\mathbf{\Phi}_i$ contains the evaluated coupling functions $g^{(d)}$ for all index combinations. The total number of unknowns for node i is

$H = (N-1) + (N-1)(N-2) + \cdots + (N-1)\dots(N-D)$, reduced when symmetries apply. If the number of equations M exceeds H and $\boldsymbol{\Phi}_i$ has full column rank, $\mathbf{a}_i$ can be recovered uniquely by least squares; otherwise, regularisation is required.

Different optimization schemes can be adopted:

- OLS: ordinary least squares, returning the minimal ℓ_2-norm solution when multiple minimisers exist.

- NNLS: non-negative least squares [65], imposing $\mathbf{a}_i \geq 0$ when coefficients are known to be non-negative.

- SL: signal Lasso [94], solving

  $$\min_{\mathbf{a}_i} \; \tfrac{1}{2}\|\mathbf{y}_i - \boldsymbol{\Phi}_i \mathbf{a}_i\|_2^2 + \alpha\|\mathbf{a}_i\|_1 + \beta\|\mathbf{a}_i - \mathbf{1}_H\|_1$$

  to promote sparsity and shrinkage toward a target.

This framework applies to both hypergraphs and simplicial complexes, directed or undirected, weighted or unweighted. Directed formulations allow node-by-node minimisation of the discrepancy, while undirected cases require symmetry constraints.

3.4 Reconstruction of cascading network failures

While multi-node couplings can shape the dynamics through higher-order structures, in many systems interactions are exclusively pairwise and embedded in a fixed backbone, yet the set of active links changes over time. We discuss this case study with reference to the equations of the power grids, where the problem finds relevant application. In such systems, the topology may be known a priori, but the set of active links evolves over time due to faults.

In a synchronous-machine representation of a power grid, the node dynamics follow the swing equations already introduced in Eq. (2.16), which describe the evolution of phase angle and angular velocity under inertia, damping, and power balance. On top of this baseline model, faults and cascading failures can be incorporated by introducing a binary activity variable a_{ij} associated with each transmission line. A line (i, j) is considered active when $a_{ij} = 1$ and shut down when $a_{ij} = 0$, according to the overload condition

$$F_{ij}(t) = a_{ij} \sin(\theta_j - \theta_i) > C_{ij} = \alpha \kappa_{ij}, \tag{3.3}$$

where $F_{ij}(t)$ is the instantaneous power flow and C_{ij} is the line capacity proportional to its coupling coefficient κ_{ij}. This extension allows the representation of dynamically changing topologies, where successive line trippings can propagate through the network, leading to cascading failures.

The reconstruction task is to determine, from measurements of $\theta_i(t)$ and $\omega_i(t)$, which of the known links are active at a given time. Discretising Eq. (2.16) over an interval Δt yields

$$r_i(h) = I_i \frac{\omega_i(h+1) - \omega_i(h)}{\Delta t} - P_i + \gamma_i \omega_i(h) = \kappa \sum_{j \in \mathcal{N}_i} a_{ij} \sin(\theta_j(h) - \theta_i(h)), \tag{3.4}$$

where $\mathcal{N}_i$ is the set of k_i neighbors of i in the known topology.

Collecting all time points, the problem can be written in the linear form

$$\mathbf{r}_i = \mathbf{\Phi}_i \mathbf{a}_i, \tag{3.5}$$

where $\mathbf{r}_i$ contains the measured terms, $\mathbf{\Phi}_i$ the evaluated coupling functions, and $\mathbf{a}_i$ the unknown coefficients to be inferred. Restricting to the k_i possible neighbors of node i, the regression matrix reduces to $\mathbf{\Phi}'_i \in \mathbb{R}^{M \times k_i}$ with entries $\Phi'_{i,m\ell} = \kappa \sin(\theta_{j_\ell}(h_m) - \theta_i(h_m))$. The system is overdetermined if $M > k_i$, which is typically easy to achieve.

This formulation allows the active topology of a network with known backbone to be inferred efficiently, enabling the identification of structural changes driven by dynamical events such as cascading failures, and offering a basis for timely interventions and control strategies.

3.5 Methodological procedure

Both the inference of higher-order interactions and the identification of active links in networks with a known backbone can be formulated as linear inverse problems, where measured or estimated dynamical quantities are expressed as combinations of unknown coupling coefficients. In both cases, the algorithm operates locally at each node, constructing an observation vector from the available time series and a regression matrix from the known form of the interactions, and solving for the coefficients under appropriate constraints.

The reconstruction procedure can be summarised as follows:

1. For each node i, assemble $\mathbf{y}_i$ from the measured or approximated derivatives (higher-order case) or from the discretised swing equations (active-link case).
2. Build the regression matrix $\mathbf{\Phi}_i$ (or $\mathbf{\Phi}'_i$) from the evaluated coupling functions using the sampled trajectories.
3. Solve $\mathbf{y}_i = \mathbf{\Phi}_i \mathbf{a}_i$ with the appropriate optimization method (OLS, NNLS, SL) depending on the problem constraints and prior knowledge.
4. In undirected networks, enforce $a_{ij} = a_{ji}$ by symmetrising the result; when reconstructing active links, merge the outcomes for i and j using logical OR to reduce false negatives.

In the *higher-order* setting, the same linear structure $\mathbf{y}_i = \mathbf{\Phi}_i \mathbf{a}_i$ is used, but $\mathbf{\Phi}_i$ includes higher-order terms (e.g., tensorial combinations) and symmetry constraints.

Algorithm 1: Algorithm for local network reconstruction (active-link case)

```
Input: $\theta_i(h), \omega_i(h), i = 1, \dots, N, h = h_1, \dots, h_M$
Output: coefficients of the adjacency matrix at time $t = h_M \Delta t$, i.e., $a_{ij}^{II}$
Procedure:
for $i = 1, \dots, N$ do
    Write $\mathbf{y}_i = \mathbf{\Phi}'_i \mathbf{a}'_i$
    if Eq. 3 is consistent then
        solve Eq. 3, using $\mathbf{a}'_i = \mathbf{\Phi}'^{+}_i \mathbf{y}_i$, to determine $a_{ij}^{I}, j = j_1, \dots, j_{k_i}$
            // where $\mathbf{\Phi}'^{+}_i$ is the Moore--Penrose pseudo-inverse of $\mathbf{\Phi}'_i$
    else
        set $a_{ij}^{I} = 0, j = j_1, \dots, j_{k_i}$
    end
end
calculate $a_{ij}^{II} = a_{ij}^{I} \vee a_{ji}^{I}, \forall i, j$
return $a_{ij}^{II}, \forall i, j$
```

3.6 Applications to Rössler networks with higher-order dynamics

In order to extend the analysis to continuous–time chaotic dynamics, a system of Rössler oscillators, already introduced in Section 2.5.1, with both pairwise and three–body interactions is considered. This example allows the reconstruction framework to be tested in a setting where the topology is known and is designed to include higher–order structures.

The following system of Rössler oscillators coupled with pairwise and three–body interactions is studied:

$$\begin{aligned}
\dot{x}_i &= -y_i - z_i + \sigma_1 \sum_{j=1}^{N} a_{ij}^{(1)}\, g^{(1)}(x_i, x_j) + \sigma_2 \sum_{j=1}^{N} \sum_{k=j+1}^{N} a_{ijk}^{(2)}\, g^{(2)}(x_i, x_j, x_k), \\
\dot{y}_i &= x_i + a y_i, \\
\dot{z}_i &= b + z_i(x_i - c),
\end{aligned} \tag{3.6}$$

where $g^{(1)}(x_i, x_j) = x_j - x_i$ denotes the linear coupling function for pairwise interactions, and $g^{(2)}(x_i, x_j, x_k) = x_j^2 x_k + x_j x_k^2 - 2x_i^3$ models genuine three–body interactions. The coefficients $a_{ij}^{(1)}$ and $a_{ijk}^{(2)}$ are, respectively, the adjacency matrix of first–order connections and the adjacency tensor of second–order connections. The constants $\sigma_1 > 0$ and $\sigma_2 > 0$ represent the coupling strengths of first– and second–order interactions.

As for the underlying topology of the interactions, namely the components of tensors $A^{(1)}$ and $A^{(2)}$, simplicial complexes, already defined in Section 2.4, are constructed as follows. The starting point is the so–called Zachary karate club, originally described in terms of an undirected graph with $N = 34$ nodes and 78 links. Since the links form 45 triangles, the system can be represented as a simplicial complex by turning a randomly chosen fraction δ of the triangles into two–dimensional simplices. The parameter δ denotes the proportion of triangles that are promoted to genuine 2–simplices, thus representing three–body interactions. By considering different values of δ, the percentage of the nodes forming a triangle which are effectively involved in a three–body interaction rather than in three, separate, pairwise interactions can be tuned. In Fig. 3.1, the results obtained for $\delta = 1$ are reported. Similar results are obtained for other values of δ.

The simplicial complex considered is shown in Fig. 3.1(a). In this case, the components of tensors $A^{(1)}$ and $A^{(2)}$ can either be 0 or 1, as they describe an unweighted structure. The strength of the interactions in Eq. (3.6) is parameterized by the constants $\sigma_1 = 10^{-4}$ and $\sigma_2 = 10^{-5}$.

In spite of the fact that the original structure is undirected, the reconstruction is performed as if the structure were directed. This means that for a given pair of connected nodes i and j both terms $a_{ij}^{(1)}$ and $a_{ji}^{(1)}$ in the adjacency matrix are considered as independent unknowns to be determined.

To quantify the accuracy of the reconstruction of the interactions at any order, the estimation $\hat{\mathbf{a}}_i$ is compared with the true values of the couplings $\mathbf{a}_i$ for each node i, by evaluating the reconstruction error as

$$E^2 = \frac{\sum_{i=1}^{N} \|\mathbf{a}_i - \hat{\mathbf{a}}_i\|_2^2}{\sum_{i=1}^{N} \|\mathbf{a}_i\|_2^2}. \tag{3.7}$$

Analogously, taking into account that in Eq. (3.6) the only non–zero coefficients of $A^{(2)}$ are those with the third index larger than the second one, for a 3–node simplex (i, j, k) with $i < j < k$ there are three independent unknowns $a_{ijk}^{(2)}$, $a_{jik}^{(2)}$, and $a_{kij}^{(2)}$.

To better formalize the reconstruction problem, the mismatch between measurements and model is cast as the minimization of a global error:

$$E = \sum_{i=1}^{N} E_i, \qquad E_i = \left\|\mathbf{y}_i - \mathbf{\Phi}_i \mathbf{a}_i\right\|_2^2. \tag{3.8}$$

In this way, the discrepancies E_i in Eq. (3.8) can be minimized independently, therefore simplifying the reconstruction problem. When M is large enough, so that the error is almost zero, the reconstructed tensors are indeed almost symmetric, i.e., $a_{ij}^{(1)} \approx a_{ji}^{(1)}$ for the first order and $a_{ijk}^{(2)} \approx a_{jik}^{(2)} \approx a_{kij}^{(2)}$ for the second order.

Considering that the interactions to be reconstructed are, in this case, unweighted, the number of different higher–order networks obtainable is finite and equal to 2^{N_H}, where N_H is the number of all possible interactions among the N nodes. An exhaustive search over all possible structures is prohibitive for even moderate values of N. For such a reason, methods for continuous weights are employed, possibly making use of the *a priori* information of the binary nature of the tensors in order to obtain a more effective reconstruction.

Three different methods, already introduced at the beginning of this Section, are adopted to solve Eq. (3.2) when the derivative is exactly known. In the first method, namely OLS, the least–square norm of the difference between $\mathbf{y}_i$ and $\mathbf{\Phi}_i\mathbf{a}_i$ is minimized. The results, indicated by the blue line in Fig. 3.1(b), show that the method correctly reconstructs the simplicial complex when the ratio M/H approaches one. In the second method, namely NNLS, the minimization of the least–square error is performed under the additional constraint that the elements of $\mathbf{a}_i$ are non–negative:

$$\min_{\mathbf{a}_i \geq 0} \|\mathbf{y}_i - \mathbf{\Phi}_i\mathbf{a}_i\|_2.$$

The red curve in Fig. 3.1(b) indicates that, including such *a priori* information on the nature of the interactions in the optimization problem, reduces the values of M/H necessary for the reconstruction. Lastly, SL is extended to deal with higher–order interactions. Namely, the following optimization is considered:

$$\min_{\mathbf{a}_i} \left(\frac{1}{2}\|\mathbf{y}_i - \mathbf{\Phi}_i\mathbf{a}_i\|_2^2 + \alpha\|\mathbf{a}_i\|_1 + \beta\|\mathbf{a}_i - \mathbf{1}_H\|_1 \right),$$

where the penalty function includes, together with the square of the 2–norm of the difference between $\mathbf{y}_i$ and $\mathbf{\Phi}_i\mathbf{a}_i$, a regularization term that induces sparsity of the solution by penalizing the non–zero elements of $\mathbf{a}_i$, and another term to shrink the estimates to one, by penalizing the elements different from one (case of unweighted graph). The effect of the two penalty terms can be easily understood graphically by plotting $\arg\min\{(\hat{x}-x)^2/2+\alpha|x|+\beta|x-1|\}$ as function of $\hat{x}$. As indicated by the orange curve in Fig. 3.1(b), this method provides successful reconstruction with a performance similar to the NNLS (red line). In conclusion, the last two methods are able to fully reconstruct the structure of the simplicial complex, with a smaller sample size than that of OLS.

When the derivatives are not available, a fourth–order approximation is used and, as a first example, $M/H = 34$ is considered. In Fig. 3.1(c), the values of the components of the arrays $\hat{\mathbf{a}}_i$, $i = 1, \ldots, N$ obtained with the OLS (blue dots) and the NNLS (red dots) methods are shown. For the OLS method, the value of M/H is still too low and values of the components of $\hat{\mathbf{a}}_i$ spanning from -3 to 3 are obtained; on the contrary, for the NNLS method the components of $\hat{\mathbf{a}}_i$ are concentrated around the two possible values (0

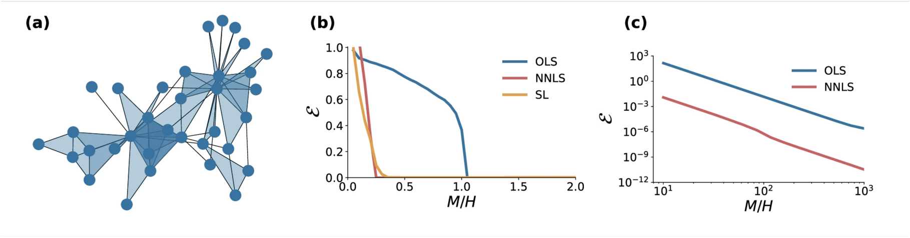

Figure 3.1: **Testing the reconstruction method on a system of $N = 34$ coupled Rössler oscillators.** (a) The underlying simplicial complex consists of 78 links and 45 2–simplices. (b) Reconstruction error E defined in Eq. (3.8) as a function of M/H when derivatives are known. (c) The computed values of the components of the arrays $\hat{\mathbf{a}}_i$, $i = 1, \ldots, N$ for $M/H = 34$ for the OLS method (blue dots) and for the NNLS method (red dots).

and 1), correctly estimating the true values of the coefficients appearing in the tensors $A^{(1)}$ and $A^{(2)}$. The dependence of the error on the ratio M/H is then systematically analyzed.

Overall, this case study confirms that the proposed reconstruction framework is able to recover with high accuracy the complete set of pairwise and higher–order interactions in chaotic oscillator networks, even when the system size is large and the interactions include non–trivial simplicial structures.

3.7 Applications to Lotka–Volterra models of microbial interactions

In the previous sections, the proposed reconstruction framework has been introduced and validated on synthetic datasets and benchmark dynamical systems. The next step consists in applying this methodology to a realistic scenario of biological interest, where the interactions among the system's components are not limited to pairwise terms but also include higher-order contributions. This section considers the case of microbial ecosystems, which provide a natural example of systems exhibiting both cooperative and antagonistic relationships, as well as potential higher-order interactions.

The focus here is on the dynamics of microbial ecosystems. These consist of species that may engage in diverse relationships, either cooperative, such as the transfer of complementary metabolites, or antagonistic, such as competition for a resource[55]. The validation of community-wide interactions in microbial communities is a far from trivial problem, faced both with experimental approaches[102] and through the use of mathematical modeling[15]. The problem is further complicated by potential higher-order interactions, which play a role in stabilizing diverse ecological communities and maintaining species coexistence[52, 3, 95].

Here, a microbial ecosystem of N species is modelled as a hypergraph of coupled Lotka–Volterra type equations, already introduced in Eq. (2.18), which include both pairwise and three-body interactions. The pairwise couplings are collected in the $N \times N$ weighted matrix $A^{(1)} = \{a_{ij}^{(1)}\}$ with at most $N(N-1)$ non-zero elements, while the three-body interactions are encoded in the $N \times N \times N$ weighted tensor $A^{(2)} = \{a_{ijk}^{(2)}\}$ with at most $\binom{N}{2}$ non-zero elements. This reduction follows from the fact that, in Lotka–Volterra type models, the interaction coefficients are invariant under permutations of the indices, so the number of independent entries of tensor $A^{(d)}$ is $\binom{N}{d}$.

Equation (2.18) can therefore be regarded as a specific instance of the general hypernetwork formulation introduced in Eq. (2.11), with $g^{(1)}(x_i, x_j) = x_i x_j$ and $g^{(2)}(x_i, x_j, x_k) = x_i x_j x_k$.

As an example, the system of $N = 7$ species with four cooperative ($a_{ij}^{(1)} > 0$) and four antagonistic ($a_{ij}^{(1)} < 0$) pairwise interactions, studied in [15] and shown in Fig. 3.2(a) with blue and red arrows, respectively, is considered. In addition to these pairwise interactions, two cooperative three-species interactions are included, shown as double arrows in the hypergraph in Fig. 3.2(a). These correspond, respectively, to a contribution to the dynamics of x_2 given by $a_{237}^{(2)} x_2 x_3 x_7$ and one to x_4 given by $a_{416}^{(2)} x_4 x_1 x_6$, with $a_{237}^{(2)} = 0.0062$ and $a_{416}^{(2)} = 0.00161$. The other system parameters, i.e., the values of r_i, k_i, $i = 1, \ldots, 7$, and the initial conditions have been chosen as in [102]. Namely, growth rates r_i for all species have been randomly selected from a uniform distribution in the interval $(0, 1)$, similarly, the carrying capacities k_i are sampled from a uniform distribution in the interval $(1, 100)$, and the initial conditions $x_i(0)$ are integers sampled in the interval $(10, 100)$.

Under these conditions, as shown by the time evolution of the variables $x_i(t)$, with $i = 1, \ldots, 7$, reported in Fig. 3.2(b), the microbial ecosystem typically converges to a stable equilibrium point corresponding to the coexistence of six species over seven. To feed the reconstruction algorithm described at the beginning of this Capther, the time window $[0, t_{\max}]$ with $t_{\max} = 20$ is considered, and the seven trajectories are sampled at M regular intervals of size $\Delta t = t_{\max}/M$. The samples are then used to calculate $\mathbf{y}_i$ and $\mathbf{\Phi}_i$ from Eq. (3.2). At this point, the ordinary least squares (OLS) method based on the complete orthogonal decomposition (see [51]) is adopted, which provides the optimal solution of minimal discrepancy E between the measurements $\mathbf{y}_i$ and the corresponding values produced by the system $\mathbf{\Phi}_i \mathbf{a}_i$,

$$E = \sum_{i=1}^{N} E_i, \quad E_i = \|\mathbf{y}_i - \mathbf{\Phi}_i \mathbf{a}_i\|_2^2. \tag{3.9}$$

The total number of parameters is NH, while the total number of sampled values is nNM (in this case $n = 1$). The minimum of the sum is obtained by minimizing each term E_i separately. The complete orthogonal decomposition provides the solution of minimal ℓ_2 norm when there is more than one minimizer.

To quantify the accuracy of the reconstruction of the interactions at any order, the estimation $\hat{\mathbf{a}}_i$ is compared with the true values of the couplings $\mathbf{a}_i$, for each i, evaluating the reconstruction error E as:

$$E^2 = \frac{\sum_{i=1}^{N} \|\mathbf{a}_i - \hat{\mathbf{a}}_i\|_2^2}{\sum_{i=1}^{N} \|\mathbf{a}_i\|_2^2}. \tag{3.10}$$

Figure 3.2(c) shows E as a function of M/H, under the assumption that the derivatives are available. Different values of M/H have been obtained by changing the number of measurements M, while the number of unknown coefficients to be determined is $H = N-1+(N-1)(N-2)/2 = 21$, where the factor 2 in the denominator is due to the symmetry of the interaction terms in Eq. (2.18), which reduces the number of unknowns and consequently the computational cost. The results indicate that the approach correctly reconstructs both pairwise and three-body interactions of the hypergraph, as the error drops when $M/H \approx 1.8$.

The feasibility of this approach has been demonstrated, with results and performance analyzes, including the impact of numerical approximations, discussed in detail in [71].

In conclusion, this case study demonstrates the applicability of the reconstruction framework to systems with higher-order interactions, providing

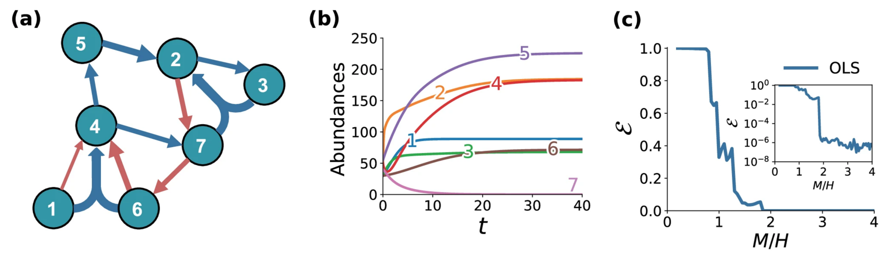

Figure 3.2: **Reconstructing higher-order interactions in a microbial ecosystem.** (a) The underlying weighted hypergraph of a Lotka–Volterra system with $N = 7$ species and two- and three-body interactions, which we want to reconstruct from (b) the time evolution of the seven species abundance $x_i(t)$. (c) Quality of the reconstruction is measured by reporting the error ϵ as a function of the ratio between the length M of the trajectories and the number H of interactions to reconstruct.

accurate recovery of both pairwise and three-body couplings under realistic sampling and noise conditions. The results confirm that, when the sampling rate and data quality are adequate, the proposed methodology can serve as a reliable tool for disentangling complex ecological interaction structures.

3.8 Applications to power–grid networks with swing dynamics

In the previous sections, a reconstruction framework has been developed that exploits known node dynamics and local linear inverse problems to infer active connectivity under structural perturbations. Here, attention is restricted to power systems modeled by swing equations (Eq. (2.16)), a canonical setting for flow/transport networks where line tripping can induce cascading failures. The goal is to demonstrate, using the same protocol introduced above (Subsection 3.5), how active links can be identified from sampled phase angles and angular velocities during a cascade, and how reconstruction accuracy depends on the sampling window and noise level.

A high-voltage (380 kV) power grid (Fig. 3.3) is considered. This power system consists of $N = 127$ nodes (34 generators and 93 loads), and $L = 171$ links. The parameters of the swing equations (Eq. (2.16)) are selected as

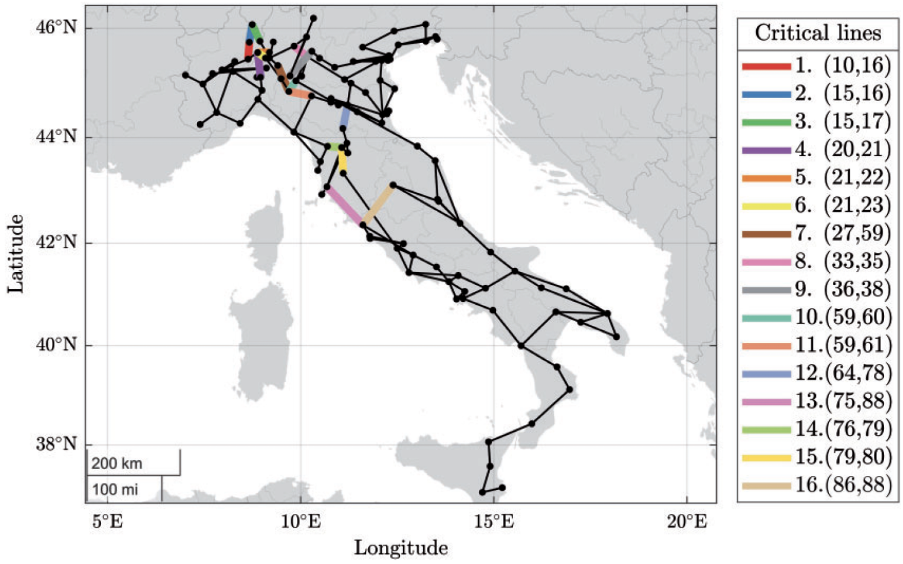

Figure 3.3: Topology of the Italian high–voltage (380 kV) power grid. Critical lines, namely the lines whose failure, due to an exogenous event, triggers a cascade of other faults, are highlighted in different colors (see also Table 1). For an interactive version of the map see [28].

in [30], namely $I_i = 1$, $\gamma = 0.1$, $\alpha = 0.6$ and $\kappa = 15$. Furthermore, the power for the load nodes is set to $P_i = -1$, while for the generator nodes $P_i = 2.7353$, so that the network is balanced, that is, $\sum_{i=1}^{N} P_i = 0$. With this setting of the parameters, the power grid is synchronized in the absence of faults [30].

To study cascading failures in this power grid, the swing equation model (Eq. (2.16)) is numerically simulated starting from the failure of a line $(i^\star, j^\star)$ at time $t = t_f$, following the temporal evolution of the flows in the network, and repeating the simulation for each possible initial location $(i^\star, j^\star)$ of the fault. The results of the simulations indicate that cascading failures are triggered for 16 of the 171 lines. For each of these cases, Table 3.1 illustrates the location of the initial fault and the sequence of failures in the other lines. The length of the cascading failures ranges from a minimum of 1 line to a maximum of 12 lines. The local reconstruction network algorithm discussed in Section 3.5 has been applied to each of these cascading failures by varying the key parameters of the algorithm such as the length of the time window

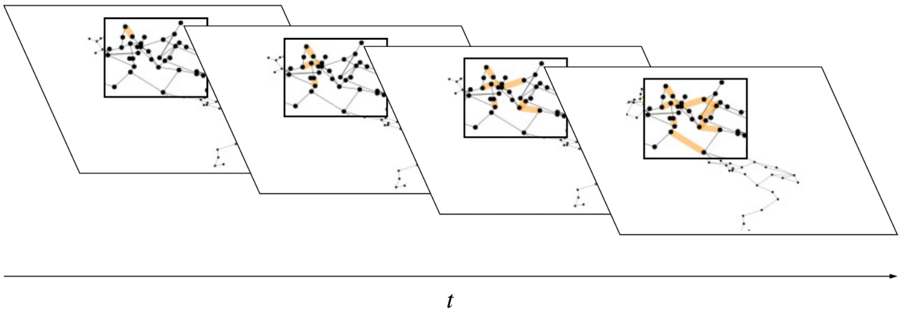

Figure 3.4: Snapshots of the topology of the Italian high–voltage power grid illustrating the propagation of the fault of line $(15, 17)$. In the first temporal slice, the initial fault $(15, 17)$ is highlighted with a bold line, while the other panels highlight the lines failing in successive steps. They are: lines $(10, 21)$, $(11, 20)$ and $(21, 22)$ in the second temporal slice; lines (59,61), $(59, 60)$ and $(28, 30)$ fail in the third; and lines $(33, 35)$, $(12, 14)$ and $(36, 38)$ in the fourth.

of the measurements, namely $W = t_{\text{end}} - t_{\text{start}} = M\,\Delta t$, and the level of noise in the data, as defined below.

An example of reconstruction of one of the cascading failures is first discussed, more specifically that induced by an initial fault in the line $(i^\star, j^\star) = (15, 17)$ at $t_f = 1.5$ s (Fig. 3.4). The temporal evolution of the flows $F_{ij}(t)$, obtained under these conditions, is shown in Fig. 3.5(a), where, in particular, only the flows associated with lines subject to failures are reported. As it can be noticed, the initial fault propagates in the power grid as the flows are dynamically redistributed. During the system evolution, several flows at some time overcome the maximum capacity, thus triggering the protection mechanism that shuts down the line. Correspondingly, these flows go to zero and induce a further redistribution of other flows in the network. The last three failures in the cascade occur at times close to each other, between 5.00 and 5.02 s (Fig. 3.5(a). A qualitatively similar trend is found for the other 15 lines reported in Table 3.1.

Figure 3.5(b) shows the results of the application of the method to infer the temporal sequence of the cascading lines. In particular, the measurements used as input for the algorithm are obtained sampling the voltage phase angle $\theta_i(t)$ and the angular velocity $\omega_i(t)$ $(i = 1, \dots, N)$ at regular time intervals of length $\Delta t = 0.001$ s. Algorithm 1 is iteratively applied at

Table 3.1: Cascading failures in a model of the Italian high-voltage power grid. The line where the initial fault is located, the length of the cascade and the ordered temporal sequence of the lines involved in the cascading failures are reported.

Line	Cascade length	Temporal sequence of failed lines
1.(10,16)	5	(21,22), (27,59), (28,30), (33,35), (30,31)
2.(15,16)	6	(21,22), (27,59), (28,30), (33,35), (30,31), (36,38)
3.(15,17)	9	(10,21), (11,20), (21,22), (59,61), (59,60), (28,30), (33,35), (12,14), (36,38)
4.(20,21)	9	(7,10), (59,61), (59,60), (28,30), (33,35), (36,38), (30,31), (12,14), (61,62)
5.(21,22)	8	(27,59), (15,17), (33,35), (36,38), (18,24), (21,23),(34,38), (12,14)
6.(21,23)	6	(59,61), (59,60), (21,22), (27,59), (36,38), (10,16)
7.(27,59)	5	(21,22), (15,17), (28,30), (33,35), (36,38)
8.(33,35)	12	(36,38), (27,59), (34,38), (21,22), (30,31), (15,17), (22,24), (18,24), (12,14), (24,26), (21,23), (58,59)
9.(36,38)	5	(33,35), (27,59), (30,31), (21,22), (15,17)
10.(59,60)	7	(59,61), (21,23), (21,22), (27,59), (15,16), (28,30), (12,14)
11.(59,61)	6	(7,10), (11,20), (59,60), (28,30), (36,38), (33,35)
12.(64,78)	3	(71,83), (14,61), (86,88)
13.(75,88)	3	(71,83), (79,80), (86,88)
14.(76,79)	2	(78,81), (71,83)
15.(79,80)	2	(75,88), (71,83)
16.(86,88)	1	(71,83)

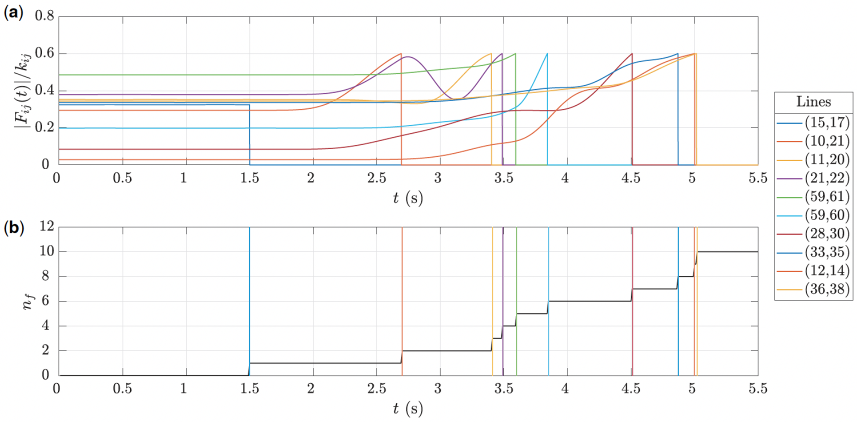

Figure 3.5: Cascading failures and their reconstruction in the Italian high-voltage power grid. (a) Temporal evolution of the flows of the links (i, j) in the cascade triggered by the initial fault of the line $(15, 17)$. (b) Reconstruction of the number of failed lines, n_f, as obtained from the local network reconstruction algorithm introduced in this chapter.

each time h_M, by calculating for each node i a number M of samples $r_i(h)$ (with $h = h_1, \ldots, h_M$), and evaluating the corresponding local regression matrices $\mathbf{\Phi}_i'$ for $i = 1, \ldots, N$ (see the active-link linear systems described below Algorithm 1). In the example shown in Fig. 3.5, the smallest temporal distance between two failure events is 0.02 s (the line $(12, 14)$ fails at time 5.00 s, and the line $(36, 38)$ at time 5.02 s). Therefore, in order to be able to identify them one-by-one, the temporal resolution of the network local reconstruction algorithm, that is given by the product of the window length M and the sampling Δt, has to be smaller than 0.02. At the same time, M has to be greater than the maximum node degree in order for the local linear systems to be overdetermined. As the maximum node degree in the Italian high-voltage power grid is 7, selecting $M = 10$ fulfils both requirements. This corresponds to have $W = M\,\Delta t = 0.01$ s. The comparison between the number of failed lines, n_f (Fig. 3.5(b), calculated counting at each time t how many lines are classified as failed by Algorithm 1, and the temporal evolution of the flows (Fig. 3.5(a) shows that the 10 failure events occurred in the cascading failure under exam are correctly inferred.

Next, the performance of the reconstruction method is studied in presence of noise in the data. To this aim, the algorithm is now fed with noisy samples of the phase variables, that is, $\tilde{\theta}_i(h) = \theta_i(h) + \sigma\,\xi(h)$, where $\theta_i(h)$ are the values obtained from the integration of Eq. (2.16), $\xi(h)$ are random variables drawn from a zero mean Gaussian distribution with unitary variance, and σ represents the standard deviation of the additive noise, here considered as a representative parameter for the noise level. The parameter σ is varied from 10^{-15} to 10^{-2} and the impact of noise is evaluated by measuring the error between the original and the reconstructed topology. In more detail, let A^* indicate the adjacency matrix of the reconstructed network. As a measure of the difference between the reconstructed network and the real one, the following reconstruction error is calculated:

$$E_r = \frac{\|A^* - A\|_2^2}{N(N-1)}\,, \tag{3.11}$$

where $\|\cdot\|_2$ indicates the matrix 2-norm.

Figure 3.6 shows the results obtained in the case of an initial fault in $(15, 17)$, and for different values of the time window W: 0.01, 0.05, 0.1 and 0.5 s. The reconstruction error E_r is evaluated once all the failures in the cascade have occurred. As expected, it is found that the error E_r increases with noise. For larger values of the time window W, the error is smaller, indicating that larger sets of data can be used to decrease the impact of the noise on network reconstruction.

Finally, the results of the systematic analysis of each of the critical lines listed in Table 3.1 are illustrated. In this case, for each line, the reconstruction error E_r has been evaluated in the absence of noise and for two different values of the noise ($\sigma = 10^{-8}$ and $\sigma = 10^{-5}$). Two values for the time window W have been also considered ($W = 0.01$ s and $W = 0.03$ s). The prediction error is shown in Fig. 3.7 with respect to different initial fault locations, labeled as in Table 3.1. The final topology, as well as the correct sequence of failed lines, is perfectly reconstructed in the absence of noise, for each critical line and value of W (circle symbols). A non-zero error is, instead, found for noisy data (square and triangle symbols), with larger errors occurring for larger noise. Also in this case, using a larger temporal window consistently reduces the error for each initial fault location.

In flow and transport networks, the dynamical evolution of the state variables may lead to the failure or intentional shut down of one or more

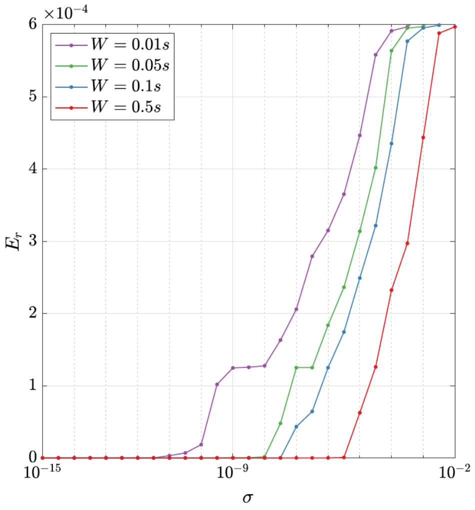

Figure 3.6: Reconstruction error E_r vs. standard deviation of the noise, σ, for different values of the time window of measurements, W. The cascading failure is that shown in Fig. 3.5 and triggered by a fault located in the line $(15, 17)$ at $t_f = 1.5$ s. The reconstruction error E_r is always evaluated at the end of the cascading failure, fixing $t_{\text{start}} = 5.02$ s and $t_{\text{end}} = t_{\text{start}} + W$.

links. Understanding the status of these links is fundamental for timely interventions on the network and to prevent the propagation of the failure in large portions of the system. In this section, the problem of inferring the active links in networks of this type has been considered, by focusing on a specific case study, that is, power grids. An approach has been proposed based on the knowledge of the underlying model of network dynamics. Such information is then combined to direct measurements of the node angles and angular speeds and leads to a set of systems of algebraic equations to solve in order to find the active links of the network. Furthermore, it has been shown that incorporating the available information on the topology of the power grid reduces the size of the problem and facilitates its solution. Even if, to illustrate the method, the application to a specific mathematical model of the power grid has been discussed, where each node dynamics is described by a swing equation, this assumption is not crucial and alternative models of the power system can be similarly adopted. Although not constrained to a specific mathematical form, the model of the local dynamics and the interaction functions, however, need to be known and, therefore, they have

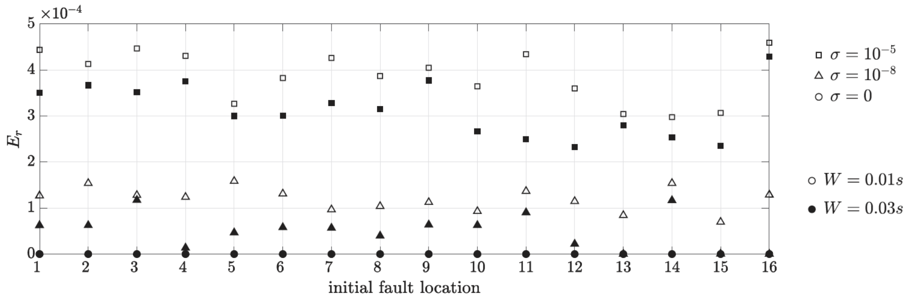

Figure 3.7: Reconstruction error E_r for the topology obtained after a cascading failure started at each of the critical lines of the Italian high–voltage power grid, for different values of the time window of measurements, W, and of the noise standard deviation, σ: circle symbols refer to noise-free data; triangle symbols to noisy data with $\sigma = 10^{-8}$; square symbols to noisy data with $\sigma = 10^{-5}$; empty (filled) symbols refer to $W = 0.01$ s ($W = 0.03$ s).

eventually to be identified, prior to the application of the method presented in this work.

As a concrete example, an application of the approach to cascading failures in a mathematical model of the Italian high-voltage power grid has been shown. However, the results should not be interpreted as quantitative predictions of the real power system, as this would require a more detailed model of generator machines, load and line characteristics, and protection mechanisms. On the contrary, the results highlight a technique tunable to the features of the power grid, the sampling frequency of the data, and the statistical and spectral properties of the noise.

The local, model-informed inverse formulation enables accurate, time-resolved identification of active links during cascades from short windows of (θ, ω) measurements, provided the sampling resolution resolves the inter-failure intervals and M exceeds the maximum degree. Larger windows mitigate noise, and known backbone constraints reduce ambiguity.

Chapter 4

Generative models

Many heterogeneous real-world systems can be modeled as spatial networks, where nodes and edges are embedded in space [21]. Despite the importance of spatial factors, many generative models for complex networks [19, 64, 17] do not explicitly account for them. Instead, they focus on topological features, often overlooking the impact of spatial embedding on network structure and dynamics. For instance, classical generative network models such as the Erdős–Rényi model [84], the Watts–Strogatz model [106], and the Barabási–Albert model [11], generate networks through random processes that replicate certain characteristics of real-world networks, but they do not consider the spatial embedding of nodes. Specifically, the Erdős-Rényi model generates networks with a given number of vertices and edges, which are randomly distributed, and, in this way, captures the small average distance between nodes, a characteristic often observed in social networks. The Watts–Strogatz model, in contrast, generates random graphs [32] that display the small-world property, often seen in real-world networks where efficient information flow coexists with a strong tendency of nodes to form closed triangles. Lastly, the Barabási–Albert model produces random networks with a degree distribution following a power law, replicating the emergence of nodes with exceptionally high connectivity (the hubs), frequently observed in various real-world systems like transportation networks.

Spatial features of nodes are explicitly incorporated in several classes of generative network models. Remarkable examples include geometric graphs, spatial generalizations of Erdős–Rényi graphs, spatial small-world models, spatial growth models, and networks optimized according to spatial criteria [12]. In geometric graphs, a direct geometric rule governs link formation: nodes are embedded in a metric space, and an edge is created between two nodes if their Euclidean distance falls below a predefined threshold, commonly referred to as the neighborhood radius [60]. Spatial generalizations of the Erdős–Rényi model, by contrast, modify the connection probability between any pair of nodes to depend explicitly on the spatial distance, typically via a decaying function such as an exponential law. The third class comprises spatial small-world models, which are constructed beginning with a regular lattice of locally connected nodes and then adding long-range links with a probability that decreases with the spatial distance between nodes, thereby preserving local structure while introducing shortcuts that reduce the average path length. The fourth group includes spatial growth models, in which the network evolves over time through the sequential addition of new nodes that establish links to existing nodes based on spatial proximity rules. The last group includes networks generated by minimizing some cost functions that balance spatial constraints, such as wiring length, with functional objectives, such as communication efficiency.

The models mentioned above are abstract in nature; they do not originate from the analysis of a specific spatial network, but rather aim to reproduce general features commonly observed in such systems. For instance, they typically do not preserve the empirical degree distribution, which, on the contrary, is a distinctive feature of the method proposed in this thesis. Specifically, a new generative model for spatial networks is proposed and applied to two distinct case studies: power grids, as an example of a two-dimensional spatial network, and brain networks, as a three-dimensional example. These real-world networks exhibit distinct characteristics that require the development of dedicated models. Crucial factors are, for instance, wiring cost minimization in both power grids and brain networks, and processing paths in brain networks. The main characteristics of the model and the contribution of this work with respect to the state of art will be discussed after illustrating the specific motivations for the two considered case studies.

4.1 Motivation and objectives

The proposed model produces new synthetic spatial networks through an iterative process that starts from a set of disconnected nodes and then assigns the links taking into account the spatial features of the node configuration. Specifically, the model is characterized by two factors, namely node positions and degree distribution. In the proposed model a general approach is pursued, with nodes that can be placed either in a two-dimensional or three-dimensional space. The node positions can be unconstrained, or, if the aim of the model is to produce surrogate networks from a sample of real-world structures, selected by mocking up the spatial features of the real-world structures at different levels of approximation. For instance, node positions can be selected to fit the spatial outline of the real-world network, or to preserve the node spatial density, or to closely reproduce the positions in the original structure. Once node positions are determined, the links between nodes are assigned to fit a target degree distribution. This distribution can, eventually, stem from the distribution that empirically characterizes a dataset of real-world structures.

Compared to the classical spatial network models discussed in [12], therefore, the key distinguishing feature of the model is that it is grounded in empirical data. However, unlike AI-based approaches, it does not rely entirely on data-driven fitting but instead builds on explicit, interpretable generative mechanisms. In this sense, the model lies at an intermediate position between fully mechanistic models and data-driven black-box approaches, combining interpretability with adaptability. This makes it particularly well suited for generating realistic surrogate spatial networks in scenarios where real data are scarce, while maintaining control over both topological and spatial characteristics.

The application of the model is exemplified with two different case studies: an example of technological, two-dimensional networks, namely power grids, and an example of biological, three-dimensional networks, such as brain networks. These two examples, pertaining to different fields, highlight the broad applicability of the model across diverse domains, from human-made infrastructures to biological systems. The novelty of the proposed model is now briefly discussed in relation to these two fields of application.

Current research on generative models for power grids has focused on replicating the structural and topological characteristics of real-world electricity networks, with an emphasis on balancing cost efficiency and network redundancy. A notable model specifically designed to capture key features of power grids is proposed by Schultz et al. [92]. This model follows a three-step process. It begins with an initialization phase that generates a minimal spanning tree, ensuring cost-effective network connectivity. This step is followed by a growth phase, where additional links are introduced, first by connecting existing nodes and then by adding new nodes according to a preferential attachment rule. Finally, in an evolution phase, certain edges are divided in two by inserting new nodes between their original endpoints, thus increasing redundancy in the network structure. Building on this body of work, the proposed model employs a distinct approach based on a two-step process. In the first step, the number of nodes and their positions are assigned, as introduced above, while, in the second step, links are selected mocking-up the target distribution and using an attachment law governing the creation of edges between nodes on the basis of their spatial distance.

For what concerns the generative models that have been developed for brain networks, previous models mainly incorporate the notion of wiring costs, that provide spatial physical constraints for the network links, and metabolic costs, which represent the cost required to establish long-range connections and therefore have to be minimized. Another aspect that these models take into account is that brain networks exhibit high topological segregation, characterized by modular structures where groups of nodes are densely connected within modules that have sparse connections with other modules [78]. These foundational aspects are also included in the dependence of the attachment law on the spatial distance of nodes.

In the literature of brain networks, the random surrogate method [22] is widely employed, particularly for null-hypothesis testing aimed at highlighting target properties of real-world networks. However, this method has limitations in replicating key features of brain networks, mainly because its long-range connections do not result in the high topological segregation typical of the brain. On the other hand, the lattice surrogate approach, which is another method commonly used to generate brain surrogate networks, typically produces structures topologically characterized by an over-segregation, but, being highly grounded on spatial constraints, with low efficiency in the communication between far regions. Nonetheless, these surrogate networks are only partially suitable for brain network modeling, as they do not account for the crucial role of wiring costs. To overcome this limitation, the authors of [87] proposed two new types of surrogates: spatial surrogates and reduced surrogates. These approaches preserve key spatial and topological properties of the original brain network, including the number of nodes (size), the number of edges (connection density), and the degree distribution (the number of connections per node). The key difference between them lies in how they treat wiring: spatial surrogates preserve the total wiring length of the brain network, while reduced surrogates use lowered wiring costs.

Here, a different approach is proposed for generating networks that replicate the spatial characteristics of real-world brain networks. Specifically, the costs involved in constructing synthetic brain networks, which reflect real-world features, are taken into account in the following way. On one hand, wiring costs are addressed by expanding the principle of physical constraints and introducing four distinct rules for placing synthetic nodes at various spatial scales. On the other hand, metabolic costs are considered by implementing attachment laws that are spatially dependent, gradually decreasing the likelihood of connecting nodes as the physical distance between them grows.

4.2 Generative modeling framework

In the proposed model, the spatial network is constructed by starting with a set of uncoupled nodes and iteratively assigning edges, node by node. Specifically, the nodes, labeled as $1, 2, \ldots, N$, are initially assigned a position $\mathbf{x}_i$ in a metric space $X \subset \mathbb{R}^d$, where the spatial network resides, and a predetermined degree $\bar{k}_i$. The network, which is undirected and unweighted, is constructed in an iterative way. At each iteration t of the growth process, a node i is selected and a number of links equal to $\bar{k}_i - k_i^{t-1}$ is added to the set of already existing edges, where k_i^{t-1} is the degree of node i at iteration $t-1$. More precisely, at each iteration the node i is selected with a probability Π_i directly proportional to $\bar{k}_i - k_i^{t-1}$:

$$\Pi_i = \frac{\bar{k}_i - k_i^{t-1}}{\sum\limits_{m=1}^{N} (\bar{k}_m - k_m^{t-1})} \tag{4.1}$$

In this way, the node to be processed at each iteration is selected according to a probability distribution proportional to its remaining number of links. This preferential mechanism ensures that nodes with higher target degrees are more likely to be processed early in the growth process, when many other nodes have not yet reached their assigned degree and are thus still available as potential neighbors. In sparse networks, this strategy significantly increases the likelihood of matching the desired degree distribution, reducing the risk of encountering situations in which it becomes impossible to assign a high degree to a node because of the lack of eligible neighbors.

For each of the $\bar{k}_i - k_i^{t-1}$ links added at step t, the other endpoint of the edge, labeled as node j, is also selected randomly, with a probability that depends on the spatial distance between the nodes i and j, that is, $\Pi_j = \Pi_j(s_{ij})$, where s_{ij} measures the distance between the positions of i and j. To set the framework, the analysis is restricted to the cases of $d = 2$ and $d = 3$ (two-dimensional and three-dimensional space, respectively) and considers two different laws for $\Pi_j = \Pi_j(s_{ij})$. The first reads

$$\Pi_j^1(s_{ij}) = \frac{s_{ij}^{-\alpha}}{\sum\limits_{m=1}^{N} s_{im}^{-\alpha}} \tag{4.2}$$

with s_{ij} being the Euclidean distance between $\mathbf{x}_i$ and $\mathbf{x}_j$ in $\mathbb{R}^d$. Here, $\alpha > 0$ is a parameter that allows tuning the weight of the distance in the expression of $\Pi_j^1(s_{ij})$: the higher the value of α, the less likely it is to connect two distant nodes.

Given that spatial proximity is a fundamental feature of real-world networks, postulating that the probability of connectivity depends on the inverse of the node distance through a generalized tunable exponent α is a natural assumption. However, to avoid limiting the analysis to this specific formulation and to accommodate networks where the relationship between edge length and connection probability may follow a different, possibly system-specific pattern, a second, data-driven attachment law is also introduced, described in detail below. This second law is expressed as follows:

$$\Pi_j^2 = \frac{\Pi_s^R(s_{ij})}{\sum\limits_{m=1}^{N} \Pi_s^R(s_{im})} \tag{4.3}$$

where $\Pi_s^R(s)$ is an assigned probability distribution for the node distances s, obtained by fitting the data of the real-world network. In this second case, the aim is not only to fit the set of desired degrees $\bar{k}_i$ $(i = 1, \dots, N)$ but also the probability distribution $\Pi_s^R(s)$ derived from real data, a step that may be relevant in some applications. In both cases, when setting the network edges, self-loops and multiple links are avoided by setting to zero the probability of selecting as node j the node i itself, a node that is already linked to i, or a node that has already reached its desired degree.

It is worth noticing that, while the first attachment law favors the creation of short-distance links by assigning higher connection probabilities to spatially close nodes, the second attachment law allows the probability of connecting two nodes to follow the empirical distribution of edge distances observed in a real network. In this way, the generative model can be adapted to replicate different types of spatial connection patterns, depending on the research goals or the empirical system under study. Recent evidence [114], showing that neuronal connection probability decreases according to a power-law function of spatial distance, provides a direct empirical support for the distance-decay formulation adopted in Eq. (4.2).

The iterative procedure underlying the growth process of the proposed model is repeated until $\sum\limits_{i=1}^{N}(\bar{k}_i - k_i^t) \leq 2$; at this point, if possible, two remaining nodes whose degrees at iteration t have not yet reached the target are connected. Finally, the connectedness of the network at the final step is checked. If the network consists of two or more disconnected components, further links are added between these components, with a higher probability of connecting nodes that are closer in Euclidean distance. Since the model generates undirected networks, it requires that the sum $\sum\limits_{i=1}^{N} \bar{k}_i$ is even [10].

Concerning node positioning, several options are considered. In the first scenario, no physical constraints are imposed on the node positions, and the nodes are placed within a normalized area/space. In the second scenario, developed to generate surrogate networks, physical constraints of varying strictness are applied. These constraints provide progressively finer representations of the area/space where the original network is defined.

The first constraint bounds only the minimum and maximum values of each component of $\mathbf{x}_i$, effectively placing the nodes within a rectangular box that encompasses all the node positions of the original network. The nodes of the surrogate networks are placed within this space at positions randomly selected according to a uniform distribution. The second constraint provides a stricter bound for the node positions. In this case, a rectangular box that encompasses all the node positions of the original network is divided into a grid of $p \times p$ cells for $d = 2$, or $p \times p \times p$ cells for $d = 3$. Then, the cells containing a non-zero number of nodes are shuffled, and, within each cell, the node positions are randomized while preserving the original number of nodes in the cell. In the third scenario, the same grid partition is considered, but, in this case, only the node positions within each cell are randomized, without shuffling the cells themselves. Consequently, each cell in the synthetic network contains the same number of nodes as the corresponding cell in the original network. Finally, in the fourth case, the nodes are constrained to their original positions and the model is applied to assign the edges from scratch.

Four constraints are defined to provide a set of possible options to select based on the application and the specific goals of the model. Constraint 1 represents the most generic case, with a uniform random placement of the nodes, while Constraint 4 replicates the exact spatial layout of the original configuration of the units. Constraints 2 and 3 serve as intermediate options, preserving boundary shape or spatial density, respectively. The choice of the constraint to use depends on the application context, the available data, and ultimately the goal of the generative models. Different constraints can be adopted, for instance, to test how the node positions and their density impact on the behavior of the system associated with the network, while in other cases it may be necessary to investigate the effect of link reshuffling without varying the positions of the nodes. When the proposed model is used to generate surrogate networks, varying the constraint allows for the exploration of alternative hypotheses on spatial embedding and the assessment of their effects on structural features and network-driven processes.

The key steps for applying the proposed model to generate a spatial network from real data are illustrated in Fig. 4.1. First, the analysis of a real network (or a set of networks), such as a power grid or a brain connectome, is performed to derive its degree distribution. From this distribution, a set of N values representing the target degrees for the synthetic network with N nodes is extracted, denoted as $\bar{k}_1, \ldots, \bar{k}_N$. Note that N does not need to match the number of nodes in the original network unless surrogate networks are generated, in which case N is exactly the same as in the original network. Afterwards, the node positions $\mathbf{x}_i$ $(i = 1, \ldots, N)$ are assigned according to what has been previously discussed. Finally, the edges of the network are set, node by node, adding links between two nodes i and j, with node i being chosen with probability Π_i as in (4.1) and node j with probability Π_j as in (4.2) or (4.3).

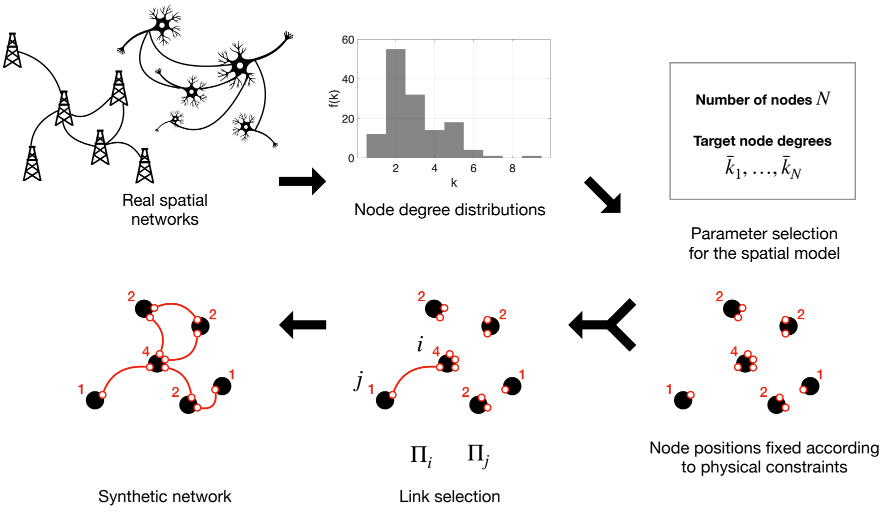

Figure 4.1: Overview of the use of the proposed model to generate spatial networks with node degrees extracted from real data. From real data on spatial networks, the node degree distribution is obtained. In turn, this is used to generate the target values of the node degrees, namely $\bar{k}_1, \ldots, \bar{k}_N$. Node positions are then fixed either without specific constraints or using physical constraints of different strictness. Lastly, edges are added by randomly choosing both endpoints of each link, while satisfying the desired node degrees (see text for the description of the attachment laws used).

An algorithm for the proposed model is reported in Algorithm 2. The input of the algorithm is the set of desired values for the node degrees, namely $\bar{k}_1, \ldots, \bar{k}_N$, and, in the case where a physical constraint is also applied to the node positions, the positions of the nodes in the original network (such points are denoted as $\mathbf{x}_i^{\text{data}}$ for $i = 1, \dots, N$). The output of the algorithm is the spatial network, comprising the node positions $\mathbf{x}_i$ $i = 1, \dots, N$, and the edges set by the model. The first phase involves node positioning. If no constraints are applied, the nodes are placed at points randomly selected according to a uniform distribution within a normalized space. If physical constraints are applied, a bounding box that encompasses all points of the original network is first defined. From this box, the different physical constraints can be imposed to regulate the placement of the nodes within the space (see the first switch condition). Notice that in case of the fourth constraint $\mathbf{x}_i = \mathbf{x}_i^{\text{data}}$ for $i = 1, \dots, N$.

Once the node positions are selected, the algorithm moves to the second step of network construction (see the second switch condition). This step involves assigning the edges iteratively, considering the nodes one by one. Given the target values, namely $\bar{k}_1, \dots, \bar{k}_N$, which can be obtained, for instance, by sampling N values from the degree distribution of a real network (or of a set of networks), and their actual values at the previous iteration, namely $k_1^{t-1}, \dots, k_N^{t-1}$, the algorithm proceeds using Eq. (4.1) to determine the node i to consider at the iteration t. Next, the other endpoint of the link to add is selected, using Eq. (4.2) or Eq. (4.3) to compute the probability of selecting another node that is not already connected to i and has not yet reached its target degree.

4.3 Applications to power grids

Power grids serve as a classic example of man-made complex networks.

Network-based models of power grids are particularly valuable for investigating the dynamical behaviors that arise under both normal operating conditions, such as synchronization, and in the presence of faults, like cascading failures. The latter is especially critical, as cascading failures can lead to large-scale blackouts.

The problem of cascading failures in power transmission systems has already been introduced in Chapter 3, where it was analyzed within the framework of swing–equation dynamics. In the present chapter, the perspective is different: instead of addressing the reconstruction of active links during a cascade, the focus is on the development of a generative model

Algorithm 2: Generative model of spatial networks

```
Input: $\bar{k}_1, \dots, \bar{k}_N$; $\mathbf{x}_1^{\text{data}}, \dots, \mathbf{x}_N^{\text{data}}$
Output: $\mathbf{A}$, $\mathbf{x}_1, \dots, \mathbf{x}_N$
switch Topological constraint do
    case No constraint do
        Assign random values for $\mathbf{x}_i$ in $[0,1]^d$
    end
    case Constraint 1 do
        $\mathbf{x}_i \sim \mathcal{U}(\ \min(\mathrm{x_{i,j}}),\ \max(\mathrm{x_{i,j}}))$
        $\forall i = 1, \dots, N,\ j = 1, \dots d$
    end
    case Constraint 2 do
        divide into $(p \times p)$ or $(p \times p \times p)$ cells
        randomize cells
    end
    case Constraint 3 do
        divide into $(p \times p)$ or $(p \times p \times p)$ cells
        randomize $\mathbf{x}_i$ inside each cell
    end
    case Constraint 4 do
        $\mathbf{x}_i = \mathbf{x}_i^{\text{data}},\ \forall i = 1, \dots N$;
    end
end
compute the distances $s_{ij}$
while $\sum_{i=1}^{N} (\bar{k}_i - k_i^{t-1}) > 2$ do
    switch Attachment law do
        Select node $i$ with probability $\Pi_i$ according to Eq. (4.1)
        case Law 1 do
            Node $j$ is selected with probability $\Pi_j^1$ as in Eq. (4.2)
        end
        case Law 2 do
            Node $j$ is selected with probability $\Pi_j^2$ as in Eq. (4.3)
        end
    end
    set $\mathbf{A}_{ij} = 1$, $\mathbf{A}_{ji} = 1$
    compute $k_i^t$
    t=t+1
end
```

capable of producing synthetic power grids that reproduce both the spatial embedding and the topological characteristics of real infrastructures. This allows us to investigate how structural and geometric constraints shape network vulnerability, and to generate surrogate networks that can be used when real data are scarce or incomplete.

4.3.1 Reference real-world data

The proposed generative model is applied to synthesize networks that replicate key structural features of power grids. The UCTE (Union for the Coordination of Transmission of Electricity) European transmission network is considered, consisting of 1254 nodes (of which 378 are generators and 876 loads) and 1812 links [116, 70, 47]. The grid encompasses 18 continental European countries: Portugal (P), Spain (E), France (F), Belgium (B), Luxembourg (LU), Switzerland (CH), Italy (I), Netherlands (NL), Germany (D), Denmark west (DK), Czech Republic (CZ), Slovakia (SK), Poland (PL), Austria (A), Hungary (H), Slovenia (SV), Croatia (CRT) and part of Bosnia and Herzegovina (BIH).

In the analysis, the grid is divided into five spatial sub-networks; in this way, the spatial networks generated by the model can be compared with several real-world examples of different size. To split the European power grid, a geographical criterion is adopted, given that the spatial aspect is both the main feature describing power-grid networks and the parameter constraint used in the generative model. The five sub-networks, labeled as (A), (B), ..., (E), include the following regions of Europe: (A) I; (B) P and E; (C) D; (D) CZ, SK, PL, A, H, SV, and CRT; and (E) F, B, LU. Fig. 4.2 shows the partition of the European power grid into the above mentioned sub-networks, each describing a different European area. The average number of nodes and links in the sub-networks are respectively 243 and 346.

As in Chapter 3, the network is treated as undirected, so that each sub-network can be described with a binary adjacency matrix $\mathcal{A}$. The sub-networks have topological features similar to the whole European power system. For example, the mean degree and the maximum node degree of the European network are respectively $k = 2.89$ and $\max_i k_i = 2$, while the corresponding average values for these measures in the five sub-networks are

$k = 2.87$ and $\max_i k_i = 2$.

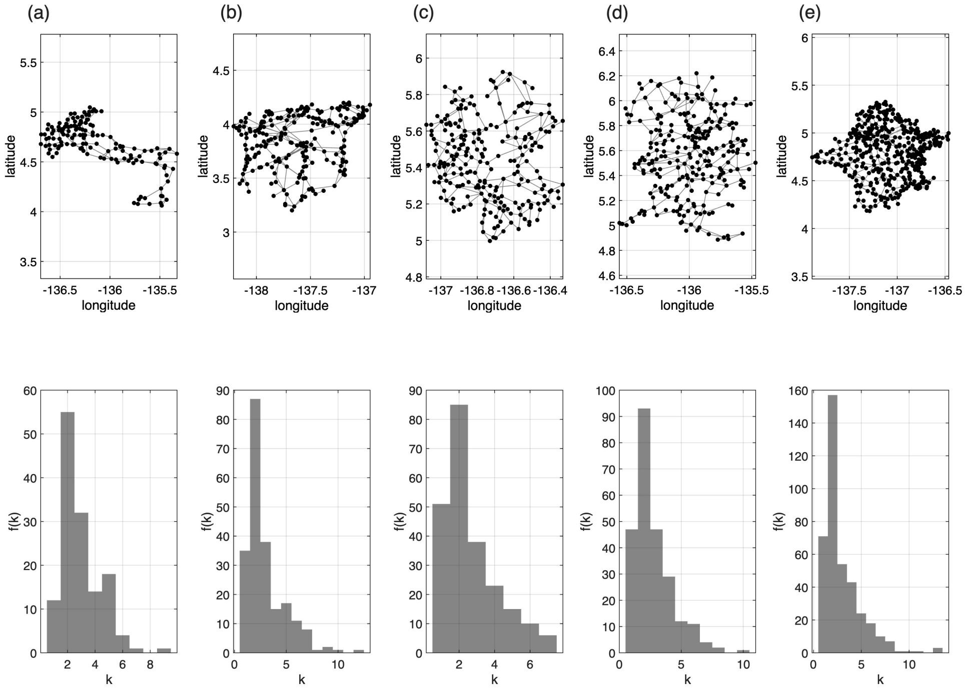

Figure 4.2: Real-world power grids corresponding to different European geographical areas: (a) Italy (137 nodes); (b) Portugal and Spain (216 nodes); (c) Germany (228 nodes); (d) Czech Republic, Slovakia, Poland, Austria, Hungary, Slovenia, and Croatia (246 nodes); and (e) France, Belgium, and Luxembourg (390 nodes). Top row: graphical representation of the power grid. Bottom row: degree distribution of the network.

4.3.2 Model behavior

Two-dimensional spatial networks generated without imposing physical constraints on the node positions and using Eq. (4.2) for selecting the second endpoint of the edges are first considered. The model behavior is studied for different values of its parameters.

The results are initially illustrated for a fixed exemplary value of α, specifically $\alpha = 3$, while considering four different values for the number of nodes, $N \in \{140, 220, 250, 400\}$. For each value of N, 100 samples of spatial networks are generated. In Fig. 4.3, for each N, one example of the generated synthetic networks and the corresponding degree distribution, averaged over the entire ensemble of networks with the same value of N, are presented. These degree distributions align with the ones extracted from real-world networks and illustrated in Fig. 4.2, keeping in mind that the corresponding networks have similar, though not identical, values of the number of nodes and links.

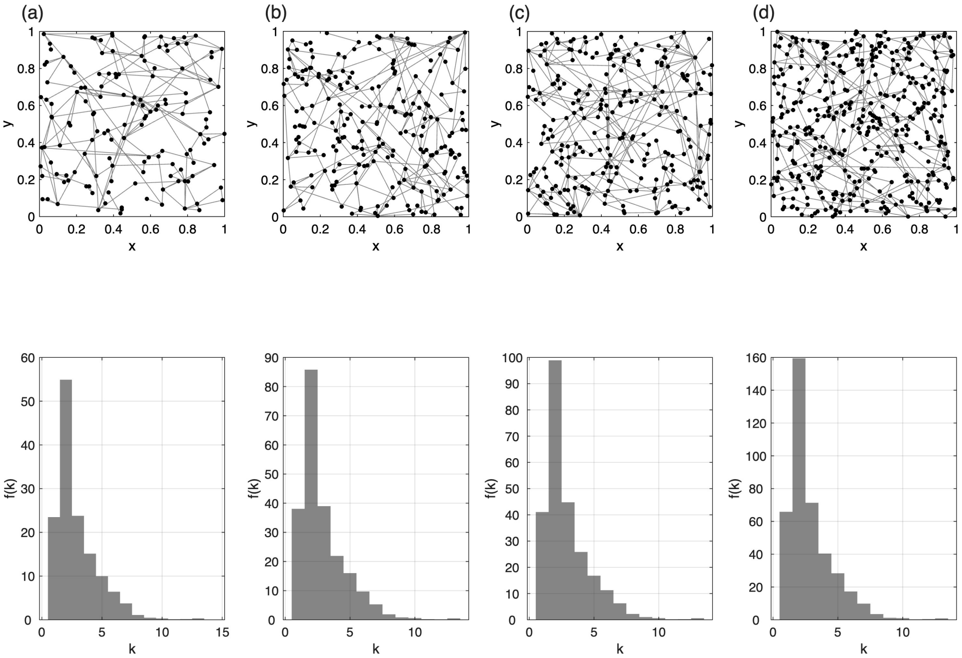

Figure 4.3: Examples of synthetic networks generated with $\alpha = 3$ and a different number of nodes: (a) $N = 140$; (b) $N = 220$; (c) $N = 250$; and (d) $N = 400$. Top row: sample network. Bottom row: degree distribution averaged over an ensemble of 100 synthetic networks generated for each given N.

For the same networks, the values of several topological measures are also reported, which can be used to corroborate the model capability to generate networks with characteristics similar to those of real-world power grids. Specifically, the average shortest path length D, the global clustering coefficient C, the mean degree k, the maximum node degree $\max_i k_i$, and the Rent exponent ρ are considered. The first nine rows of Table 4.1 illustrate the values of these parameters for both real-world (Fig. 4.2) and synthetic (Fig. 4.3) networks. The comparison shows that, despite the empirical nature of the law used for edge selection, the synthetic networks yield similar values for the topological measures when the number of nodes N is close to that of the real-world power grid analyzed.

The model behavior is then analyzed for different values of the parameter α, ranging from 2 to 5 in increments of 0.2. This parameter significantly impacts the network characteristics: as α increases, the probability of connecting nodes that are far apart decreases, leading to networks with more localized connections. The analysis is carried out while also varying $N \in \{140, 220, 250, 400\}$. For each pair of values of N and α, 100 synthetic networks are generated and their average topological properties studied. Fig. 4.4(a) shows that the average shortest path length D grows as N and α increase. This is different from the behavior of the global clustering coefficient C (Fig. 4.4(b)), which instead grows as the parameter α increases, but decreases with N. Altogether, the curves of D and C indicate that α serves as a control parameter that can effectively tune connectivity at both the local and global scales. As expected, the mean degree k, shown in Fig. 4.4(c), is almost constant for each value of N and for each value of α. The value obtained, $k = 2.87$, is close to the average value observed in the five sub-networks of the European power grid, namely $k = 2.84$. This agreement is a clear indication of the effectiveness of the algorithm used for generating the spatial networks. A similar argument holds for the maximum degree $\max_i k_i$, shown in Fig. 4.4(d). In power grids, the maximum peak typically occurs at very small degrees [92], and this property is confirmed since $\max_i k_i$, independently from N and α, is always equal to 2. These low values of the two parameters, k and $\max_i k_i$, also show that the spatial networks satisfy the sparseness property typically found in real-world power grids.

The model is then compared against networks generated using a non-spatial baseline. Specifically, the same procedure for selecting the source nodes of each link is retained, based on a target degree sequence sampled from real-world power grids, but the target nodes are selected uniformly

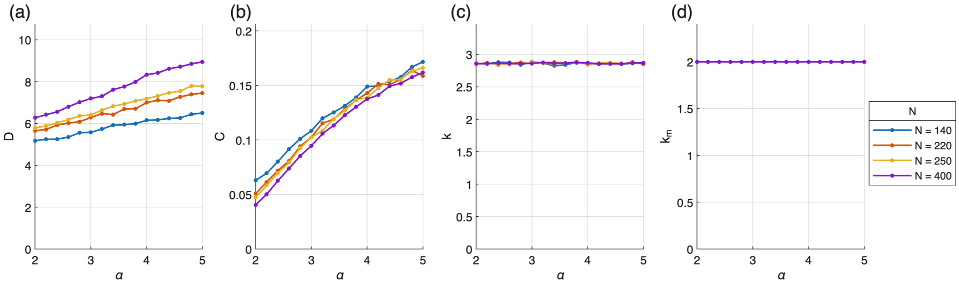

Figure 4.4: Topological properties of synthetic power grid networks generated by the proposed model: (a) average shortest path length D, (b) global clustering coefficient C, (c) mean degree k, and (d) maximum node degree $\max_i k_i$. Results are averaged over 100 synthetic networks for each pair of values of N and α.

at random, independently of spatial distance. This mechanism mimics the link assignment process of the spatial generalizations of the Erdős–Rényi model. For brevity, such networks are referred to as *spatial random* (SR) networks. For what concerns node positions, they are assigned uniformly at random within the unit square so as to isolate the effect of spatial embedding and allow for a direct assessment of its contribution to reproducing key topological features.

The last four rows of Table 4.1 show the results for SR networks. While the mean degree and maximum node degree are approximately preserved, other structural measures, such as the global clustering coefficient and the average shortest path length, exhibit substantial deviations from the values observed in the real networks. Notably, the clustering coefficient is consistently an order of magnitude lower, underscoring the structural inadequacy of surrogates generated without incorporating spatial constraints.

4.3.3 Surrogate networks

The application of the generative model to produce synthetic surrogates of power grids is analyzed. A real-world power grid with N nodes is taken as reference, and synthetic networks with the same number of nodes are generated by positioning them according to one of the four constraints introduced at the beginning of this chapter. To exemplify the surrogate networks that can be created by this procedure, Fig. 4.5 shows four examples obtained

Table 4.1: Topological properties of real-world power grids and synthetic networks. The first five rows refer to real-world power grids. The next four rows show the results for synthetic networks generated with our model with $\alpha = 3$. The last four rows refer to SR networks. All synthetic results are averaged over 100 independent realizations. Reported metrics: number of nodes N, number of edges L, average shortest path length D, global clustering coefficient C, mean degree k, local maximum degree k_m, and Rent exponent ρ.

		N	L	D	C	k	k_m	ρ
Power grids	(Fig. 4.2 (a))	137	202	8.14	0.11	2.95	2.00	0.75
Power grids	(Fig. 4.2 (b))	216	319	6.56	0.12	2.95	2.00	0.88
Power grids	(Fig. 4.2 (c))	228	302	8.87	0.07	2.65	2.00	0.78
Power grids	(Fig. 4.2 (d))	246	335	9.66	0.07	2.72	2.00	0.86
Power grids	(Fig. 4.2 (e))	390	571	8.53	0.11	2.93	2.00	0.87
Model	(Fig. 4.3 (a))	140	202	5.58	0.11	2.89	2.00	0.68
Model	(Fig. 4.3 (b))	220	315	6.28	0.10	2.86	2.00	0.69
Model	(Fig. 4.3 (c))	250	360	6.41	0.10	2.88	2.00	0.69
Model	(Fig. 4.3 (d))	400	572	7.20	0.09	2.86	2.00	0.68
SR networks		140	203	4.90	0.019	2.90	2.20	1.07
SR networks		220	318	5.39	0.011	2.90	2.09	1.06
SR networks		250	363	5.48	0.011	2.91	2.08	1.06
SR networks		400	578	6.03	0.006	2.89	2.13	1.04

starting from the whole European power grid and applying the four different constraints for the node positions. In panel (b), the nodes are arranged into arbitrary positions bounded by the rectangular box that encompasses all node positions of the original network. In panel (c), the node positions replicate the general outlines of the point set from the original power grid, while in panel (d) both the real network outlines and the node density distribution within the space are preserved. Finally, in panel (e), the nodes of the surrogates are placed in the same positions of the original power grid and only the edges are randomized. In all cases, Eqs. (4.1) and (4.2) are applied to govern the procedure for connecting the nodes.

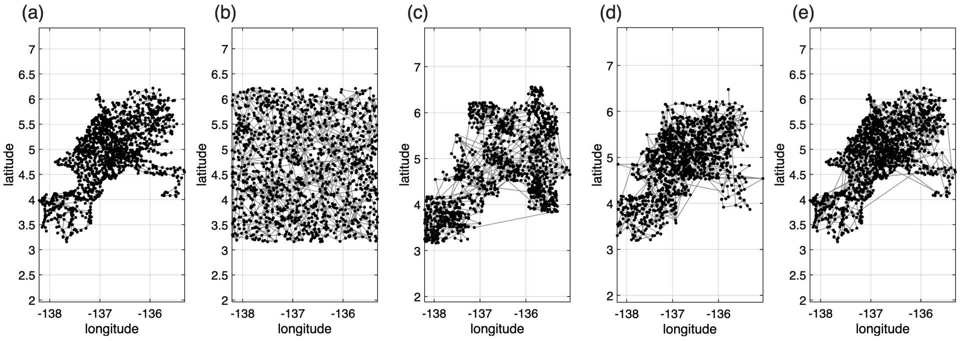

Figure 4.5: The European power grid (a) and four surrogate networks (b)–(e) generated by the proposed model. The surrogates are obtained by applying constraint 1 (b), constraint 2 (c), constraint 3 (d), or constraint 4 (e).

A more systematic analysis is then carried out by considering each of the five sub-networks shown in Fig. 4.2. For each sub-network, an ensemble of 100 surrogate networks is generated under each of the four physical constraints described earlier, resulting in a total of 400 surrogate networks for each sub-network. In this case, Eqs. (4.1) and (4.3) are applied in the phase of edge generation. To characterize the structure of the surrogate networks, for each sample the following quantities are calculated: the average shortest path length D, the global clustering coefficient C, the mean degree k, the modularity Q, and the Rent exponent ρ. These metrics provide insight into both the local and global connectivity properties of the surrogate networks, allowing an assessment of how well they replicate the structural features of the original power grids.

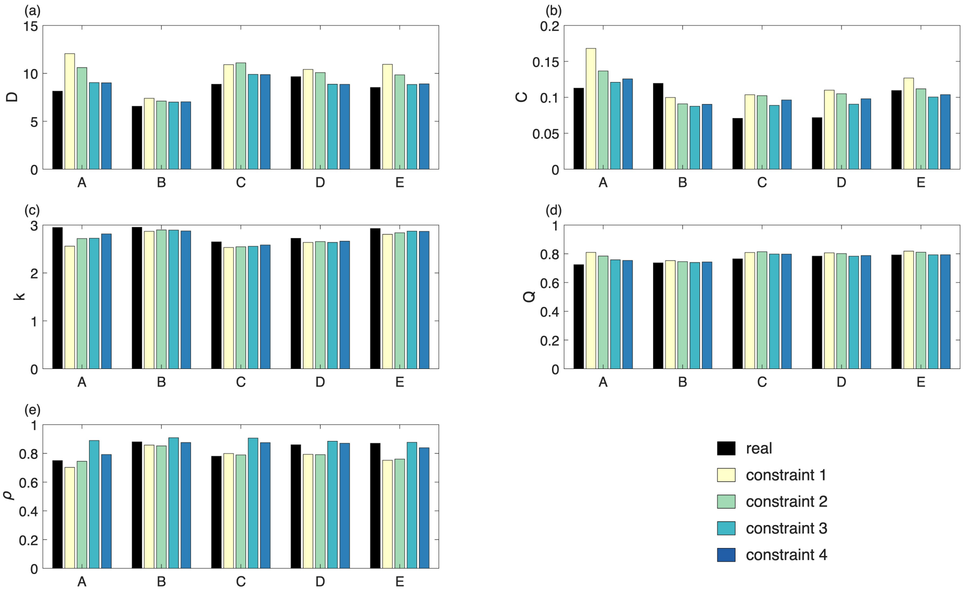

Figure 4.6: Values of the average shortest path length D, the global clustering coefficient C, the mean degree k, the modularity Q, and the Rent exponent ρ measured for different networks: real power grid networks, here highlighted in black, and synthetic networks generated following one between four physical constraints of the generative model. Measures are divided in five groups, from A to E, for each of the five power grid sub-networks (see Fig. 4.2(a–e)).

Fig. 4.6 reports the results of this analysis by comparing the average values of these metrics with those found in the corresponding original power grid. For the reference networks (shown in black in Fig. 4.6), the metrics are calculated for each individual network, while for the surrogate networks the reported values are averages computed over the ensemble of 100 generated samples. The characteristics of the original networks are in general well replicated in the synthetic data. This is supported by the outcomes of a statistical analysis based on the One Sample Kolmogorov–Smirnov test [14], which demonstrates that the differences between the metrics in the real and synthetic networks are not statistically significant. The Kolmogorov–Smirnov test, a non-parametric method, compares the mean value from an ensemble of sample data (in this case, the metrics from the surrogate networks) to a target value, namely the metric measured in the original power grid. The resulting p-values were consistently higher than the threshold of 0.01, as shown in Table 4.2, supporting the null hypothesis that the mean values of the two sets (original and surrogate networks) are not significantly different. At the same time, the values in Table 4.2 are quite heterogeneous, indicating that in some cases the synthetic values align very closely with the real values, while in others the similarity is less marked. For example, the average shortest path length of subnetwork A is better reproduced using constraints 3 and 4 (p-values 0.32 and 0.50, respectively) rather than 1 and 2 (p-values 0.02 and 0.06, respectively). As another example, the global clustering coefficient of subnetwork E is better reproduced using constraints 2–4 (p-values 0.83, 0.46, and 0.71, respectively) than with constraint 1 (p-value 0.28). These findings suggest a non-trivial relationship between the topological characteristics of the network and the choice of model parameters required to accurately replicate them.

4.4 Applications to brain networks

The discussion now moves from technological systems, exemplified by power grids, to biological systems, focusing on the brain. As in the previous case, spatial constraints and topological properties play a central role in shaping the structure of the network. In this context, the nervous system provides a paradigmatic example of a natural complex network whose spatial organization is tightly interwoven with its functional properties.

The nervous system can be analyzed using graph theory tools, where the brain is represented as a network with nodes corresponding to anatomical regions and edges representing either structural or functional connections. The focus here is on structural networks, where the edges represent anatomical connections between neural regions. Different from functional connections, which are derived from the analysis of statistical associations between neural nodes, links in structural networks represent physical connections, i.e. synapses or axonal projections, between brain regions. The structure of a brain network is mapped with diffusion tensor imaging (DTI), a magnetic resonance imaging (MRI) technique that uses the restricted diffusion of water in the three spatial directions through myelinated nerve fibers to identify anatomical connectivities [21]. Another technique to reconstruct anatomical connections is diffusion weighted imaging (DWI), which, instead, uses the diffusion of water molecules to identify links between neuronal regions [72]. The geometry and topology of the networks identified by these techniques are shaped by the spatial features of the brain [23]. Their inherent complexity and the need for accurate modeling of spatial relationships make them a valuable subject for exploring the capabilities of the proposed generative approach. Topological structure and geometric relationships between brain regions are the main properties on which generative rules are based to reproduce the network topology [16]. Generative models are often used to create surrogates that share some properties with real networks while also being formed by randomized processes.

Generating synthetic brain networks is crucial for adhering to ethical guidelines and protecting patient privacy. When analyzing real patient data for research or clinical purposes, significant privacy concerns arise, particularly because brain-computer interface (BCI) technologies grant access to highly personal and identifiable information [66, 2]. Generative models can effectively simulate real brain networks, capturing their essential features while safeguarding sensitive information. These synthetic datasets preserve the typical characteristics of the original data without compromising patient confidentiality or exposing any identifying details. Furthermore, the collection of structural brain data, using advanced and costly technologies such as DTI, is a complex and time-consuming process [101]. These devices are not readily available in all laboratories, and obtaining a sufficient sample size [24], particularly for patients with specific characteristics under investigation, is often challenging. This limitation can be addressed through the use of generative models, which can simulate data and replicate the key characteristics of real datasets, providing researchers with an alternative solution to the scarcity of the original data.

Altogether, these considerations highlight the importance of developing generative models for brain networks. The need to reproduce structural and spatial features while ensuring interpretability and data privacy makes the brain a compelling case for testing the proposed approach. In the following, attention is directed to constructing surrogate brain networks and assessing their ability to capture the characteristic properties of empirical data.

4.4.1 Reference empirical data

The second case study concerns networks representing human brain data. This application highlights the use of the generative model for spatial networks embedded in a three-dimensional space, in contrast to power grids, which are inherently two-dimensional. The analysis is based on the open dataset named ”Max Planck Institut Leipzig Mind-Brain-Body Dataset” (LEMON) [9], focusing, as in [59], on a subgroup of the sample participants. The selected data refer to 136 participants, aged between 20 and 30 years, including 98 males and 38 females. The dataset contains both resting state functional Magnetic Resonance Imaging (rs-fMRI) and Diffusion Weighted Imaging (DWI) for all participants. Since the interest here lies in structural rather than functional links, the analysis is restricted to DWI data.

An unsupervised voxel-level clustering analysis was performed to identify six macro-regions: frontal lobe, parietal lobe, occipital lobe, temporal lobe, insula, and subcortical structures (including thalamus, basal ganglia, amygdala, and hippocampus). Subsequently, an initial Parcellation Atlas (iPA) was employed to aggregate the micro-regions obtained from the six macro-regions. Different aggregation levels resulted in nine iPAs, of which five are used in the present analysis. These correspond to networks characterized by 183, 391, 568, 729, and 964 nodes. A representative network for each iPA, selected from a randomly chosen participant, is shown in Fig. 4.8 as a sagittal brain section. For reference, the brain surface is displayed in the background using BrainNet Viewer [110], a visualization tool for human brain connectomics.

For the purposes of the analysis, the networks were preprocessed in order to obtain undirected and unweighted structures. A threshold at the 90th percentile of the original weight values was applied: when a pair of nodes was connected by a link with a weight exceeding this threshold, the corresponding element in the post-processed binary adjacency matrix was set to one, and zero otherwise.

4.4.2 Model behavior

Analogously to the case of power grids (Sec. 4.3.2), spatial networks generated from human brain connectome data were also examined without imposing physical constraints on the node positions, and using Eqs. (4.1) and (4.2) to select the edges. The behavior of the model was analyzed for different values of N and α. Specifically, networks with $N = \{200, 400, 550, 700, 900\}$ were considered, while the control parameter α was varied from 2 to 20 in increments of 1. Without loss of generality, the target values for the node degrees, namely $\bar{k}_1, \ldots, \bar{k}_N$, were sampled from the degree distribution of the iPA$_{568}$ network of each subject. Similar results hold for the other parcellations.

The average values of the main topological measures, obtained from an ensemble of 100 synthetic networks, are reported in Fig. 4.7. The quantities considered are the average shortest path length D, the global clustering coefficient C, the mean degree k, and the modularity Q, each shown as a function of α and N. The observed trends are consistent with those reported in Fig. 4.4 for power grids, suggesting that the general dependence of these parameters on α is not affected by the dimensionality of the embedding space.

The comparison with the values reported for the real-world iPA networks in the first ten rows of Table 4.3 indicates that, for $\alpha = 20$, the model reproduces key structural properties of the empirical networks, in particular those of the iPA$_{568}$ case. For example, when $N = 550$ and $\alpha = 20$, and averaging over 100 independent realizations, the resulting networks have $D = 2.27$, $C = 0.47$, $k = 56.53$, $Q = 0.48$, and $\rho = 1.03$, values that are in close agreement with the corresponding empirical measures.

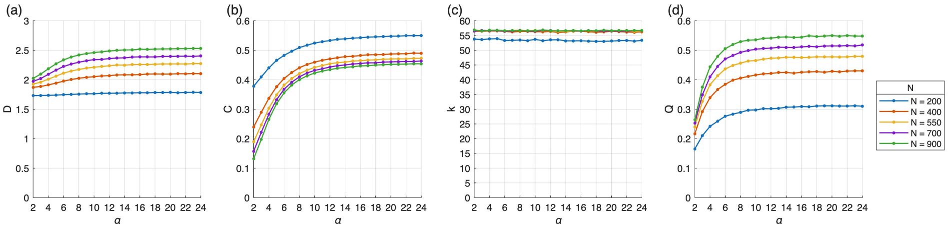

Figure 4.7: Topological properties of synthetic brain networks generated by the proposed model from averaged (see Sec. 2.3) real-world networks: (a) average shortest path length D; (b) global clustering coefficient C; (c) mean degree k; (d) modularity Q. Results are averaged over 100 synthetic networks for different values of N and α.

A comparison with SR networks was also carried out. In this case, node positions were randomly assigned within a unit cube, in order to reproduce the three-dimensional embedding of the data. The corresponding results, reported in the last five rows of Table 4.3, show that although the degree distribution is maintained, other topological properties diverge significantly. In particular, both the clustering coefficient and the modularity are strongly reduced when spatial constraints are not considered. This highlights the relevance of distance-dependent mechanisms in link construction for reproducing the topological and spatial characteristics of brain networks.

4.4.3 Surrogate networks

The application of the generative model to human brain networks is illustrated in the following. A subject, denoted as s, is randomly selected from the set of 136 subjects, and the five DWI structural networks corresponding to the different iPAs of the connectome of this subject are considered. For each of these networks, illustrated in the first column of Fig. 4.8, 100 surrogates with the same number of nodes of the iPA are generated by applying one of the four physical constraints to set the spatial arrangement of the nodes, and using Π_i as in Eq. (4.1) and $\Pi_j = \Pi_j^1$ with $\alpha = 20$ as in Eq. (4.2) to govern edge selection. The target degrees, $\bar{k}_1, \ldots, \bar{k}_N$, used to construct the new structures, are sampled from the degree distribution of the analyzed iPA. An example network for each case is shown in columns 2–5 of Fig. 4.8, with each column corresponding to one of the four constraints for each iPA represented in the rows.

For all generated networks, the average shortest path length D, the global clustering coefficient C, the mean degree k, the modularity Q, and the Rent exponent ρ were calculated and compared with the corresponding values in the original networks. For each ensemble of 100 surrogate networks generated for each physical constraint, with $N = 183, 391, 568, 729, 964$, Table 4.4 reports the average values of D, C, k, Q, and ρ along with the number of nodes N and of edges L. The One Sample Kolmogorov–Smirnov test was applied to these values, returning a p-value higher than 0.1 for all cases and all parameters D, C, k, Q, and ρ. This outcome indicates that the null hypothesis is not rejected, showing that the mean values observed in the surrogate networks cannot be considered significantly different from

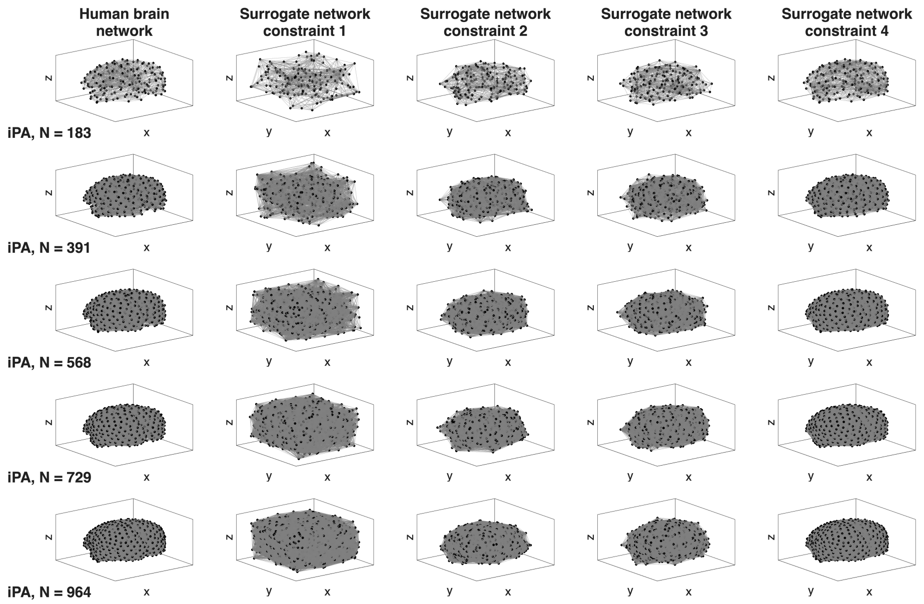

Figure 4.8: DWI brain networks (first column) and corresponding surrogates (columns 2–5) generated by the model. The rows correspond to different iPAs [59] of subject $s = 1$ of the "Max Planck Institut Leipzig Mind-Brain-Body Dataset" – LEMON [9], while columns 2–5 display examples of surrogate networks generated by applying one of the four physical constraints.

those of the original real data.

An extended analysis was then performed by considering all 136 subjects and generating 100 surrogate networks for each iPA and physical constraint. For each iPA, all brain networks associated with the 136 subjects of the dataset were examined to derive the cumulative degree distribution. Then, for each surrogate of size $N = \{183, 391, 568, 729, 964\}$, the target degrees, $\bar{k}_1, \dots, \bar{k}_N$, were sampled from the degree distribution corresponding to the respective iPA network size. In this way, for each iPA 400 synthetic networks were obtained, subdivided into four groups of 100, with each group using one of the four physical constraints for node positioning. For each set, five topological metrics were computed, namely average shortest path length D, global clustering coefficient C, mean degree k, modularity Q, and Rent exponent ρ. The results are presented in Fig. 4.9, where the average topological measures for each surrogate set (ranging from light green to blue, each color representing a different physical constraint) are compared with the real values of the corresponding original network (in black). The values of the original networks are well replicated in the synthetic networks. The One Sample Kolmogorov–Smirnov test confirmed this agreement: as shown in Table 4.5, the test returned a p-value always higher than 0.1, indicating that the synthetic results cannot be considered significantly different from the real values. In the case of brain networks, a complex interplay is observed between model parameters, including the chosen physical constraint, and the topological characteristics of the resulting synthetic networks.

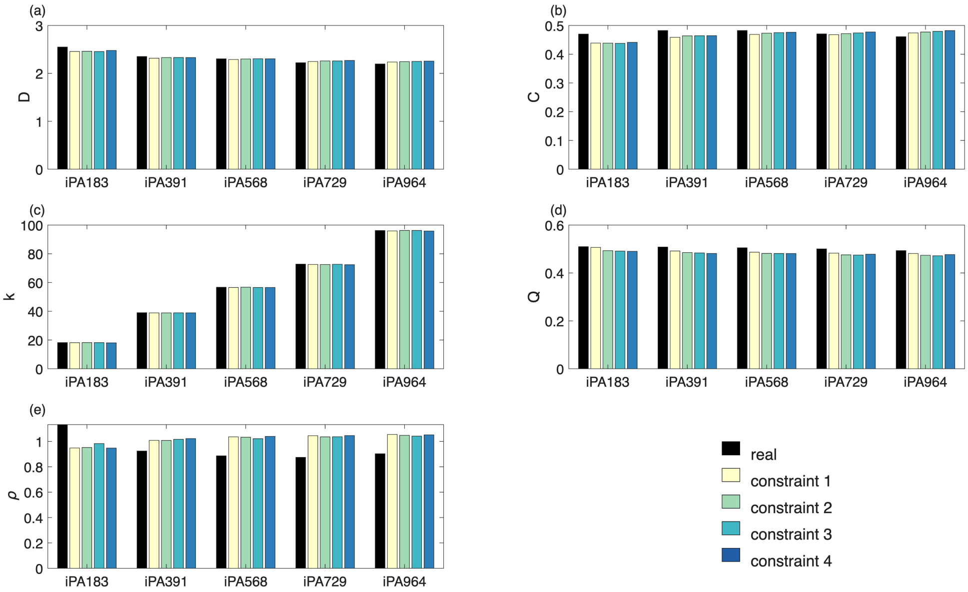

Figure 4.9: The values of average shortest path length D, global clustering coefficient C, mean degree k, modularity Q, and Rent exponent ρ measured across different networks: real brain networks (highlighted in black) and synthetic networks generated according to one of four physical constraints from the generative model. The results are organized into five groups, each corresponding to a specific iPA network size.

Table 4.2: p-values from the One Sample Kolmogorov–Smirnov test comparing different network metrics — specifically, average shortest path length D, global clustering coefficient C, and modularity Q — calculated for real power grid sub-networks versus 100-sample synthetic networks. The following table displays p-values, consistently above 0.01, for each of the four constraint types (1–4, see Fig. 4.5) and each of the five sub-networks (A–E, see Fig. 4.2(a–e), supporting the validity of our model in generating realistic synthetic power grid networks.

	A	B	C	D	E
D: real vs constraint 1	0.02	0.26	0.12	0.65	0.02
D: real vs constraint 2	0.06	0.28	0.08	0.77	0.06
D: real vs constraint 3	0.32	0.40	0.46	0.32	0.61
D: real vs constraint 4	0.50	0.42	0.46	0.26	0.65
C: real vs constraint 1	0.12	0.40	0.08	0.08	0.28
C: real vs constraint 2	0.42	0.22	0.18	0.14	0.83
C: real vs constraint 3	0.75	0.12	0.50	0.36	0.46
C: real vs constraint 4	0.71	0.12	0.16	0.16	0.71
Q: real vs constraint 1	0.02	0.42	0.02	0.14	0.06
Q: real vs constraint 2	0.02	0.67	0.02	0.28	0.10
Q: real vs constraint 3	0.02	0.91	0.12	0.97	0.99
Q: real vs constraint 4	0.18	0.69	0.04	0.79	0.85
ρ: real vs constraint 1	0.81	0.77	0.89	0.46	0.18
ρ: real vs constraint 2	0.91	0.63	0.89	0.40	0.22
ρ: real vs constraint 3	0.06	0.87	0.10	0.77	0.93
ρ: real vs constraint 4	0.55	0.89	0.22	0.89	0.75

Table 4.3: Topological properties of real-world brain networks and synthetic networks. The first five rows refer to real-world brain networks from the reference iPA sample, with results obtained as averages of measures taken from each subject network. The next five rows show the results for synthetic networks generated with the proposed model with $\alpha = 20$. The last five rows refer to SR networks. All synthetic results are averaged over 100 independent realizations. Reported metrics: number of nodes N, number of edges L, average shortest path length D, global clustering coefficient C, mean degree k, modularity Q, and Rent exponent ρ.

	N	L	D	C	k	Q	ρ
Brain networks	183	1665	2.55	0.47	18.20	0.51	1.13
Brain networks	391	7624	2.35	0.48	39.00	0.51	0.92
Brain networks	568	16103	2.30	0.48	56.70	0.50	0.89
Brain networks	729	26536	2.22	0.47	72.85	0.50	0.87
Brain networks	964	46374	2.20	0.46	96.31	0.49	0.90
Model	200	5312	1.79	0.55	53.12	0.31	1.04
Model	400	11288	2.10	0.49	56.44	0.43	1.03
Model	550	15545	2.27	0.47	56.53	0.48	1.03
Model	700	19803	2.40	0.46	56.58	0.52	1.03
Model	900	25501	2.52	0.45	56.67	0.55	1.02
SR networks	200	5709	1.71	0.35	57.09	0.09	1.04
SR networks	400	11365	1.86	0.17	56.82	0.10	1.03
SR networks	550	15637	1.90	0.13	56.86	0.11	1.03
SR networks	700	19839	1.93	0.10	57.68	0.11	1.04
SR networks	900	25501	1.97	0.08	56.67	0.11	1.03

Table 4.4: Values of the number of nodes N, number of edges L, average shortest path length D, global clustering coefficient C, mean degree k, modularity Q, and Rent exponent ρ for both human brain networks and surrogate networks. The original data refer to subject $s = 1$ from the 183, 391, 568, 729, 964-node iPA dataset. Surrogate networks are generated using Π_i and $\Pi_j = \Pi_j^1$ with $\alpha = 20$, applying the four physical constraints. For surrogate networks, reported values are averages over 100 samples for each constraint.

	N	L	D	C	k	Q	ρ
Real	183	1665	2.56	0.47	18.20	0.53	1.23
Constraint 1	183	1651	2.46	0.44	18.04	0.51	0.96
Constraint 2	183	1674	2.45	0.44	18.30	0.49	0.96
Constraint 3	183	1656	2.47	0.44	18.10	0.49	0.94
Constraint 4	183	1663	2.46	0.44	18.18	0.49	1.01
Real	391	7624	2.34	0.48	39.00	0.53	0.95
Constraint 1	391	7639	2.31	0.46	38.08	0.49	1.02
Constraint 2	391	7604	2.33	0.46	38.90	0.48	1.01
Constraint 3	391	7689	2.33	0.46	38.82	0.48	1.01
Constraint 4	391	7603	2.33	0.47	38.89	0.48	1.02
Real	568	16103	2.31	0.49	56.70	0.52	0.91
Constraint 1	568	16087	2.29	0.47	56.64	0.49	1.03
Constraint 2	568	16095	2.30	0.47	57.67	0.48	1.03
Constraint 3	568	16111	2.30	0.47	56.73	0.48	1.03
Constraint 4	568	16122	2.31	0.48	56.77	0.48	1.03
Real	729	26536	2.23	0.48	72.80	0.50	0.86
Constraint 1	729	26467	2.25	0.47	72.61	0.48	1.05
Constraint 2	729	26459	2.25	0.47	72.59	0.48	1.04
Constraint 3	729	26568	2.26	0.47	72.89	0.48	1.04
Constraint 4	729	26418	2.27	0.48	72.48	0.48	1.04
Real	964	46417	2.21	0.47	96.40	0.50	0.91
Constraint 1	964	46318	2.24	0.47	96.10	0.48	1.06
Constraint 2	964	46394	2.25	0.48	96.25	0.47	1.04
Constraint 3	964	46419	2.24	0.48	96.30	0.47	1.04
Constraint 4	964	46218	2.25	0.48	96.89	0.48	1.05

Table 4.5: p-values from the One Sample Kolmogorov–Smirnov test comparing different network metrics — specifically, average shortest path length D, global clustering coefficient C, modularity Q, and Rent exponent ρ — calculated for real brain networks versus 100-sample synthetic networks. Surrogate networks are generated using Eq. (4.1) and Eq. (4.2), with $\alpha = 20$. The table displays p-values, consistently above 0.1, for each of the four constraint types (1–4) and each of the five iPA brain networks.

	iPA_{183}	iPA_{391}	iPA_{568}	iPA_{729}	iPA_{964}
D: real vs constraint 1	0.18	0.36	0.73	0.91	0.36
D: real vs constraint 2	0.36	0.73	0.55	0.91	0.18
D: real vs constraint 3	0.18	0.91	0.18	0.73	0.36
D: real vs constraint 4	0.55	0.55	0.73	0.36	0.18
C: real vs constraint 1	0.18	0.18	0.18	0.18	0.18
C: real vs constraint 2	0.18	0.18	0.18	0.55	0.18
C: real vs constraint 3	0.18	0.18	0.18	0.36	0.18
C: real vs constraint 4	0.18	0.18	0.36	1.00	0.18
Q: real vs constraint 1	0.55	0.18	0.18	0.18	0.18
Q: real vs constraint 2	0.18	0.18	0.18	0.18	0.18
Q: real vs constraint 3	0.18	0.18	0.18	0.18	0.18
Q: real vs constraint 4	0.18	0.18	0.18	0.18	0.18
ρ: real vs constraint 1	0.18	0.55	0.18	0.18	0.18
ρ: real vs constraint 2	0.36	0.36	0.18	0.18	0.18
ρ: real vs constraint 3	0.36	0.18	0.18	0.18	0.18
ρ: real vs constraint 4	0.36	0.55	0.18	0.18	0.18

Part II

Network control

Chapter 5

Synchronization via edge snapping

Adaptive networks are commonly defined as systems of dynamical units interacting through a graph topology whose structure evolves together with the node dynamics [50, 39].

Over the past decades, adaptive networks have proven to be a powerful framework for describing, analyzing, and controlling both natural and artificial systems. Numerous social and biological systems inherently possess the capacity to reorganize their interaction patterns, either by creating or removing connections among their elements or by adjusting the intensity of existing ones [56]. Such flexibility makes them naturally amenable to a representation in terms of adaptive networks [89]. Drawing inspiration from these natural examples, adaptive-network concepts have also been applied to the design of control strategies in artificial systems, where modifying link weights or rewiring the network structure provides an effective means to achieve specific collective behaviors [35].

Adaptation can enter a network through different mechanisms. A first line of studies assumes the topology fixed, while allowing the edge weights to evolve in order to promote synchronization. In this setting, early contributions proposed centralized strategies in which all couplings are updated simultaneously, according to a rule based on global information about the state of the system [26, 34]. In contrast, decentralized schemes avoid global communication and let each node regulate the strength of its interactions locally, adjusting its coupling with neighbors as a function of their state mismatch; in this way, each link or node is endowed with its own adaptive law [115, 34]. Subsequent work extended the idea by allowing not only edge weights but also the network structure itself to evolve, with links being created or removed to facilitate synchronization across the system [35, 6]. This perspective has been applied, for instance, to ensembles of Kuramoto oscillators, where adaptive rewiring leads to the emergence of patterns at mesoscopic and macroscopic scales [8, 54]. Importantly, in most of these approaches the adaptive rules impose bounds on the overall coupling strength. In the context of more general dynamics, including chaotic oscillators, the edge snapping mechanism has been introduced to model the switching on and off of connections. In this formulation, the state of a link evolves like a particle in a double-well potential, driven by the mismatch of its endpoints [35]. The inertial term in the link dynamics ensures that an edge is activated only when the mismatch is sufficiently large and sustained, thereby avoiding spurious activations due to short-lived fluctuations.

The edge snapping approach has proven effective in modeling the processes that drive complex networks toward a steady-state topology. Remarkably, when applied to financial systems to capture influence dynamics, the resulting degree distribution reproduced patterns consistent with those found in corporate elite networks [41, 37]. From the viewpoint of control theory, edge snapping can also be interpreted as a control strategy, in which the network continues to reconfigure itself until synchronization or pinning control is attained [35, 36]. However, in view of technological applications, it becomes essential to account for constraints on available resources, which limit the number of links that can be activated. In fact, depending on the initial conditions, the mechanism may lead to steady-state networks characterized by relatively high average degree [38].

To overcome this limitation in general models of complex networks, the edge snapping mechanism is here extended to incorporate explicit constraints on the number of edges that can be activated. The approach relies on the multilayer framework [68, 69], where one layer represents the physical system under control and the additional layers implement the various components of the control strategy, for instance the proportional, integral, and derivative terms of a distributed controller.

In our model, the system is organized into two layers: a static backbone network forming the first layer, and a switching adaptive control layer forming the second, which regulates the activation of additional connections. Unlike the classical edge snapping approach, here (i) the activation or removal of edges is governed by a discontinuous output function of the edge state, and (ii) the input driving the snapping dynamics is specifically designed to balance the benefit of activating new edges to promote synchronization with the necessity of limiting their overall number. The binary discontinuous output enables each node to autonomously track the number of active incident links, while the input term in the edge dynamics enforces an asymptotic constraint on the node degree. Analytical results demonstrate that, under suitable assumptions on the local dynamics and on the coupling intensity, the system admits locally asymptotically stable steady-state configurations. In addition, it is possible to establish a lower bound on the coupling strength, below which the snapping dynamics are not sufficient to ensure synchronization among the network nodes.

The effectiveness of the proposed method is initially assessed on networks of chaotic Rössler oscillators. Its robustness is then examined in a more realistic setting by applying it to a model of the Italian high-voltage power grid, where the response of the system to line faults is tested. In this context, the adaptive control layer is specifically evaluated with respect to its ability to reconfigure the network after the occurrence of a fault on a given transmission line.

5.1 Multilayer network model

5.1.1 Rössler oscillator as node dynamics

The elementary dynamics assigned to each node follow the Rössler equations, already introduced in Chapter 2 (see Eq. (2.12)). This choice ensures that the network is composed of units exhibiting chaotic behavior with well-characterised properties, which makes them particularly suitable as a benchmark for the analysis of synchronization. Within the present context, the Rössler system is not examined in isolation but rather regarded as the fundamental building block whose interactions through the coupling architecture give rise to collective behavior.

In the two-layer setting adopted here, each node i evolves according to

$$\begin{aligned}\dot{\mathbf{x}}_i(t) = {} & \mathbf{f}_{\text{Rössler}}(\mathbf{x}_i) \\ & + k\sum_{j=1}^{N} a^b_{ij}\big(\mathbf{h}^{(b)}(\mathbf{x}_j) - \mathbf{h}^{(b)}(\mathbf{x}_i)\big) \\ & + q\sum_{j=1}^{N} a^c_{ij}(t)\big(\mathbf{h}^{(c)}(\mathbf{x}_j) - \mathbf{h}^{(c)}(\mathbf{x}_i)\big), \qquad i = 1, \dots, N,\end{aligned} \tag{5.1}$$

where $\mathbf{f}_{\text{Rössler}}$ coincides with the vector field in Eq. (2.12), k and q are the coupling gains on the backbone and on the adaptive control layer, and $\mathbf{h}^{(b)}$ and $\mathbf{h}^{(c)}$ denote the corresponding inner coupling functions. The matrices $A^{(b)} = [a^b_{ij}]$ and $A^{(c)}(t) = [a^c_{ij}(t)]$ represent, respectively, the time-invariant backbone adjacency and the time-varying control-layer adjacency. By definition, $a^c_{ij}(t) \in \{0, 1\}$ is the binary state of the control edge between nodes i and j at time t, which is updated by the snapping dynamics introduced in Sec. 5.1.2 and constrained by the control objectives in Eqs. (5.2).

The focus of the subsequent analysis is therefore on how the interplay between intrinsic chaotic trajectories and network connectivity determines the stability and convergence of synchronized states.

5.1.2 Structural configuration of the control layer

The purpose of the control layer is to achieve two concurrent objectives, which may be in contrast with each other:

$$\lim_{t\to+\infty} (\mathbf{x}_i(t) - \mathbf{x}_j(t)) = 0, \qquad i, j = 1, \dots, N, \tag{5.2a}$$

$$\lim_{t\to+\infty} \sum_{j=1}^{N} a^c_{ij}(t) \le \bar{d}_i, \qquad i = 1, \dots, N, \tag{5.2b}$$

namely, the emergence of global synchronization and the enforcement of an asymptotic bound $\bar{d}_i$ on the degree of each node in the control layer.

To meet these conditions in a decentralized way, the edge snapping scheme [38] is adopted. In this approach, the activation of links is regulated by assigning a dynamical system to each pair of nodes (i, j). For every such pair, a continuous state $\sigma_{ij} \in \mathbb{R}$ is introduced, which evolves according to the dynamics of a particle in a double-well potential. The binary control edge is then obtained as the thresholded output of σ_{ij}, so that

$$\ddot{\sigma}_{ij}(t) + \zeta\dot{\sigma}_{ij}(t) + \frac{\partial}{\partial\sigma_{ij}(t)}V(\sigma_{ij}(t)) = u_{ij}(t), \tag{5.3a}$$

$$a^c_{ij}(t) = \Theta(\sigma_{ij}(t) - 0.5), \tag{5.3b}$$

where ζ is a damping parameter, $V(\sigma_{ij})$ is a double-well potential, $u_{ij}(t)$ is an external input, and Θ denotes the Heaviside step function. The potential is chosen such that the undriven dynamics in (5.3a) exhibit two stable equilibria, located at 0 and 1, and one unstable equilibrium at 0.5. As in standard edge snapping, a convenient choice is

$$V(\sigma_{ij}) = b\,\sigma^2_{ij}(\sigma_{ij} - 1)^2, \tag{5.4}$$

with $b > 0$ tuning the barrier height between the two wells.

The distinctive feature of the present formulation with respect to the original edge snapping framework is the design of the input $u_{ij}(t)$, which here explicitly accounts for resource limitations in the control layer. For each node i, we define

$$\delta_i(t) = \max\left\{0, \sum_{j=1}^{N} a^c_{ij}(t) - \bar{d}_i\right\}, \tag{5.5}$$

which measures the excess degree of node i beyond the prescribed bound $\bar{d}_i$. For a pair of nodes (i, j), the variable $\delta_{ij}(t) = \delta_i(t) + \delta_j(t)$ is then positive whenever at least one of the two nodes has exceeded its bound. Based on this definition, the input is specified as

$$u_{ij}(t) = \beta_1 g(e_{ij}(t)) - \beta_2\delta_{ij}(t), \tag{5.6}$$

where $e_{ij}(t) = \mathbf{x}_j(t) - \mathbf{x}_i(t)$ and

$$g(e_{ij}(t)) = \|e_{ij}(t)\|. \tag{5.7}$$

Accordingly, the input is composed of two terms. The first, $\beta_1 g(e_{ij}(t))$, depends on the local synchronization error between nodes i and j and, for $\beta_1 > 0$, favours the creation of a link if the two nodes are not aligned. The second, $-\beta_2\delta_{ij}(t)$, penalizes the formation of an edge whenever one of the nodes already exceeds its allowed degree. The parameters β_1 and β_2 regulate the trade-off between the synchronization requirement in (5.2a) and the resource constraint in (5.2b).

5.2 Analytical framework

In this section, a theoretical analysis is presented of the local stability of solutions of model (5.3) that are pertinent to the control goals in (5.2), namely solutions where (i) all nodes are synchronous, $\mathbf{x}_1 = \cdots = \mathbf{x}_N = \mathbf{x}_s$, and (ii) the control edges are time-invariant, $a^c_{ij}(t) \equiv a^c_{ij} \in \{0, 1\}$, satisfying the degree bounds $\sum_{j=1}^N a^c_{ij} \leq \bar{d}_i$ for all i.

Before analyzing the stability of the synchronized state, it is useful to briefly recall the framework of the Master Stability Function (MSF), originally introduced in [81]. The MSF formalism decouples the local node dynamics from the network structure by linearizing the system around the synchronization manifold and projecting perturbations onto the eigenmodes of the Laplacian matrix. Each mode evolves independently according to a variational equation whose stability is determined by the MSF, which therefore provides a general and quantitative criterion for assessing the onset and robustness of synchronization across different topologies and coupling schemes.

In this framework, let us indicate with $\delta\mathbf{x}_i = \mathbf{x}_i - \mathbf{x}_s$ the transverse dynamics of the i-th unit, and let us define $\delta\sigma_{ij} = \sigma_{ij} - \bar{\sigma}_{ij}$ as the deviation of the edge state from the considered equilibrium $\bar{\sigma}_{ij}$. Furthermore, we can introduce

$$\delta\mathbf{x} = \left[\delta\mathbf{x}_1^\top, \ldots, \delta\mathbf{x}_N^\top\right]^\top,$$

and the vectors $\delta\sigma$ and $\dot{\delta\sigma}$ stacking all the $\delta\sigma_{ij}$'s and $\dot{\delta\sigma}_{ij}$'s, respectively. Linearising the dynamics of $(\delta\mathbf{x}, \delta\sigma)$ around the origin yields

$$\begin{aligned} \dot{\delta\mathbf{x}} &= \left[I_N \otimes J\mathbf{f}(\mathbf{x}_s) - k\mathbf{L}^{(b)} \otimes J\mathbf{h}^{(b)}(\mathbf{x}_s) - q\mathbf{L}^{(c)} \otimes J\mathbf{h}^{(c)}(\mathbf{x}_s)\right]\delta\mathbf{x}, \\ \ddot{\delta\sigma} &= -\zeta\dot{\delta\sigma} - 2b\delta\sigma, \end{aligned} \tag{5.8}$$

where we considered that the gradient of g is null at the origin, and that δ_{ij} is constant (and equal to zero) around the origin.

We remark that the assumption of a zero gradient of g at the origin is important to decouple the perturbations on the weights of the adaptive layer. This assumption is true for g in Eq. (5.7), and is therefore a design criterion for the updating law for the adaptive weights of the proposed approach. In Eq. (5.8) we denoted with $J\mathbf{f}(\mathbf{x}_s)$, $J\mathbf{h}^{(b)}(\mathbf{x}_s)$, and $J\mathbf{h}^{(c)}(\mathbf{x}_s)$ the Jacobians of the functions $\mathbf{f}$, $\mathbf{h}^{(b)}$, and $\mathbf{h}^{(c)}$, respectively, evaluated at the synchronization manifold $\mathbf{x}_s$, and with $\mathbf{L}^{(c)}$ the constant Laplacian matrix corresponding to the reference equilibrium $\bar{\sigma}$ of the network edge state σ.

Notice that $\mathbf{L}^{(c)}$ depends on the system evolution, and hence on the updating rule for the adaptive links, the system parameters, and initial conditions. In particular, while in classic edge snapping all possible topologies on N nodes are a feasible equilibrium configuration, here an admissible equilibrium topology should be such that δ_i is zero for all i, as implied by Eqs. (5.5)–(5.6), that is, the equilibrium degree $(\mathbf{L}^{(c)})_{ii}$ of node i in the control layer should not exceed $\bar{d}_i$.

Since local node and edge dynamics in (5.8) are decoupled, we can study them separately. First, we notice that selecting positive values for ζ and b yields asymptotic stability of the linearised dynamics of $\delta\sigma$. We can then focus on the nodal dynamics around the synchronization manifold.

We start by observing that both $\mathbf{L}^{(b)}$ and $\mathbf{L}^{(c)}$ are symmetric, positive semi-definite matrices, and thereby they share the eigenvalue $\lambda_1 = 0$, with associated eigenvector $\mathbf{v}_1 = [1, \ldots, 1]^\top$ (for convenience we sort the eigenvalues in ascending order). In general, the other eigenvalues and eigenvectors of the two matrices are different, such that they cannot be simultaneously diagonalised.

Let us then consider the matrix T containing the left eigenvectors of $\mathbf{L}^{(b)}$ and define the transformed variable $\xi = (T^{-1} \otimes I_n)\delta\mathbf{x}$. The dynamics of ξ can be written as

$$\begin{aligned}\dot{\xi} = \Big[&I_N \otimes J\mathbf{f}(\mathbf{x}_s) - k\,\mathrm{diag}\{\lambda_1(\mathbf{L}^{(b)}), \ldots, \lambda_N(\mathbf{L}^{(b)})\} \otimes J\mathbf{h}^{(b)}(\mathbf{x}_s) \\ &- q\tilde{\mathbf{L}}^{(c)} \otimes J\mathbf{h}^{(c)}(\mathbf{x}_s)\Big]\xi\end{aligned} \tag{5.9}$$

where $\tilde{\mathbf{L}}^{(c)} = T^{-1}\mathbf{L}^{(c)}T$. Considering the spectral properties of matrices $\mathbf{L}^{(b)}$ and $\mathbf{L}^{(c)}$, Eq. (5.9) can be recast as

$$\begin{aligned}\dot{\xi}_1 &= J\mathbf{f}(\mathbf{x}_s)\,\xi_1, \\ \dot{\xi}_j &= [J\mathbf{f}(\mathbf{x}_s) - k\lambda_j(\mathbf{L}^{(b)})J\mathbf{h}^{(b)}(\mathbf{x}_s)]\xi_j - q\sum_{\ell=2}^{N} \tilde{\mathbf{L}}^{(c)}_{j\ell} J\mathbf{h}^{(c)}(\mathbf{x}_s)\,\xi_\ell,\end{aligned} \tag{5.10}$$

for $j = 2, \ldots, N$. Note that the first mode is associated to $\lambda_1 = 0$ and determines the stability of the motion along the synchronization manifold, whereas all the other modes are transverse to this manifold. When these transverse modes damp out, synchronization is stable, such that synchronization stability can be assessed by characterising the largest Lyapunov exponent of the dynamics of $\xi_2, \dots, \xi_N$.

When the coupling function is the same in the two layers, that is, $\mathbf{h}^{(b)} = \mathbf{h}^{(c)}$, a considerable simplification takes place. Under this assumption, in fact, we can define a new matrix $\mathbf{M} = k\mathbf{L}^{(b)} + q\mathbf{L}^{(c)}$ and rewrite the first equation in (5.8) as

$$\dot{\delta\mathbf{x}} = [I_N \otimes J\mathbf{f}(\mathbf{x}_s) - \mathbf{M} \otimes J\mathbf{h}^{(b)}(\mathbf{x}_s)]\delta\mathbf{x}. \tag{5.11}$$

If $k, q \geq 0$, since both $\mathbf{L}^{(b)}$ and $\mathbf{L}^{(c)}$ are symmetric and positive semi-definite, then also matrix $\mathbf{M}$ is symmetric and positive semi-definite. Therefore, we can select the transformation T as the matrix whose columns are obtained by juxtaposing the left eigenvectors of $\mathbf{M}$, and define again $\xi = (T^{-1} \otimes I_n)\delta\mathbf{x}$, thereby obtaining

$$\dot{\xi}_i = [J\mathbf{f}(\mathbf{x}_s) - \lambda_i(\mathbf{M})J\mathbf{h}^{(b)}(\mathbf{x}_s)]\xi_i, \tag{5.12}$$

where $\lambda_1(\mathbf{M}), \dots, \lambda_N(\mathbf{M})$ are the eigenvalues of $\mathbf{M}$ sorted in ascending order, that is, $0 = \lambda_1(\mathbf{M}) \leq \lambda_2(\mathbf{M}) \leq \cdots \leq \lambda_N(\mathbf{M})$.

Local stability of the synchronization manifold requires that the transverse modes in (5.12), i.e. those for $i = 2, \dots, N$, damp out. This condition can be checked by calculating the maximum Lyapunov exponent associated to the generic equation

$$\dot{\eta} = [J\mathbf{f}(\mathbf{x}_s) - \alpha J\mathbf{h}^{(b)}(\mathbf{x}_s)]\eta$$

as a function of the parameter α, i.e. $\Lambda_{\max}(\alpha)$, and verifying that $\Lambda_{\max}(\alpha) < 0$ for all $\alpha \in \{\lambda_2(\mathbf{M}), \dots, \lambda_N(\mathbf{M})\}$.

The exact form of $\mathbf{L}^{(c)}$ (and therefore of $\mathbf{M}$) depends on the trajectory followed by the system (5.3) with input as in Eq. (5.6). Since the input is a function only of the state variables, the system becomes autonomous, and the trajectory it follows depends solely on the system equations, its parameters (including the bound on available resources), and its initial conditions. As $\mathbf{L}^{(c)}$ is not determined prior to the trajectory of the system, the eigenvalues of $\mathbf{M}$ cannot be computed in advance, and the condition $\Lambda_{\max}(\alpha) < 0$ cannot be directly verified.

Nonetheless, Eq. (5.12) can still provide some *a priori* insights on the stability of the synchronous manifold. First, we point out that Eq. (5.12) has the exact form of the Master Stability Function (MSF) that characterises the synchronization stability in single-layer complex networks of coupled oscillators [81], and, therefore, the classification into different types of MSF can still be applied [19].

For the sake of simplicity, let us focus on systems with type II MSF, which represents the case of an unbounded stability region, whereby there exists a threshold value $\alpha \in \mathbb{R}$ such that $\Lambda_{\max}(\alpha) < 0$ for $\alpha \in [\alpha_1, \infty)$. For this class of systems, local stability of the synchronization manifold requires $\lambda_2(\mathbf{M}) > \alpha_1$.

As $\mathbf{M}$ is the sum of two positive semi-definite matrices, we have that

$$\lambda_2(\mathbf{M}) \geq \max\{k\lambda_2(\mathbf{L}^{(b)}),\, q\lambda_2(\mathbf{L}^{(c)})\} \geq q\lambda_2(\mathbf{L}^{(c)}). \tag{5.13}$$

Suppose now that the backbone layer is not able to enforce local stability of the synchronization manifold, that is, $\max\{k\lambda_2(\mathbf{L}^{(b)}), q\lambda_2(\mathbf{L}^{(c)})\} = q\lambda_2(\mathbf{L}^{(c)})$, such that the control problem is not trivial. A relevant degenerate case is when there is no backbone network at all, i.e. $k = 0$ and the topology is entirely dictated by the snapping dynamics; in that case $\lambda_2(\mathbf{M}) = q\lambda_2(\mathbf{L}^{(c)})$. Furthermore, let us remind that, according to Eqs. (5.5)–(5.6), an admissible equilibrium configuration for the control layers is such that each node i in the control layer does not overcome the threshold $\bar{d}_i$ introduced in (5.5). Therefore, in this case a necessary condition for synchronisability is the existence of an admissible equilibrium configuration, fulfilling the asymptotic constraint on the maximal number $\bar{d} = \max_i \bar{d}_i$ of edges incident at each node, such that

$$q \geq \frac{\alpha_1}{\lambda_2(\mathbf{L}^{(c)})}.$$

Reminding that the addition of a new edge can never decrease the Laplacian eigenvalues, and denoting with $\mathcal{L}_{\text{reg}}(\bar{d})$ the class of static Laplacian matrices associated to $\bar{d}$-regular graphs (i.e. graphs such that all nodes have degree $\bar{d}$), we would then have that a necessary condition for synchronization is

$$q \geq \frac{\alpha_1}{\lambda_2(\mathbf{L}_{\max}(\bar{d}))},$$

where

$$\mathbf{L}_{\max}(\bar{d}) = \arg \max_{\mathbf{L} \in \mathcal{L}_{\text{reg}}(\bar{d})} \lambda_2(\mathbf{L}).$$

Since an upper bound for the smallest non-zero eigenvalue of the Laplacian is its smallest degree, we then have

$$\lambda_2(\mathbf{L}_{\max}(\bar{d})) \leq \bar{d},$$

thereby obtaining

$$q \geq \frac{\alpha_1}{\bar{d}}. \tag{5.14}$$

When the control gain q is lower than $q^{\Delta} = \alpha_1/\bar{d}$, we can then conclude that synchronization with limited resources cannot be attained without either further increasing q, or relaxing the constraint on the maximal number of edges by modifying $\bar{d}_i$ in Eq. (5.5).

5.3 Results for the Rössler network

The effectiveness of the adaptive strategy is first tested numerically on a network with $N = 12$ Rössler oscillators coupled through their second state variable, as introduced in Sec. 2.5.1. Denoting $\mathbf{x}_i = [x_i \; y_i \; z_i]^\top$, the network dynamics follow Eq. (2.13) with the addition of the adaptive control term described in Eq. (5.6). The backbone topology is the one shown in Fig. 5.1, with coupling coefficient $k = 0.2$. Under these conditions, in the absence of control ($q = 0$), the system does not synchronize. For the adaptive layer, the parameters are set to $b = 5$ in Eq. (5.4), and $\beta_1 = 1$, $\beta_2 = 2.5$ in Eq. (5.6).

The next step is to evaluate whether the presence of the adaptive control layer can enforce synchronization in the network. To this aim, different choices are considered for the parameters of the control layer, in particular q and the resource constraints $\bar{d}_i$ in Eq. (5.5), here assumed equal for all nodes, i.e., $\bar{d}_i = \bar{d}$. For different values of $\bar{d}$ (varied between 2 and 5 with step 1), both the synchronization error E and the maximum degree d_M of the final configuration of the control layer are monitored after transient dynamics vanish, as a function of the control gain q.

The synchronization error is defined as $E = \langle e(t) \rangle_T$, with

$$e(t) = \sqrt{\frac{1}{N(N-1)} \sum_{i=1}^{N} \sum_{\substack{j=1 \\ j \neq i}}^{N} \|\mathbf{e}_{ij}\|}, \tag{5.15}$$

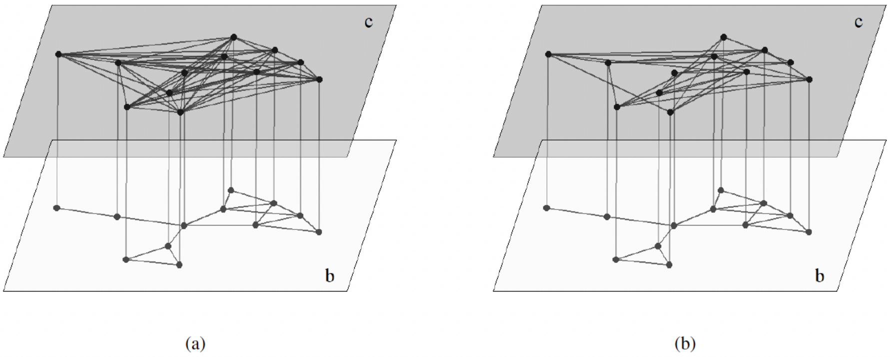

Figure 5.1: Schematic representation of the multilayer network framework and illustrative outcomes of the adaptive control layer in a network of Rössler oscillators. Panel (a) reports the case in which no constraint on the available resources is imposed. With the backbone and control gains set to $k = 0.2$ and $q = 0.2$, respectively, the resulting control topology exhibits a maximum degree $d_M = 10$ and an average degree $\langle d \rangle = 6.34$. Panel (b) shows instead the constrained setting, where the resource limit is enforced by prescribing $\bar{d} = 6$, which yields a control layer with $d_M = 6$ and $\langle d \rangle = 5$. The schematic highlights the node-wise control connections between the backbone and the control layers, denoted by the letters b and c, respectively.

and T is a sufficiently large time window, set to $T = 200\,\mathrm{s}$ in the simulations. The maximum degree d_M is used to verify whether the resource constraint is satisfied.

Figure 5.2(a) shows that the synchronization error E decreases as the control gain q increases, reaching a threshold around $q = 0.1$, above which the network consistently synchronizes. Below this threshold, synchronization is possible only if larger values of $\bar{d}$ are allowed. This is confirmed by panel (b): for low gain values, resources are insufficient, and the snapping mechanism attempts to activate additional edges. However, synchronization cannot be maintained because the asymptotic constraint on resources is violated, with some δ_i in Eq. (5.5) being positive, which forces edge deactivation.

A comparison with the classic edge-snapping approach, which operates without resource constraints, highlights a substantial difference. The classic

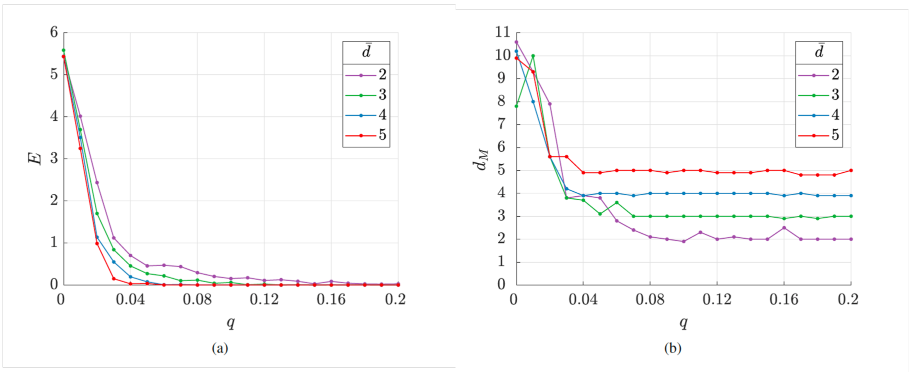

(a)

(b)

Figure 5.2: Average synchronization error E (a) and maximum degree d_M (b) as a function of the control gain q in the network of $N = 12$ depicted in Fig. 5.1 for different values of $\bar{d}$. The coupling strength of the backbone layer is set $k = 0.2$, and results are averaged over 10 runs for each value of q.

mechanism activates a relatively large number of links, not all of which are necessary for synchronization. This is illustrated in Fig. 5.3, where both the maximum degree d_M and the average degree $\langle d \rangle$ of the control layer are reported as a function of q. In this case, some nodes activate all possible links, leading to $d_M = N - 1$, see panel (a). This behavior originates from random initial conditions, where certain nodes start with a high synchronization error, causing full activation of their connections. The proposed adaptive mechanism, instead, accounts in Eqs. (5.5)–(5.6) for the necessity of avoiding saturation of available resources, and therefore leads to a much smaller number of activated links, see panel (b).

To further characterise the system, the analysis is extended to two selected values of $\bar{d}$ (3 and 6), by varying the control gain q between 0 and 0.2 with step 0.01, and the coupling strength k on the backbone layer between 0 and 1 with step 0.05. For each configuration the synchronization error is recorded. The color maps in Fig. 5.4 show that, for both values of $\bar{d}$, synchronization is achieved in a broad region of the parameter space where the coupling coefficients k and q are sufficiently high. A synergy between the two layers emerges: increasing k reduces the minimum q needed for synchronization, and vice versa.

In this setting, the same coupling function is adopted in both layers, i.e.,

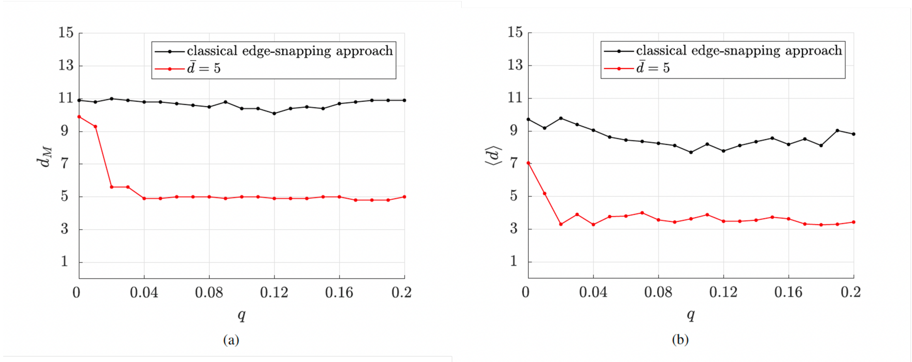

(a) (b)

Figure 5.3: Maximum degree d_M (a) and average degree $\langle d \rangle$ (b) of the control layer as a function of the control gain q for the classic edge snapping mechanism (without resource constraints) and for the proposed adaptive mechanism with $\bar{d} = 5$.

$\mathbf{h}^{(b)} = \mathbf{h}^{(c)}$, so that the stability of synchronization can be studied through Eq. (5.12). The system exhibits a type-II MSF with $\alpha_1 = 0.157$, and, for the backbone network, the smallest non-zero eigenvalue of the Laplacian matrix is $\lambda_2 = 0.273$. Hence, in the absence of control ($q = 0$), synchronization requires $k > \alpha_1/\lambda_2 = 0.575$. Conversely, when the physical coupling is absent ($k = 0$), the necessary condition (5.14) yields, for $\bar{d} = 6$, $q > 0.023$, and for $\bar{d} = 3$, $q > 0.052$, in agreement with Fig. 5.4(b).

Finally, the effect of the adaptive law on the emergent topology is examined in the absence of any backbone structure, i.e., $\mathbf{A}^{(b)} = \mathbf{0}$. In this case, the network is entirely shaped by the adaptive dynamics, corresponding to the single-layer formulation of edge snapping [38]. An ensemble of $N = 100$ Rössler oscillators is considered, starting from $\sigma_{ij}(0) = 0$ for all i, j, i.e., with no active links. The system is evolved with the adaptive law introduced in Sec. 5.1.2, over 100 runs, with and without resource constraints ($\bar{d}_i = \bar{d} = 8$ for all i in Eq. (5.5)). The main effect of bounding the available resources is a shift and truncation of the distribution. With unlimited resources, a Poisson-like degree distribution is observed, whereas with resource limits the distribution peaks at $d = 5$ and is truncated at the bound $d = \bar{d}$.

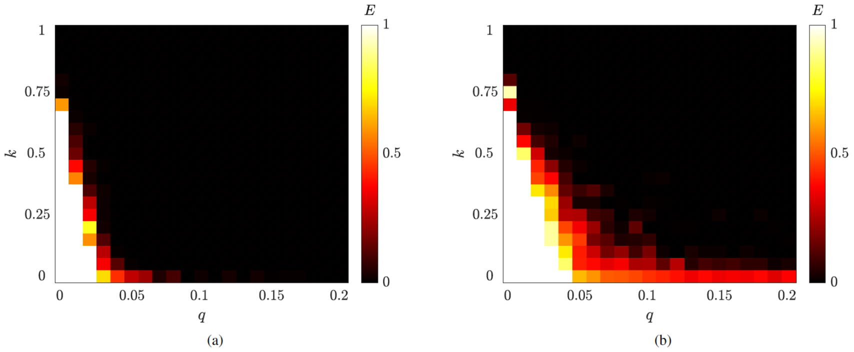

(a)

(b)

Figure 5.4: Color map of the synchronization error E as a function of the control gain q and the coupling strength k of the backbone layer for a system of coupled Rössler oscillators, for $\bar{d} = 6$ (a) and $\bar{d} = 3$ (b), respectively (all values of E larger than 1 are depicted in white). The backbone network is shown in Fig. 5.1. Results are averaged over 10 runs for each pair (q, k).

5.4 Power grid analytical framework

The adaptive law (5.3) is now applied to the control of synchronization in a model of the Italian power grid, in order to demonstrate that the approach is not limited to the canonical network dynamics considered earlier, but extends to systems with more realistic dynamics. In this model the units are no longer identical, and the target synchronization property is phase synchronization rather than complete synchronization. For this reason, the theoretical framework presented in Sec. 5.2 cannot be directly applied. Nevertheless, the proposed control law remains effective, since the essential mechanisms of the adaptive dynamics do not rely on the specific form of the underlying system.

This analysis is particularly relevant in the context of power grids, where the ability to reconfigure the network in response to failures is crucial. Accordingly, a model of the Italian power grid including failure mechanisms on the transmission lines is considered, and the behavior of the control layer is tested under selected line failures.

5.4.1 Swing equation as node dynamics

A power grid equipped with a control cyberlayer [45] with limited resources is considered, that is, under constraints on the number of edges that can be activated. Each of the N nodes of the power system is described by a swing equation according to the synchronous machine representation of the power grid, already introduced in Sec. 2.5.2 (see Eq. (2.16)). In particular, each node is characterised by inertia I_i, damping γ_i, and net power injection P_i, which is positive for generators and negative for loads.

On top of this baseline model, an adaptive control term is introduced in parallel with the physical layer, proportional to the frequency differences with neighboring nodes. The dynamics of each unit then become

$$I_i \frac{d\omega_i}{dt} = P_i - \gamma_i \omega_i + \sum_{j=1}^{N} a_{ij}^b \sin(\theta_j - \theta_i) + q \sum_{j=1}^{N} a_{ij}^c(t)(\omega_j - \omega_i),$$

for $i = 1, \dots, N$, where θ_i and ω_i denote, respectively, the voltage phase angle and angular velocity of the i-th synchronous machine in a rotating reference frame with frequency $\Omega = 2\pi f$. The coefficients a_{ij}^b are the elements of the weighted adjacency matrix describing the operative transmission lines, defined from the electrical parameters as $a_{ij}^b = B_{ij} V_i V_j$. The coefficients $a_{ij}^c(t)$ represent the control-layer adjacency matrix (undirected and unweighted), which evolves according to the adaptive law (5.3)–(5.6).

As in Sec. 3.4, line overloads are modelled by checking whether the power flow across edge (i, j), defined as $F_{ij}(t) = a_{ij}^b \sin(\theta_j - \theta_i)$, exceeds the maximum capacity $C_{ij} = \alpha a_{ij}^b$. The overload condition is expressed by Eq. (3.3). If this condition is satisfied at some time $t = t_f$, the line is assumed to trip and is removed from the operative topology by setting $a_{ij}^b = 0$ for all $t > t_f$.

5.4.2 Structural configuration of the Italian high–voltage transmission network

In the analysis, a fault due to some exogenous event is considered, located at a line (i', j'). This fault generates a transient where the power grid operates out of synchrony, and eventually induces a cascade of failures in other lines where the flow overcomes the maximum capacity [90, 111]. At the same time, the loss of synchrony triggers the adaptive mechanisms embedded in the links of the control layer and activates the control inputs,

$$u_i = q \sum_{j=1}^{N} a^c_{ij} \left(\omega_j - \omega_i\right),$$

which attempt to restore synchrony in the network, thus limiting the flows in the lines. The effectiveness of such a control strategy in preventing the propagation of the faults into a cascade of successive failures has been demonstrated over a static topology, copy of the physical layer, in [45]. In the present case, it is shown that the topology of the control layer can be adaptively selected in a decentralized fashion to avoid the onset of cascading failures and maintain synchronization.

We now specialise the framework to the Italian high-voltage transmission network, detailing topology and parameterization of the swing-equation model, the backbone adjacency, and the metrics E and d_M, under the control objectives and resource constraints stated above (Eqs. (5.2) and (5.5)).

The power grid model is here tailored to the case of the Italian high-voltage (380 kV) transmission network [43, 49, 86, 44, 103, 100]. The system is represented as a homogeneous and undirected network, that is, $a^b_{ij} = a^b_{ji} = k$ if there exists a link between nodes i and j, and $a^b_{ij} = a^b_{ji} = 0$ otherwise. The considered topology comprises $N = 127$ nodes (34 generators and 93 loads) and $L = 171$ links (see Fig. 3.3 in Chapter 3). Following [45], the parameters of the swing-equation dynamics are chosen as $\gamma = 0.1$, $\alpha = 0.6$, $k = 15$, $P_i = -1$ for the load nodes, and $P_i = 2.735$ for the generator nodes, so that the overall system is balanced, i.e., $\sum_{i=1}^{N} P_i = 0$. With this parameter choice, the network operates in synchrony in the absence of faults.

In the adaptive layer, since the controller aims at synchronizing all the frequencies in the grid, the function $g(e_{ij})$ has been considered as depending solely on the frequency difference between nodes i and j, namely $g(e_{ij}) = |\omega_i - \omega_j|$. As in Sec. 5.1, the parameters of the potential function (5.4) are chosen as $\zeta = 1$ and $b = 5$. The control gain is fixed to $q = 15$, whereas the parameters of the control law (5.3) are set to $\beta_1 = 20$ and $\beta_2 = 2.5$.

5.5 Results for the Italian power network

The behavior of the power grid has been first analyzed in the absence of control ($q = 0$) under the following setting: the grid initially operates in synchrony, then, at time $t = t_f = 1\,\mathrm{s}$, a fault occurs in a single line of the network, possibly triggering a cascading failure. The dynamics have been numerically integrated for a total time $T = 20\,\mathrm{s}$, while monitoring the flows to check whether they exceeded the maximum line capacity $C_{ij} = \alpha a^b_{ij}$, thereby leading to line failures.

This analysis reveals the presence of 16 critical lines, namely links that effectively trigger a cascading failure. For these lines, the effect of the adaptive control layer has been studied with the aim of restoring synchronization and preventing cascading failures. As an illustrative example, the failure of line $(10, 16)$ has been considered. In the absence of control, this fault triggers a cascade involving five additional lines [45]. Without any constraint on the resources available at each node, the evolution of the adaptive layer produces a structure with $L_c = 251$ links and an average degree of $\langle d \rangle = 3.95$, see Fig. 5.5(a). However, the majority of these links are not strictly required, as shown by the use of the adaptation rule (5.3)–(5.6) under finite $\bar{d}_i$. Indeed, Fig. 5.5, panels (b–d), demonstrates that the power grid can be successfully controlled, with cascading failures prevented and frequency synchronization recovered after the initial fault, by activating a much lower number of links. Specifically, $L_c = 49$ ($\langle d \rangle = 0.77$) for $\bar{d}_i = 6$, $L_c = 36$ ($\langle d \rangle = 0.57$) for $\bar{d}_i = 5$, and $L_c = 30$ ($\langle d \rangle = 0.47$) for $\bar{d}_i = 4$.

The analysis has been extended to all 16 lines identified as critical, since they trigger cascading failures in the absence of the control layer. Table 5.1 reports, for each line, the differentiated use of resources in four cases: no upper bound on the resources available at each node, as in the classic edge-snapping mechanism, and limited resources with $\bar{d}$ equal to 6, 5, or 4. For each case, the maximum node degree d_M and the average node degree $\langle d \rangle$ in the control layer have been calculated. In all cases, the control input was able to restore synchronization while preventing further line failures in the grid.

In addition, in all scenarios with constrained resources, d_M was always equal to $\bar{d}$, so that the constraints were systematically satisfied. The average degree $\langle d \rangle$, which quantifies the effective number of activated links ($L_c = \langle d \rangle N/2$), was typically much lower than the upper bound d_M, confirming that additional links were activated only where necessary. Moreover, this parameter highlights that some faults demand the activation of more links

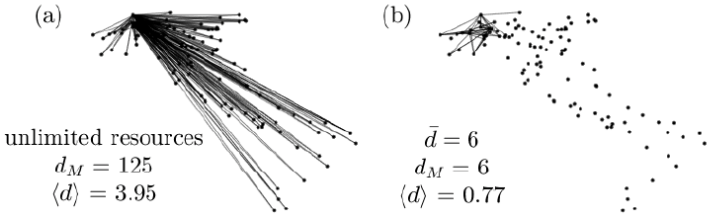

Figure 5.5: Control layer of the Italian high-voltage power grid obtained after failure of the line $(10, 16)$ (shown in red in Fig. 3.3) in the absence of constraints on the available resources (a), and when $\bar{d}$ is equal to 6 (b), 5 (c), and 4 (d), respectively.

than others. For example, under a constraint $\bar{d} = 4$, recovering from a fault in line $(59, 61)$ requires $L_c = 67$ links, whereas a fault in line $(21, 23)$ requires only $L_c = 28$. Although beyond the scope of this work, it would be of interest to investigate whether and how $\langle d \rangle$ or L_c correlate with the topological properties of the initially damaged links.

5.6 Key findings and remarks

A multilayer control protocol for synchronization of coupled dynamical systems under the constraint of limited resources available at each node has been introduced. The control is structured as a second layer, acting in parallel with a set of fixed links that constitute the backbone of the network. The interactions in the control layer are adaptive, in the sense that they can be activated or removed depending on the level of synchronization and the available resources. The adaptive mechanism proposed introduces a discontinuous output function that, together with a modified input to the snapping dynamics, extends the classical edge-snapping algorithm by incorporating constraints on the degree of each node in the network. As in classical edge snapping, the method provides a fully distributed technique able to evolve the structure of the interconnections, in contrast with other approaches [35, 115, 26, 34] that operate only on the coupling gains of a pre-existing network. Differently from the classical edge-snapping algorithm, however, the proposed approach achieves synchronization with a significantly smaller average degree, thereby overcoming a major limitation of the original method.

The effectiveness of the approach has been demonstrated on a network of coupled Rössler oscillators and subsequently tested on a more general setting represented by a model of the Italian high-voltage power grid. In the case of Rössler oscillators, suitable values of the coupling coefficient of the control layer were shown to guarantee the stability of the synchronous solution while simultaneously satisfying the constraints imposed by the limited resources. Moreover, the two layers act in synergy, so that a lower control gain is required as the coupling strength in the backbone network increases.

The Italian high-voltage power grid, modelled through swing equations and incorporating line failures induced by the dynamical evolution of the system, has been considered to test the robustness of the control strategy in a more realistic context. The adaptive control law successfully guaranteed synchronization and prevented cascading failures even when the available resources were limited.

Several directions for future research naturally arise. In all the numerical results presented, the same upper bound was imposed on the degree of every node, although the strategy is general and allows for heterogeneous limits, thereby differentiating the resources available at different nodes. Another generalization is to restrict the set of links that can be adapted in the control layer, so as to embed additional structural constraints into the evolved topology. Finally, in scenarios where the number of controlled nodes is relevant, the adaptive control law could be applied only to a selected subset of the backbone nodes, further reducing the complexity of the control layer.

The adaptive mechanism complements the reconstruction methods of Chapter 3, as both exploit local information and sparse structures, and precedes the synchronization analysis on physical circuits in Chapter 6.

Table 5.1: Characteristic parameters of the adaptive control layer of the Italian high-voltage (380kV) power grid model, for different locations of initial fault and assumptions on the available resources at each node.

Fault line	$\bar{d}$	d_M	$\langle d \rangle$	Fault line	$\bar{d}$	d_M	$\langle d \rangle$
(10,16)	∞	125	3.95	(15,16)	∞	124	7.69
	6	6	0.77		6	6	0.38
	5	5	0.57		5	5	0.35
	4	4	0.47		4	4	0.27
(15,17)	∞	123	7.59	(20,21)	∞	124	2.27
	6	6	0.43		6	6	0.54
	5	5	0.36		5	5	0.68
	4	4	0.28		4	4	0.52
(21,22)	∞	117	4.06	(21,23)	∞	125	4.00
	6	6	1.18		6	6	0.74
	5	5	0.98		5	5	0.57
	4	4	0.79		4	4	0.44
(27,59)	∞	122	5.76	(33,35)	∞	126	5.81
	6	6	0.83		6	6	0.47
	5	5	0.85		5	5	0.46
	4	4	0.69		4	4	0.46
(36,38)	∞	123	7.67	(59,60)	∞	123	3.97
	6	6	0.47		6	6	1.78
	5	5	0.47		5	5	1.07
	4	4	0.36		4	4	1.13
(59,61)	∞	124	7.67	(64,78)	∞	123	4.27
	6	6	1.42		6	6	1.37
	5	5	1.13		5	5	0.93
	4	4	1.06		4	4	1.09
(75,88)	∞	121	4.25	(76,79)	∞	122	4.24
	6	6	1.15		6	6	1.37
	5	5	1.54		5	5	1.23
	4	4	1.09		4	4	1.06
(79,80)	∞	123	5.78	(86,88)	∞	123	5.81
	6	6	0.74		6	6	0.69
	5	5	0.85		5	5	0.68
	4	4	1.02		4	4	0.60

Chapter 6

Synchronization time slowdown under increasing coupling in chaotic circuit networks

Synchronization in networks of chaotic electronic circuits provides a rigorous setting to investigate the interplay between topology, coupling strength, and nonlinear dynamics. Transistor-based chaotic oscillators offer analytical tractability and experimental feasibility, enabling validation of theoretical predictions on synchronization stability and convergence time. This chapter presents the circuit model for the Minati–Frasca (MF) oscillator in isolated, pairwise-coupled, and networked configurations, derives the Master Stability Function (MSF) for the adopted coupling protocol, and reports numerical results on synchronization error and synchronization time, including robustness under perturbations and scaling with network size.

6.1 Mathematical framework for coupled oscillators

The transistor-based chaotic oscillator adopted in this chapter is the *Minati–Frasca oscillator*. Its electrical scheme, dimensional formulation, and compact rescaled model have already been introduced in Section 2.5.4. The following recalls only the aspects relevant to the synchronization analysis and specifies the parameter settings used in the numerical investigations.

The dimensionless equations of an isolated oscillator are given in Eq. (2.22), with parameters a, b, c, d, e, f, g defined in Eq. (2.23). The network extension, reported in Eq. (2.25), describes N coupled circuits, where the adjacency matrix $A = \{a_{ij}\}$ encodes the topology and σ denotes the normalized coupling gain.

Throughout this chapter the circuit parameters are fixed to the reference values reported in Section 2.5.4. Variations of the intrinsic parameters are not considered, as the focus is on the role of the coupling strength σ and of the network topology in determining synchronization behavior. Numerical experiments explore the dynamics from pairs of coupled oscillators to larger networks with heterogeneous connectivity patterns.

All simulations are obtained by integrating Eq. (2.25) with the fourth-order Runge–Kutta method, using an integration step $\Delta t = 10^{-3}$ in rescaled time units. Initial conditions are randomly chosen within the attractor basin, ensuring generality of the results.

This formulation makes the system directly amenable to analysis through the Master Stability Function (MSF), since the separation between local dynamics and network structure is explicit in Eq. (2.25). The following sections employ this formalism to determine synchronization stability regimes and to quantify the dependence of the synchronization time on the coupling intensity.

6.2 Master Stability Function analysis

To study the theoretical conditions for synchronization, the standard network synchronization formalism is adopted. Accordingly, the network of N coupled oscillators, represented by Eqs. (2.24), is described, in general terms, by

$$\dot{\mathbf{x}}_i = \mathbf{f}(\mathbf{x}_i) + \sigma \sum_{j=1}^{N} a_{ij}\, \mathrm{H}(\mathbf{x}_j - \mathbf{x}_i)\,, \tag{6.1}$$

where $i = 1, \ldots, N$, $\mathbf{f}$ is the uncoupled dynamics, $\mathbf{x}_i \in \mathbb{R}^n$ is the state vector, σ is the coupling strength, and H is the inner coupling matrix specifying the coupling channel. The synchronization manifold, defined by $\mathbf{x}_1 = \cdots = \mathbf{x}_N = \mathbf{x}_s$, follows

$$\dot{\mathbf{x}}_s = \mathbf{f}(\mathbf{x}_s). \tag{6.2}$$

Linearising around the manifold with perturbation $\delta\mathbf{x}_i = \mathbf{x}_i - \mathbf{x}_s$ yields

$$\dot{\delta\mathbf{x}} = [\mathrm{I} \otimes \mathrm{D}\mathbf{f}|_{\mathbf{x}_s} - \sigma \mathrm{L} \otimes \mathrm{H}]\, \delta\mathbf{x}, \tag{6.3}$$

where $\delta\mathbf{x} = [\delta\mathbf{x}_1^T, \delta\mathbf{x}_2^T, \ldots, \delta\mathbf{x}_N^T]^T$, $\mathrm{D}\mathbf{f}|_{\mathbf{x}_s}$ is the Jacobian of $\mathbf{f}$ at $\mathbf{x}_s$, and L is the graph Laplacian. Since L is positive semi-definite for undirected connected graphs, its eigenvalues satisfy $0 = \lambda_1 < \lambda_2 \leq \cdots \leq \lambda_N$. Block-diagonalisation leads to

$$\dot{\boldsymbol{\xi}}_i = [\mathrm{D}\mathbf{f}|_{\mathbf{x}_s} - \sigma\lambda_i \mathrm{H}]\, \boldsymbol{\xi}_i.$$

Introducing $\alpha = \sigma\lambda_i$, the Master Stability Equation (MSE) is

$$\dot{\boldsymbol{\zeta}} = [\mathrm{D}\mathbf{f}|_{\mathbf{x}_s} - \alpha \mathrm{H}]\, \boldsymbol{\zeta}. \tag{6.4}$$

From this equation, the maximum Lyapunov exponent $\lambda_{\max}$ is computed as a function of α, obtaining the Master Stability Function (MSF), $\lambda_{\max}(\alpha)$. Based on the shape of $\lambda_{\max}(\alpha)$, three classes of MSF can be distinguished [18]: type I, always unstable; type II, with a single threshold α_c such that $\lambda_{\max}(\alpha) > 0$ for $\alpha < \alpha_c$ and $\lambda_{\max}(\alpha) < 0$ for $\alpha > \alpha_c$; and type III, with a stability interval $\alpha \in [\alpha_1, \alpha_2]$. For type II, any connected network can be synchronised provided $\sigma > \alpha_c/\lambda_2$, whereas for type III stability requires $\lambda_N/\lambda_2 < \alpha_2/\alpha_1$.

For the MF oscillator with coupling only through the first state, Eqs. (2.24) correspond to (6.1) with

$$\mathbf{f}(\mathbf{x}) = \begin{pmatrix} \dfrac{a-x_1}{bg} - \dfrac{x_3+x_4}{b} \\ \dfrac{x_4 - \beta\,\Gamma(x_3)\tanh(x_2/(2d))}{c} \\ \dfrac{x_1-d}{e} \\ \dfrac{x_1-x_2}{f} \end{pmatrix}, \quad \mathrm{H} = \begin{pmatrix} 1 & 0 & 0 & 0 \\ 0 & 0 & 0 & 0 \\ 0 & 0 & 0 & 0 \\ 0 & 0 & 0 & 0 \end{pmatrix}.$$

The Jacobian $\mathbf{Df}|_{\mathbf{x}_s}$ is

$$\mathbf{Df}|_{\mathbf{x}_s} = \begin{pmatrix} -\dfrac{1}{bg} & 0 & -\dfrac{1}{b} & -\dfrac{1}{b} \\ 0 & \dfrac{\beta\,\Gamma(x_{3,s})\left(\tanh^2(x_{2,s}/(2d))-1\right)}{2cd} & -\dfrac{\beta\,\Theta(x_{3,s})\tanh(x_{2,s}/(2d))}{c} & \dfrac{1}{c} \\ \dfrac{1}{e} & 0 & 0 & 0 \\ \dfrac{1}{f} & -\dfrac{1}{f} & 0 & 0 \end{pmatrix} \tag{6.5}$$

where $\Theta(x)$ is the Heaviside function, i.e., $\Theta(x) = 0$ for $x < 0$ and $\Theta(x) = 1$ for $x > 0$. The maximum Lyapunov exponent is computed following [96] (pp. 116–117) with integration step $\delta t = 10^{-5}$, iterations per cycle $I =$ 5,000,000, and number of cycles $C = 15$. The resulting MSF is shown in Fig. 6.1. The curve starts at a positive value, corresponding to the chaotic behavior of the isolated dynamics, decreases rapidly crossing the axis, and remains negative as α increases. This indicates a type II behavior with a single transition point. For large α, $\lambda_{\max}$ remains negative but its absolute value gradually decreases, which significantly affects convergence to synchronization when two or more MF circuits are coupled.

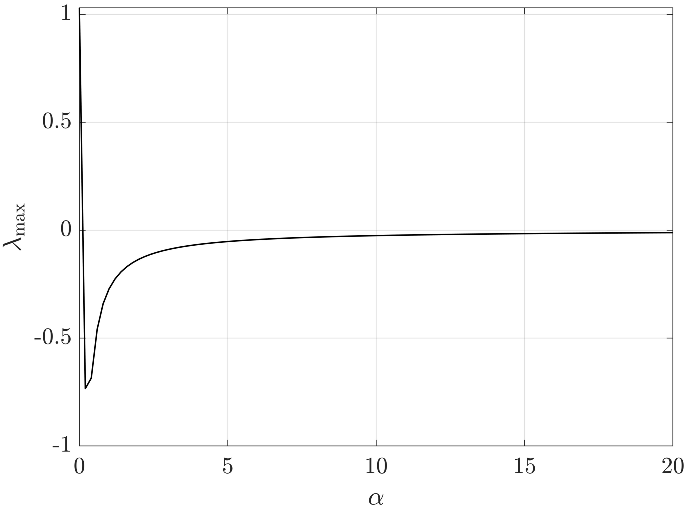

Figure 6.1: Maximum transverse Lyapunov exponent $\lambda_{\max}$ as a function of α for the transistor-based chaotic oscillator in Eq. (2.24) with parameters set as in (2.23). For convenience, the independent parameter was divided by k_I.

6.3 Numerical results

6.3.1 Synchronization error and synchronization time

To monitor synchronization in Eqs. (2.24) and (2.25), the synchronization error at time t, denoted as $e(t)$, is defined as

$$e(t) = \left(\frac{1}{N(N-1)} \sum_{i=1}^{N} \sum_{\substack{j=1 \\ j \neq i}}^{N} \|\mathbf{x}_j - \mathbf{x}_i\|^2 \right)^{\frac{1}{2}}, \tag{6.6}$$

where $\|\mathbf{x}\| = \sqrt{x_1^2 + x_2^2 + x_3^2 + x_4^2}$ denotes the Euclidean norm in $\mathbb{R}^4$. To smooth transient effects, the average value of $e(t)$ over the interval $[T_D/2, T_D]$ is considered, namely

$$E = \langle e(t) \rangle_{T_D},$$

which is referred to as the synchronization error.

To gain further insight into the dynamics, the synchronization time t_s is tracked, defined as the minimum time such that for all $t > t_s$ the condition

$e(t) < \varepsilon$ holds, with $\varepsilon = 0.01$. An approximate expression for t_s is obtained by assuming

$$e(t) \simeq e_0 \, e^{-\lambda_{\max}(\alpha) t}, \tag{6.7}$$

with $e_0 = e(0)$, yielding

$$t_s \simeq -\frac{1}{\lambda_{\max}(\alpha)} \ln\left(\frac{\varepsilon}{e_0}\right). \tag{6.8}$$

6.3.2 Synchronization in a pair of two MF circuits

Consider synchronization in a pair of coupled MF circuits, modelled by Eqs. (2.24), or equivalently by Eqs. (2.25) with $N = 2$. For two coupled units, the Laplacian matrix is $\mathrm{L} = \begin{pmatrix} 1 & -1 \\ -1 & 1 \end{pmatrix}$ with eigenvalues $\lambda_1 = 0$ and $\lambda_2 = 2$. There is a single transverse mode associated with λ_2, and the condition for synchronization stability reduces to $\lambda_{\max}(2\sigma) < 0$.

The dependence of the synchronization error E on the coupling strength σ is shown in Fig. 6.2, considering different simulation lengths T_D. For $T_D = 10^6$ the error becomes zero at the MSF-predicted onset, indicating consistency between theory and simulations. For shorter T_D, e.g. $2 \cdot 10^5$, a non-zero error emerges for large σ, increasing with σ, signaling slow convergence to the synchronization manifold: stability is retained, yet trajectories require long times to settle, which makes the error profile appear similar to a type III MSF with an apparent second threshold due to finite-time effects.

Figure 6.3 compares t_s computed from simulations of Eqs. (2.24) against the approximation (6.8). Initial conditions are $\mathbf{x}_1(0) = [0.9 \;\; 0 \;\; 0 \;\; 0]^T$ and $\mathbf{x}_2(0) = [0.05 \;\; 0.8 \;\; 0 \;\; 0]^T$, so that $e(0) = 1.1673$. Since $\lambda_{\max}$ is an average measure and $e(t)$ need not be monotone, Eq. (6.8) underestimates t_s, yet it captures the trend: as σ increases, the absolute value of $\lambda_{\max}$ decreases at large α, thus t_s increases. Hence, higher coupling strength does not necessarily aid synchronization; it may prolong the settling time.

Figure 6.4 shows that the synchronization time t_s exhibits markedly different behaviors depending on the voltage source V_s. For $V_s = 2$ (black circles), t_s increases approximately linearly with the coupling strength σ, indicating that stronger coupling unexpectedly slows down the convergence to the synchronized state. In contrast, for $V_s = 5$ (white circles), synchronization occurs within a few time units and is essentially insensitive to

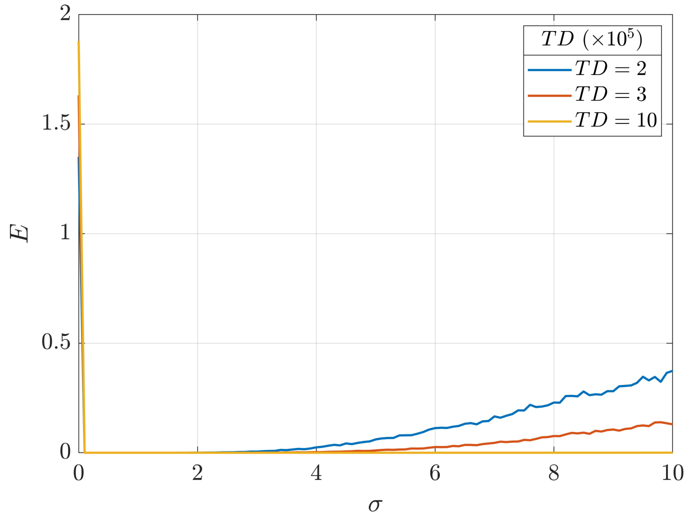

Figure 6.2: Synchronization error E as a function of the coupling strength σ for different values of the simulation duration T_D.

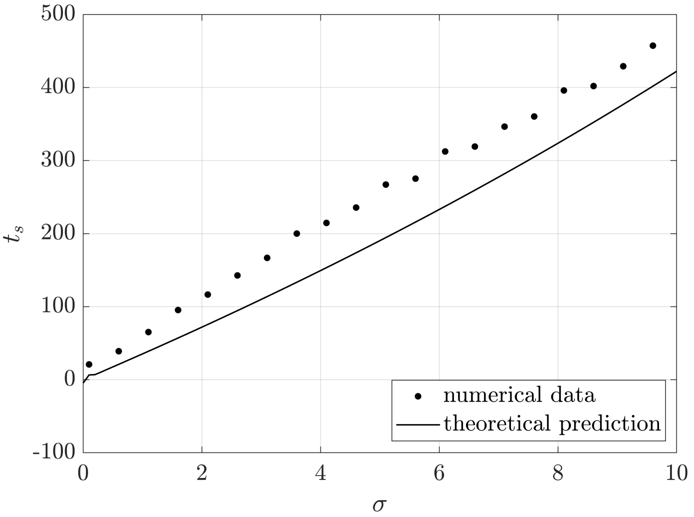

Figure 6.3: Synchronization time t_s as a function of the coupling strength σ: comparison between numerical results (dots) and theoretical predictions (solid line). Initial conditions have been set as $\mathbf{x}_1(0) = [0.9\ 0\ 0\ 0]^T$ and $\mathbf{x}_2(0) = [0.05\ 0.8\ 0\ 0]^T$. Here, $\varepsilon = 0.01$, and $T_D = 5 \times 10^5$.

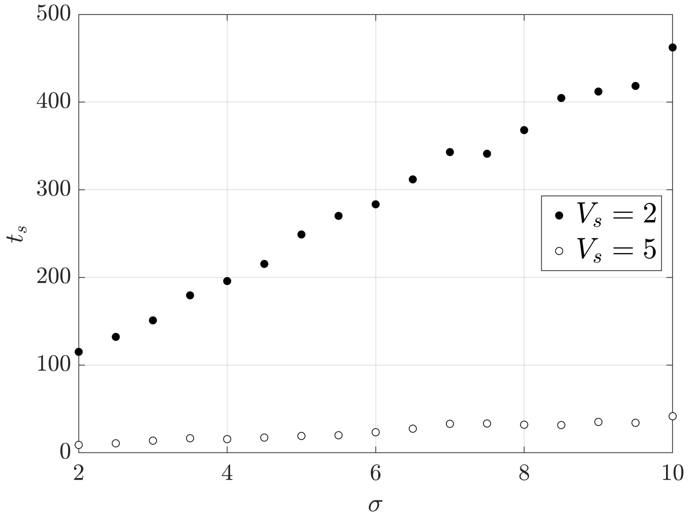

Figure 6.4: Synchronization time t_s as a function of the coupling strength σ. Initial conditions have been set as $\mathbf{x}_1(0) = [0.9\ 0\ 0\ 0]^T$ and $\mathbf{x}_2(0) = [0.05\ 0.8\ 0\ 0]^T$. Here, $\varepsilon = 0.01$ and $T_D = 1 \times 10^5$. Black circles represent the simulation results for $V_s = 2$, while white circles correspond to $V_s = 5$.

variations of σ. This comparison highlights the crucial role of the intrinsic oscillator dynamics, tuned by V_s, in determining the effectiveness of coupling. The figure therefore demonstrates that synchronization properties cannot be inferred from network topology and coupling strength alone, but depend critically on the operating regime of the individual oscillators.

6.3.3 Network-level synchronization dynamics

Extending to networks, the dependence of synchronization time on network size and topology is illustrated in Figs. 6.5 and 6.6. Star and Erdős–Rényi networks exhibit different trends, reflecting the impact of the Laplacian spectrum on synchronization stability and convergence rates.

The results in Figs. 6.5 and 6.6 confirm that network topology has a decisive influence on the scaling of synchronization time with system size. In the star configuration, t_s increases almost linearly with the number of peripheral nodes, since the central hub must mediate the convergence of all other oscillators. This behavior reflects the high heterogeneity of the Laplacian spectrum, which penalises convergence rates despite the stability of the synchronization manifold.

In contrast, Erdős–Rényi networks with connection probability $p = 0.3$ exhibit overall larger synchronization times compared to star networks of the same size. Moreover, the dependence on N is less regular and shows pronounced fluctuations, indicating that stochastic variability in the connectivity pattern strongly affects convergence. This irregular growth highlights that, although random networks avoid the extreme centralisation of the star, their heterogeneous local structures can slow down the approach to synchronization.

Taken together, these results show that stronger or denser connectivity does not automatically guarantee faster convergence. Instead, the spectral properties of the Laplacian, shaped by the underlying topology, are the key factor governing synchronization performance. This conclusion extends the observations made in Chapter 5, underscoring the importance of considering spectral characteristics beyond degree distributions or coupling intensity when assessing network-level synchronization.

Overall, these results confirm that while the synchronization manifold is stable, the convergence time does not decrease monotonically with increasing coupling strength. The non-monotonic dependence of synchronization time on coupling strength resonates with the results obtained in Chapter 5, where excessive connectivity was shown not to guarantee faster convergence.

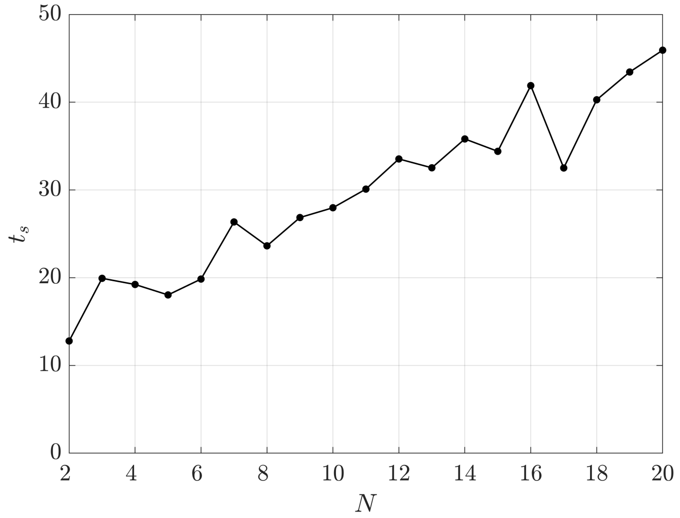

Figure 6.5: Synchronization time t_s versus network size N in a star topology. Initial conditions are randomly chosen with $x_1(0) \in [0.7, 0.9]$, $x_2(0) \in [0.1, 0.3]$, $x_3(0) = x_4(0) = 0$. Parameters: $\sigma = 200$, $\varepsilon = 0.01$, $T_D = 100$. Results are averaged over 10 simulations.

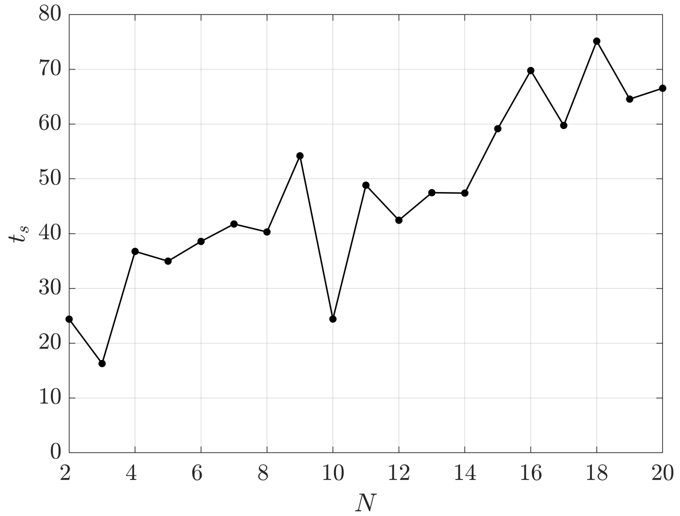

Figure 6.6: Synchronization time t_s as a function of the network size N in a star topology. Node initial conditions are randomly chosen with $x_1(0) \in [0.7, 0.9]$, $x_2(0) \in [0.1, 0.3]$, and $x_3(0) = x_4(0) = 0$. Parameters are $\sigma = 200$, $\varepsilon = 0.01$, $T_D = 100$. Reported values are averages over 10 simulations.

6.4 Key findings and remarks

This chapter has presented a theoretical and numerical investigation of synchronization in networks of chaotic circuits, with a particular focus on transistor-based Minati–Frasca oscillators. The analysis started from the mathematical modeling of the isolated circuit and its coupled configurations, highlighting the distinctive nonlinear features that make this class of oscillators both analytically tractable and experimentally accessible. By deriving the Master Stability Function for the adopted coupling protocol, the stability of the synchronous state was characterised as a function of the network topology and the coupling strength.

Numerical simulations confirmed the theoretical predictions, showing how synchronization error and synchronization time depend on the interplay between circuit parameters, interaction strength, and network structure. The analysis of pairs of coupled circuits provided insight into the fundamental mechanisms of convergence, while network-level simulations extended the results to heterogeneous topologies, revealing how structural properties affect the overall ability to sustain synchrony.

The results highlight that, even in systems with a type II MSF, synchronization in chaotic circuits is not guaranteed by simply increasing the coupling intensity. Instead, excessive coupling can degrade stability or induce longer convergence times, in agreement with the predictions of the Master Stability Function framework. This underlines the importance of balancing circuit dynamics, coupling design, and network topology when aiming to achieve coherent behavior in networks of chaotic oscillators.

Chapter 7

Conclusions

This thesis has addressed several aspects related to the modeling and control of artificial and natural complex networks from multiple and complementary perspectives, integrating theoretical and computational approaches supported by numerical simulations. The results obtained indicate that the dynamics of these systems cannot be fully captured by analyzes limited to classical graph-based representations or by purely abstract dynamical models. A more complete understanding requires the integration of higher-order network descriptions with rigorous inverse modeling techniques, together with systematic validation through numerical simulations. The contributions of this thesis can be grouped along two main lines, modeling and control.

On the modeling side, a first result has been to show how network reconstruction and generative modeling can be performed under structural and dynamical constraints, clarifying the extent to which network properties arise from optimization principles or from local statistical rules. This has provided insight into how structural heterogeneity shapes collective behavior and how realistic network ensembles can be generated for comparison against empirical data. A second modeling contribution has been the analysis of higher-order interactions and their influence on dynamical processes, with particular emphasis on synchronization phenomena. The study of simplicial complexes built upon paradigmatic systems demonstrated how pairwise and group interactions jointly determine the stability and speed of collective dynamics. This perspective extends beyond traditional graph theory and offers a framework relevant to both artificial and natural contexts, from engineered infrastructures to biological networks.

Our findings extend previous evidence in network science and complexity theory showing that higher-order organization and spatial embedding are key determinants of global functionality [19, 64]. By explicitly connecting reconstruction and generative modeling to the paradigms of emergent collective behavior [77, 10], this work situates its contributions within the broader effort to bridge structure and dynamics. In particular, the demonstration that geometric constraints and optimization criteria jointly shape connectivity aligns with the principles of spatial network formation observed in brain connectomics and power grids [21]. The reconstruction of time-varying topologies under cascading failures connects directly with the study of network resilience and percolation transitions [4, 31], offering a quantitative framework for the analysis of fault propagation in infrastructure systems.

On the control side, the thesis has investigated adaptive strategies for synchronization, introducing a switching layer that dynamically reconfigures the network topology. This approach provided theoretical guarantees of local stability and robustness, and was validated through applications to networks of chaotic oscillators and to models of power grids. Furthermore, abstract control principles have been connected to concrete implementations through the study of transistor-based chaotic circuits. By analyzing synchronization in networks of Minati–Frasca oscillators, the work has linked rigorous tools such as the Master Stability Function to physical systems that experimentally realizable. These results demonstrate how complex behavior can emerge from minimal circuit architectures, reinforcing the value of simple platforms for testing general theories of network dynamics.

From a broader control-theoretic standpoint, highlighting how decentralized interventions and adaptive feedback can sustain global coordination under structural constraints. The proposed edge-snapping mechanism contributes to this line of research by coupling control and topology evolution within the adaptive synchronization frameworks [81, 7]. The integration of multilayer adaptation also provides a concrete link to recent studies on multilayer and temporal networks [33], extending their principles to real-world systems such as the Italian high-voltage grid.

Overall, the thesis shows that advancing the understanding of complex networks requires both methodological generality and specific instantiations. The combination of reconstruction, generative models, higher-order interactions, adaptive control, and analysis of physical realizations contributes to a unified picture in which theory and application mutually inform one another.

The analysis of synchronization time slowdown complements the study of generative models by linking structural efficiency with dynamical performance.

Beyond the technical results, the work reflects a broader trajectory of interdisciplinary research, where concepts from physics, engineering, and network science converge. Several challenges remain open, particularly regarding scalability, robustness under uncertainty, and integration of multiple dynamical layers. The approaches developed here provide a foundation for addressing these challenges and indicate promising directions for future investigations.

While the reconstruction and generative procedures proved effective in controlled settings, the adaptive control strategies, though robust in simulations, require further analysis under stochastic perturbations and measurement noise. Additionally, the extension of higher-order models to empirical data, especially in biological systems, raises issues of identifiability and interpretability that deserve focused attention. Addressing these aspects represents a natural evolution of the present work and could involve hybrid methods combining machine learning and dynamical inference, as recently explored in data-driven network science [19].

In conclusion, this thesis advances both the conceptual and practical tools available for the study of complex networks. The results obtained are expected to contribute to a deeper theoretical understanding of collective dynamics and to support the design of resilient and controllable networked systems in technological and natural domains. Future extensions could follow three main directions emerging from the present findings. First, connecting data-driven reconstruction with generative spatial modeling would make it possible to iteratively compare inferred and synthesized network structures, clarifying how geometric and dynamical constraints shape connectivity in real systems. Second, extending reconstruction and control to higher-order and time-varying networks, as suggested by recent works on multilayer inference, would clarify the interplay between topology evolution, synchronization, and resilience under failures. Third, the adaptive control strategies developed here could be validated on physical or hardware-in-the-loop testbeds, where measurement noise, actuation limits, and communication delays determine the achievable synchronization performance. Altogether, these directions define a coherent path toward data-grounded, resource-aware methods for the modeling and control of artificial and natural complex networks.

Publications

A. Corso, L. V. Gambuzza, L. Minati, and M. Frasca. A generative model for spatial complex networks. Submitted to *IEEE Transactions on Network Science and Engineering*, 2025.

F. Malizia, A. Corso, L. V. Gambuzza, G. Russo, V. Latora, and M. Frasca. Reconstructing higher-order interactions in coupled dynamical systems. *Nature Communications*, 15(1), 5184, 2024.

A. Corso, L. V. Gambuzza, P. De Lellis, and M. Frasca. Synchronizing network systems in the presence of limited resources via edge snapping. *Chaos: An Interdisciplinary Journal of Nonlinear Science*, 33(1), p.013123, 2023.

A. Corso, L. V. Gambuzza, F. Malizia, G. Russo, V. Latora, and M. Frasca. Reconstruction of cascading failures in dynamical models of power grids. *Journal of Complex Networks*, 10(4), p.cnac035, 2022.

Bibliography

[1] J. A. Acebrón, L. L. Bonilla, C. J. Pérez Vicente, F. Ritort, and R. Spigler. The kuramoto model: A simple paradigm for synchronization phenomena. *Reviews of modern physics*, 77(1):137–185, 2005.

[2] A. Agarwal, R. Dowsley, N. D. McKinney, D. Wu, C.-T. Lin, M. De Cock, and A. C. Nascimento. Protecting privacy of users in brain-computer interface applications. *IEEE Transactions on Neural Systems and Rehabilitation Engineering*, 27(8):1546–1555, 2019.

[3] M. AlAdwani and S. Saavedra. Is the addition of higher-order interactions in ecological models increasing the understanding of ecological dynamics? *Mathematical Biosciences*, 315:108222, 2019.

[4] R. Albert, H. Jeong, and A.-L. Barabási. Error and attack tolerance of complex networks. *nature*, 406(6794):378–382, 2000.

[5] U. Alvarez-Rodriguez, F. Battiston, G. F. de Arruda, Y. Moreno, M. Perc, and V. Latora. Evolutionary dynamics of higher-order interactions in social networks. *Nature Human Behaviour*, 5(5):586–595, 2021.

[6] T. Aoki and T. Aoyagi. Co-evolution of phases and connection strengths in a network of phase oscillators. *Physical Review Letters*, 102(3):034101, 2009.

[7] A. Arenas, A. Díaz-Guilera, J. Kurths, Y. Moreno, and C. Zhou. Synchronization in complex networks. *Physics reports*, 469(3):93–153, 2008.

[8] S. Assenza, R. Gutiérrez, J. Gómez-Gardenes, V. Latora, and S. Boccaletti. Emergence of structural patterns out of synchronization in networks with competitive interactions. *Scientific reports*, 1(1):99, 2011.

[9] A. Babayan, M. Erbey, D. Kumral, J. D. Reinelt, A. M. Reiter, J. Röbbig, H. L. Schaare, M. Uhlig, A. Anwander, P.-L. Bazin, et al. A mind-brain-body dataset of mri, eeg, cognition, emotion, and peripheral physiology in young and old adults. *Scientific Data*, 6(1):1–21, 2019.

[10] A.-L. Barabási. Network science. *Philosophical Transactions of the Royal Society A: Mathematical, Physical and Engineering Sciences*, 371(1987):20120375, 2013.

[11] A.-L. Barabási and R. Albert. Emergence of scaling in random networks. *Science*, 286(5439):509–512, 1999.

[12] M. Barthélemy. Spatial networks. *Physics reports*, 499(1-3):1–101, 2011.

[13] F. Battiston, G. Cencetti, I. Iacopini, V. Latora, M. Lucas, A. Patania, J.-G. Young, and G. Petri. Networks beyond pairwise interactions: Structure and dynamics. *Physics reports*, 874:1–92, 2020.

[14] V. W. Berger and Y. Zhou. Kolmogorov–smirnov test: Overview. *Wiley statsref: Statistics reference online*, 2014.

[15] D. Berry and S. Widder. Deciphering microbial interactions and detecting keystone species with co-occurrence networks. *Frontiers in microbiology*, 5:219, 2014.

[16] R. F. Betzel, A. Avena-Koenigsberger, J. Goñi, Y. He, M. A. De Reus, A. Griffa, P. E. Vértes, B. Mišic, J.-P. Thiran, P. Hagmann, et al. Generative models of the human connectome. *Neuroimage*, 124:1054–1064, 2016.

[17] R. F. Betzel and D. S. Bassett. Generative models for network neuroscience: prospects and promise. *Journal of The Royal Society Interface*, 14(136):20170623, 2017.

[18] S. Boccaletti, D.-U. Hwang, M. Chavez, A. Amann, J. Kurths, and L. M. Pecora. Synchronization in dynamical networks: Evolution along commutative graphs. *Physical Review E—Statistical, Nonlinear, and Soft Matter Physics*, 74(1):016102, 2006.

[19] S. Boccaletti, V. Latora, Y. Moreno, M. Chavez, and D.-U. Hwang. Complex networks: Structure and dynamics. *Physics reports*, 424(4-5):175–308, 2006.

[20] S. Boccaletti, A. N. Pisarchik, C. I. Del Genio, and A. Amann. *Synchronization: from coupled systems to complex networks*. Cambridge University Press, 2018.

[21] E. Bullmore and O. Sporns. Complex brain networks: graph theoretical analysis of structural and functional systems. *Nature reviews neuroscience*, 10(3):186–198, 2009.

[22] E. Bullmore and O. Sporns. The economy of brain network organization. *Nature reviews neuroscience*, 13(5):336–349, 2012.

[23] E. T. Bullmore and D. S. Bassett. Brain graphs: graphical models of the human brain connectome. *Annual review of clinical psychology*, 7:113–140, 2011.

[24] K. S. Button, J. P. Ioannidis, C. Mokrysz, B. A. Nosek, J. Flint, E. S. Robinson, and M. R. Munafò. Power failure: why small sample size undermines the reliability of neuroscience. *Nature reviews neuroscience*, 14(5):365–376, 2013.

[25] T. J. Case. Illustrated guide to theoretical ecology. *Ecology*, 80(8):2848–2848, 1999.

[26] X. L. T. Chen. Network synchronization with an adaptive coupling strength. *arXiv preprint math/0610580*, 2006.

[27] P. Christie and D. Stroobandt. The interpretation and application of rent's rule. *IEEE Transactions on Very Large Scale Integration (VLSI) Systems*, 8(6):639–648, 2002.

[28] A. Corso. Interactive map of the italian high-voltage power grid. `https://alesscorso.github.io/map/MAPItalianPowerGrid.html`, 2022. Accessed: 2025-08-17.

[29] A. Corso, L. V. Gambuzza, P. De Lellis, and M. Frasca. Synchronizing network systems in the presence of limited resources via edge snapping. *Chaos: An Interdisciplinary Journal of Nonlinear Science*, 33(1), 2023.

[30] A. Corso, L. V. Gambuzza, F. Malizia, G. Russo, V. Latora, and M. Frasca. Reconstruction of cascading failures in dynamical models of power grids. *Journal of Complex Networks*, 10(4):cnac035, 2022.

[31] P. Crucitti, V. Latora, M. Marchiori, and A. Rapisarda. Error and attack tolerance of complex networks. *Physica A: Statistical mechanics and its applications*, 340(1-3):388–394, 2004.

[32] J. Dall and M. Christensen. Random geometric graphs. *Physical review E*, 66(1):016121, 2002.

[33] M. De Domenico, A. Solé-Ribalta, E. Cozzo, M. Kivelä, Y. Moreno, M. A. Porter, S. Gómez, and A. Arenas. Mathematical formulation of multilayer networks. *Physical Review X*, 3(4):041022, 2013.

[34] P. De Lellis, M. Di Bernardo, F. Sorrentino, and A. Tierno. Adaptive synchronization of complex networks. *International Journal of Computer Mathematics*, 85(8):1189–1218, 2008.

[35] P. DeLellis, M. Di Bernardo, T. E. Gorochowski, and G. Russo. Synchronization and control of complex networks via contraction, adaptation and evolution. *IEEE Circuits and Systems Magazine*, 10(3):64–82, 2010.

[36] P. DeLellis, M. di Bernardo, and M. Porfiri. Pinning control of complex networks via edge snapping. *Chaos: An Interdisciplinary Journal of Nonlinear Science*, 21(3), 2011.

[37] P. DeLellis, A. DiMeglio, F. Garofalo, and F. Lo Iudice. The evolving cobweb of relations among partially rational investors. *PloS One*, 12(2):e0171891, 2017.

[38] P. DeLellis, F. Garofalo, M. Porfiri, et al. Evolution of complex networks via edge snapping. *IEEE Transactions on Circuits and Systems I: Regular Papers*, 57(8):2132–2143, 2010.

[39] F. Della Rossa and P. De Lellis. Synchronization and pinning control of stochastic coevolving networks. *Annual Reviews in Control*, 53:147–160, 2022.

[40] P. ERDdS and A. R&wi. On random graphs i. *Publ. math. debrecen*, 6(290-297):18, 1959.

[41] E. Estrada. Network robustness to targeted attacks. the interplay of expansibility and degree distribution. *The European Physical Journal B-Condensed Matter and Complex Systems*, 52(4):563–574, 2006.

[42] X. Fan, E. Dudkina, L. V. Gambuzza, M. Frasca, and E. Crisostomi. A network-based structure-preserving dynamical model for the study of cascading failures in power grids. *Electric Power Systems Research*, 209:107987, 2022.

[43] G. Filatrella, A. H. Nielsen, and N. F. Pedersen. Analysis of a power grid using a kuramoto-like model. *The European Physical Journal B*, 61(4):485–491, 2008.

[44] L. Fortuna, M. Frasca, and A. Sarra Fiore. A network of oscillators emulating the italian high-voltage power grid. *International Journal of Modern Physics B*, 26(25):1246011, 2012.

[45] M. Frasca and L. V. Gambuzza. Control of cascading failures in dynamical models of power grids. *Chaos, Solitons & Fractals*, 153:111460, 2021.

[46] L. Gallo, R. Muolo, L. V. Gambuzza, V. Latora, M. Frasca, and T. Carletti. Synchronization induced by directed higher-order interactions. *Communications Physics*, 5(1):263, 2022.

[47] L. V. Gambuzza, A. Buscarino, L. Fortuna, M. Porfiri, and M. Frasca. Analysis of dynamical robustness to noise in power grids. *IEEE Journal on Emerging and Selected topics in Circuits and Systems*, 7(3):413–421, 2017.

[48] L. V. Gambuzza, F. Di Patti, L. Gallo, S. Lepri, M. Romance, R. Criado, M. Frasca, V. Latora, and S. Boccaletti. Stability of synchronization in simplicial complexes. *Nature communications*, 12(1):1255, 2021.

[49] GENI—Global Energy Network Institute. Map of Italian electricity grid. `https://www.geni.org/globalenergy/library/national_energy_grid/italy/italiannationalelectricitygrid.shtml`, 2020. [Online; accessed 21-December-2020].

[50] D. Ghosh, M. Frasca, A. Rizzo, S. Majhi, S. Rakshit, K. Alfaro-Bittner, and S. Boccaletti. The synchronized dynamics of time-varying networks. *Physics Reports*, 949:1–63, 2022.

[51] G. H. Golub and C. F. Van Loan. *Matrix computations*. JHU press, 2013.

[52] J. Grilli, G. Barabás, M. J. Michalska-Smith, and S. Allesina. Higher-order interactions stabilize dynamics in competitive network models. *Nature*, 548(7666):210–213, 2017.

[53] T. Gross and B. Blasius. Adaptive coevolutionary networks: a review. *Journal of the Royal Society Interface*, 5(20):259–271, 2008.

[54] R. Gutiérrez, A. Amann, S. Assenza, J. Gómez-Gardenes, V. Latora, and S. Boccaletti. Emerging meso-and macroscales from synchronization of adaptive networks. *Physical Review Letters*, 107(23):234103, 2011.

[55] M. E. Hibbing, C. Fuqua, M. R. Parsek, and S. B. Peterson. Bacterial competition: surviving and thriving in the microbial jungle. *Nature reviews microbiology*, 8(1):15–25, 2010.

[56] F. G. Hillary and J. H. Grafman. Injured brains and adaptive networks: the benefits and costs of hyperconnectivity. *Trends in cognitive sciences*, 21(5):385–401, 2017.

[57] I. Iacopini, G. Petri, A. Barrat, and V. Latora. Simplicial models of social contagion. *Nature communications*, 10(1):2485, 2019.

[58] R. Jansen, H. Yu, D. Greenbaum, Y. Kluger, N. J. Krogan, S. Chung, A. Emili, M. Snyder, J. F. Greenblatt, and M. Gerstein. A bayesian networks approach for predicting protein-protein interactions from genomic data. *Science*, 302(5644):449–453, 2003.

[59] A. Jimenez-Marin, I. Diez, A. Erramuzpe, S. Stramaglia, P. Bonifazi, and J. M. Cortes. Open datasets and code for multi-scale relations on structure, function and neuro-genetics in the human brain. *Scientific Data*, 11(1):256, 2024.

[60] S. A. Kauffman. *At home in the universe: The search for laws of self-organization and complexity.* Oxford University Press, USA, 1995.

[61] M. P. Kennedy. Chaos in the colpitts oscillator. *IEEE Transactions on circuits and systems I: Fundamental Theory and Applications*, 41(11):771–774, 1994.

[62] C. Ladroue, S. Guo, K. Kendrick, and J. Feng. Beyond element-wise interactions: identifying complex interactions in biological processes. *PloS one*, 4(9):e6899, 2009.

[63] V. Latora and M. Marchiori. Efficient behavior of small-world networks. *Physical Review Letters*, 87(19):198701, 2001.

[64] V. Latora, V. Nicosia, and G. Russo. *Complex networks: principles, methods and applications.* Cambridge University Press, 2017.

[65] C. L. Lawson and R. J. Hanson. *Solving least squares problems.* SIAM, 1995.

[66] Q. Li, D. Ding, and M. Conti. Brain-computer interface applications: Security and privacy challenges. In *2015 IEEE conference on communications and network security (CNS)*, pages 663–666. IEEE, 2015.

[67] S. Lizotte, J.-G. Young, and A. Allard. Hypergraph reconstruction from uncertain pairwise observations. *Scientific Reports*, 13(1):21364, 2023.

[68] D. A. B. Lombana and M. Di Bernardo. Distributed pid control for consensus of homogeneous and heterogeneous networks. *IEEE Transactions on Control of Network Systems*, 2(2):154–163, 2014.

[69] D. A. B. Lombana and M. Di Bernardo. Multiplex pi control for consensus in networks of heterogeneous linear agents. *Automatica*, 67:310–320, 2016.

[70] S. Lozano, L. Buzna, and A. Díaz-Guilera. Role of network topology in the synchronization of power systems. *The European Physical Journal B*, 85:1–8, 2012.

[71] F. Malizia, A. Corso, L. V. Gambuzza, G. Russo, V. Latora, and M. Frasca. Reconstructing higher-order interactions in coupled dynamical systems. *Nature Communications*, 15(1):5184, 2024.

[72] E. Martinez-Heras, F. Grussu, F. Prados, E. Solana, and S. Llufriu. Diffusion-weighted imaging: recent advances and applications. In *Seminars in Ultrasound, CT and MRI*, volume 42, pages 490–506. Elsevier, 2021.

[73] L. Minati, M. Frasca, P. Oświecimka, L. Faes, and S. Drożdż. Atypical transistor-based chaotic oscillators: Design, realization, and diversity. *Chaos: An Interdisciplinary Journal of Nonlinear Science*, 27(7), 2017.

[74] L. Minati, M. Frasca, N. Yoshimura, and Y. Koike. Versatile locomotion control of a hexapod robot using a hierarchical network of nonlinear oscillator circuits. *IEEE Access*, 6:8042–8065, 2018.

[75] L. Minati, G. Innocenti, G. Mijatovic, H. Ito, and M. Frasca. Mechanisms of chaos generation in an atypical single-transistor oscillator. *Chaos, Solitons & Fractals*, 157:111878, 2022.

[76] R. Muolo, L. Giambagli, H. Nakao, D. Fanelli, and T. Carletti. Turing patterns on discrete topologies: from networks to higher-order structures. In *Proceedings A*, volume 480, page 20240235. The Royal Society, 2024.

[77] M. Newman. *Networks*. Oxford university press, 2018.

[78] M. E. Newman. Communities, modules and large-scale structure in networks. *Nature physics*, 8(1):25–31, 2012.

[79] M. E. Newman and M. Girvan. Finding and evaluating community structure in networks. *Physical review E*, 69(2):026113, 2004.

[80] T. Nishikawa and A. E. Motter. Comparative analysis of existing models for power-grid synchronization. *New Journal of Physics*, 17(1):015012, 2015.

[81] L. M. Pecora and T. L. Carroll. Master stability functions for synchronized coupled systems. *Physical Review Letters*, 80(10):2109, 1998.

[82] R. Pernice, L. Faes, M. Feucht, F. Benninger, S. Mangione, and K. Schiecke. Pairwise and higher-order measures of brain-heart interactions in children with temporal lobe epilepsy. *Journal of Neural Engineering*, 19(4):045002, 2022.

[83] J. Ren, W.-X. Wang, B. Li, and Y.-C. Lai. Noise bridges dynamical correlation and topology in coupled oscillator networks. *Physical Review Letters*, 104(5):058701, 2010.

[84] E. Rényi. On random graph. *Publicationes Mathematicate*, 6:290–297, 1959.

[85] F. E. Rosas, P. A. Mediano, A. I. Luppi, T. F. Varley, J. T. Lizier, S. Stramaglia, H. J. Jensen, and D. Marinazzo. Disentangling high-order mechanisms and high-order behaviours in complex systems. *Nature Physics*, 18(5):476–477, 2022.

[86] V. Rosato, S. Bologna, and F. Tiriticco. Topological properties of high-voltage electrical transmission networks. *Electric Power Systems Research*, 77(2):99–105, 2007.

[87] D. Samu, A. K. Seth, and T. Nowotny. Influence of wiring cost on the large-scale architecture of human cortical connectivity. *PLoS computational biology*, 10(4):e1003557, 2014.

[88] A. Santoro, F. Battiston, G. Petri, and E. Amico. Higher-order organization of multivariate time series. *Nature Physics*, 19(2):221–229, 2023.

[89] H. Sayama, I. Pestov, J. Schmidt, B. J. Bush, C. Wong, J. Yamanoi, and T. Gross. Modeling complex systems with adaptive networks. *Computers & Mathematics with Applications*, 65(10):1645–1664, 2013.

[90] B. Schäfer, D. Witthaut, M. Timme, and V. Latora. Dynamically induced cascading failures in power grids. *Nature communications*, 9(1):1975, 2018.

[91] T. Schreiber. Measuring information transfer. *Physical Review Letters*, 85(2):461, 2000.

[92] P. Schultz, J. Heitzig, and J. Kurths. A random growth model for power grids and other spatially embedded infrastructure networks. *The European Physical Journal Special Topics*, 223(12):2593–2610, 2014.

[93] S. G. Shandilya and M. Timme. Inferring network topology from complex dynamics. *New Journal of Physics*, 13(1):013004, 2011.

[94] L. Shi, C. Shen, L. Jin, Q. Shi, Z. Wang, and S. Boccaletti. Inferring network structures via signal lasso. *Physical Review Research*, 3(4):043210, 2021.

[95] P. Singh and G. Baruah. Higher order interactions and species coexistence. *Theoretical Ecology*, 14(1):71–83, 2021.

[96] J. Sprott. *Chaos and Time-Series Analysis.* Oxford University Press, 2003.

[97] L. Tang, X. Wu, J. Lü, J.-a. Lu, and R. M. D'Souza. Master stability functions for complete, intralayer, and interlayer synchronization in multiplex networks of coupled rössler oscillators. *Physical Review E*, 99(1):012304, 2019.

[98] M. Timme and J. Casadiego. Revealing networks from dynamics: an introduction. *Journal of Physics A: Mathematical and Theoretical*, 47(34):343001, 2014.

[99] G. Tirabassi, R. Sevilla-Escoboza, J. M. Buldú, and C. Masoller. Inferring the connectivity of coupled oscillators from time-series statistical similarity analysis. *Scientific reports*, 5(1):10829, 2015.

[100] C. H. Totz, S. Olmi, and E. Schöll. Control of synchronization in two-layer power grids. *Physical Review E*, 102(2):022311, 2020.

[101] J.-D. Tournier, S. Mori, and A. Leemans. Diffusion tensor imaging and beyond. *Magnetic resonance in medicine*, 65(6):1532, 2011.

[102] P. Trosvik, K. Rudi, K. O. Strætkvern, K. S. Jakobsen, T. Næs, and N. C. Stenseth. Web of ecological interactions in an experimental gut microbiota. *Environmental microbiology*, 12(10):2677–2687, 2010.

[103] L. Tumash, S. Olmi, and E. Schöll. Stability and control of power grids with diluted network topology. *Chaos: An Interdisciplinary Journal of Nonlinear Science*, 29(12), 2019.

[104] R. Vicente, M. Wibral, M. Lindner, and G. Pipa. Transfer entropy—a model-free measure of effective connectivity for the neurosciences. *Journal of computational neuroscience*, 30(1):45–67, 2011.

[105] W.-X. Wang, Y.-C. Lai, C. Grebogi, and J. Ye. Network reconstruction based on evolutionary-game data via compressive sensing. *Physical Review X*, 1(2):021021, 2011.

[106] D. J. Watts and S. H. Strogatz. Collective dynamics of 'small-world'networks. *nature*, 393(6684):440–442, 1998.

[107] D. Witthaut, F. Hellmann, J. Kurths, S. Kettemann, H. Meyer-Ortmanns, and M. Timme. Collective nonlinear dynamics and self-organization in decentralized power grids. *Reviews of modern physics*, 94(1):015005, 2022.

[108] X. Wu, X. Zhao, J. Lü, L. Tang, and J.-a. Lu. Identifying topologies of complex dynamical networks with stochastic perturbations. *IEEE Transactions on Control of Network Systems*, 3(4):379–389, 2015.

[109] X. Wu, C. Zhou, G. Chen, and J.-a. Lu. Detecting the topologies of complex networks with stochastic perturbations. *Chaos: An Interdisciplinary Journal of Nonlinear Science*, 21(4), 2011.

[110] M. Xia, J. Wang, and Y. He. Brainnet viewer: a network visualization tool for human brain connectomics. *PloS one*, 8(7):e68910, 2013.

[111] Y. Yang and A. E. Motter. Cascading failures as continuous phase-space transitions. *Physical Review Letters*, 119(24):248302, 2017.

[112] J.-G. Young, G. Petri, and T. P. Peixoto. Hypergraph reconstruction from network data. *Communications Physics*, 4(1):135, 2021.

[113] D. Yu, M. Righero, and L. Kocarev. Estimating topology of networks. *Physical Review Letters*, 97(18):188701, 2006.

[114] X.-Y. Zhang, J. M. Moore, X. Ru, and G. Yan. Geometric scaling law in real neuronal networks. *Physical Review Letters*, 133(13):138401, 2024.

[115] C. Zhou and J. Kurths. Dynamical weights and enhanced synchronization in adaptive complex networks. *Physical Review Letters*, 96(16):164102, 2006.

[116] Q. Zhou and J. W. Bialek. Approximate model of european interconnected system as a benchmark system to study effects of cross-border trades. *IEEE Transactions on power systems*, 20(2):782–788, 2005.